Title
Stress modulation of earthquakes: A study of long and short period stress perturbations and the crustal response

Author
Johnson, Christopher W.

Publication Date
2017

Peer reviewed|Thesis/dissertation

Stress modulation of earthquakes: A study of long and short period stress perturbations and the crustal response

by

Christopher W Johnson

A dissertation submitted in partial satisfaction of the
requirements for the degree of
Doctor of Philosophy

in

Earth and Planetary Science

in the

Graduate Division

of the

University of California, Berkeley

Committee in charge:

Professor Roland Bürgmann, Chair
Professor Michael Manga
Professor David Brillinger

Summer 2017

Stress modulation of earthquakes: A study of long and short period stress perturbations and the crustal response

Abstract

Stress modulation of earthquakes: A study of long and short period stress perturbations and the crustal response

by

Christopher W Johnson

Doctor of Philosophy in Earth and Planetary Science

University of California, Berkeley

Professor Roland Bürgmann, Chair

Decomposing fault mechanical processes advances our understanding of active fault systems and properties of the lithosphere, thereby increasing the effectiveness of seismic hazard assessment and preventative measures implemented in urban centers. Along plate boundaries earthquakes are inevitable as tectonic forces reshape the Earths surface. Earthquakes, faulting, and surface displacements are related systems that require multidisciplinary approaches to characterize deformation in the lithosphere. Modern geodetic instrumentation can resolve displacements to millimeter precision and provide valuable insight into secular deformation in near real-time. The expansion of permanent seismic networks as well as temporary deployments allow unprecedented detection of microseismic events that image fault interfaces and fracture networks in the crust. The research presented in this dissertation is at the intersection of seismology and geodesy to study the Earth's response to transient deformation and explores research questions focusing on earthquake triggering, induced seismicity, and seasonal loading while utilizing seismic data, geodetic data, and modeling tools. The focus is to quantify stress changes in the crust, explore seismicity rate variations and migration patterns, and model crustal deformation in order to characterize the evolving state of stress on faults and the migration of fluids in the crust. The collection of problems investigated all investigate the question: Why do earthquakes nucleate following a low magnitude stress perturbation? Answers to this question are fundamental to understanding the time dependent failure processes of the lithosphere.

Dynamic triggering is the interaction of faults and stress transferring from one system to another, at both local and remote distances (Freed, 2005). The passage of teleseismic surface waves from the worlds largest earthquakes produce dynamic stress fields and provides a natural experiment to explore the causal relationship between low-amplitude stress changes and dynamically triggered events. Interestingly, observations of dynamically triggered M$\geq$5.5 earthquakes are absent in the seismic records (Johnson, Bürgmann, et al., 2015; Parsons and Velasco, 2011), which invokes questions regarding whether or not large magnitude events can be dynamically triggered. Emerging results in the literature indicate undocumented M$\geq$5.5

events at near to intermediate distances are dynamically triggered during the passage of surface waves but are undetected by automated networks (Fan and Shearer, 2016). This raises new questions about the amplitude and duration of dynamic stressing for large magnitude events. I used 35-years of global seismicity and find that large event rate increases only occur following a delay from the transient load, suggesting aseismic processes are associated with large magnitude triggered events. To extend this finding I investigated three cases of large magnitude delayed dynamic triggering following the M8.6 2012 Indian Ocean earthquake (Pollitz, Stein, et al., 2012) by producing microseismicity catalogs and modeling the transient stresses. The results indicate immediate triggering of microseismic events that hours later culminate into a large magnitude event and support the notion that large magnitude events are triggerable by transient loading, but seismic and aseismic processes (e.g. induced creep or fluid mobilization) are contributing to the nucleation process. Open questions remain concerning the source of a nucleation delay period following a stress perturbation that require both geodetic and seismic observations to constrain the source of delayed dynamic triggering and possibly provide insight into a precursory nucleation phase

Induced seismicity has gained much attention in the past 5 years as earthquake rates in regions of low tectonic strain accumulation accelerate to unprecedented levels (Ellsworth, 2013). The source of the seismicity is attributed to shallow fluid injection associated with energy production. As hydrocarbon extraction continues to increase in the U.S. the deformation and induced seismicity from wastewater injection is providing new avenues to explore crustal properties. The large magnitude events associated with regions of high rate injection support the notion that the crust is critically stressed. Seismic data in these areas provides the opportunity to delineate fault structures in the crust using precise earthquake locations. Using high-resolution hypocenter data from The Geysers geothermal field in northern California I implement an epidemic type aftershock sequence (ETAS) model to develop seismicity rate time series in the active geothermal field and characterize the migration of fluids from high volume water injection. Subtle stress changes induced by thermo- and poroelastic stresses trigger seismicity for $\sim$5 months after peak injection at depths $\sim$3 km below the main injection interval. This suggests vertical migration paths are maintained in the geothermal field that allows fluid propagation on annual time scales. Fully describing the migration pattern of fluids in the crust and the associated stresses are applicable to tectonic related faulting and triggered seismic activity.

Seasonal hydrological loading is a source of annual periodic transient deformation that is ideal for investigating the modulation of seismicity. The initial step in exploring the modulation of seismicity is to validate that a significant annual period does exist in California earthquake records. The periodicity results (Dutilleul et al., 2015) motivate continued investigation of seismically active regions that experience significant seasonal mass loading, i.e. high precipitation and snowfall rates, to quantify the magnitude of seasonal stress changes and possible correlation with seismicity modulation. The implication of this research addresses questions concerning the strength and state of stress on faults. High-resolution water storage time series throughout California are developed using continuous GPS records. The results allow an estimation of the stress changes induced by hydrological loading, which

is combined with a detailed focal mechanism analysis to characterize the modulation of seismicity. The hydrologic loading is augmented with the contribution of additional deformation sources (e.g. tidal, atmosphere, and temperature) and show that annual stress changes of 5 kPa are modulating seismicity. These observations suggest that mechanical differences exist between the vertically dipping strike-slip faults and the shallowly dipping oblique structures in California. When comparing all the annual loading cycles it is evident that future studies should incorporate all the sources of solid Earth deformation to fully describe the stresses realized on fault systems that respond to seasonal loads.

To Randee, my family, and everyone along the way.

Contents

List of Figures

List of Tables

Acknowledgments

First and foremost I want to thank my advisor Roland Bürgmann for all of the guidance, patience, and understanding over the past 5 years. I have learned more than any other time in my life and I owe it to him for access to this amazing research program. His overall positive attitude, enthusiasm for science, and broad knowledge creates a great atmosphere for pushing research forward, especially when initial results do not look promising. I have directly benefitted from the exposure he provides to a diverse range of topics and the collaborations with many scientists in the community. His extremely productive work-life balance is great encouragement for me to enjoy pursuing challenging research questions and maintain an active lifestyle. It has truly been a pleasure working with Roland and I look forward to many more insightful conversations in the coming years.

I would also like to thank the many members of the Active Tectonics group who help create a great working environment that produces so much exciting science. In particular Kim Blisniuk, Estelle Chaussard, Brent Delbridge, Ronni Grapenthin, Yan Hu, Mong-Han Huang, Kathryn Materna, Noah Randolph-Flagg, Manoochehr Shirzaei, and Lian Xue. Each of these scientists have contributed to my work through constructive feedback to improve results and push the science forward.

The Berkeley Seismological Laboratory has been a great place to work during my Ph.D and I thank the researchers and staff that maintain the network and data. In particular Taka'aki Tiara for many great conversations and his knowledge of seismology. Also, I would like to thank my officemates Kathryn Materna, Qingkai Kong, and William Hawley. It has been a lot of fun over the years. In addition I would like to thank Fred Pollitz, Pierre Dutilluel, and Yuning Fu, all of who I have directly worked with over the years and greatly benefitted from their collaboration.

Finally I thank my family for all the support in pursuing this education. In particular my wife Randee who has been there since the beginning of my undergraduate degree and fully supported my decisions to pursue an advanced degree. Her patience and understanding of the commitment I made allowed this to happen. Also my loving parents, even during challenging times in their lives they have continued to support me. And my sister, I will be there for her because I know she will always be there for me.

Chapter 1

Introduction

The timing of earthquakes is fundamental to extending our knowledge of fault related properties and nucleation processes, which invokes the question: Why do faults respond to low magnitude stress perturbation and what can we learn about earthquake nucleation? These questions probe the state of stress in the crust and are the focus of the material presented in this dissertation. As stress accumulates in the crust, an earthquake is the brittle failure to relieve that stress and results in energy radiated from the source and near-field permanent surface deformation. The initiation of an earthquake is when the loading on a fault exceeds the strength, resulting in slip. Transient loading occurs on a range of time scales and both short-period (10's-1000's sec) and long-period ($\sim$1 yr) stress changes are observed to trigger earthquakes. Earthquake triggering is when a known external force is applied to the lithosphere, in addition to the tectonic forces, and an earthquake occurs. It is postulated that the crust is critically stressed, as inferred from earthquakes occurring following a low amplitude stress perturbation on the order of 1-1,000 kPa. Relating the timing of earthquakes to small transient stress perturbations provides insight to the failure process and the state of stress on the fault.

Transient loading occurs on time scales that are orders of magnitude less than tectonic loading, but the timing of triggered earthquakes can be related to the stress changes induced by quantifiable stress changes. Outstanding questions remain to fully describe the failure processes involved with earthquake triggering and how small stress changes can result in changes in seismicity variations that occur immediately or are delayed, suggesting multiple failure processes are occurring simultaneously. The research in this dissertation incorporates geodetically observed surface deformation and seismology to examine these stress changes from multiple loading sources along with earthquake timing to decompose the mechanical processes of faulting for triggered events. The material is presented in 5 chapters that describe 3 different sources of transient stressing. The sources of loading are earthquake interaction, subsurface fluid injection, and surface loading. Each source of deformation occurs on a different time scale but the response of the crust in the same, an earthquake.

In Chapter 2 and 3 the source of transient stressing that is explored is from teleseismic surface waves. At distances 100's to 1000's of kilometers from the mainshock, transient

stresses during the passage of long-period (10 - 100 seconds) surface waves and have been shown to dynamically trigger microearthquakes (M<3), as well as non-volcanic tremor during the passage of seismic waves, and sometimes continuing long after the seismic waves have passed (Hill and Prejean, 2015; Shelly, Peng, et al., 2011; Pankow et al., 2004). Studies of dynamically triggered earthquakes explore the temporal and distal limits of earthquake interaction. In Chapter 2 I investigate global seismicity catalog records for evidence of dynamic triggering of large magnitude (M≥5.5) earthquakes. The results indicate periods of elevated seismicity rates for large magnitude events only in the ensuing days following the passage of surface waves, with no evidence of immediate triggering. The observation of elevated seismicity rates is limited to specific global mainshock and is not a widespread phenomenon suggesting that larger magnitude events, if triggered, do not respond to a failure threshold and requires additional failure processes to explain the onset of nucleation.

As no immediate dynamic triggering of large magnitude events is observed (Parsons and Velasco, 2011; Johnson, Bürgmann, et al., 2015), in Chapter 3 I investigate the role of delayed dynamic triggering, i.e. the interaction of teleseismic surface waves with a fault zone and a delayed seismic response. Following the 2012 M8.6 Indian Ocean earthquake, Pollitz, Stein, et al. (2012) document the widespread increase in large magnitude events, suggesting a global aftershock zone. Three M≥6.0 earthquakes occur within 24 hours of the large amplitude surface waves. The study presented here uses regional seismic networks to examine changes in microseismicity in the hours leading up to the events following the surface wave passage. The results indicate immediate triggering of unreported low magnitude earthquakes prior the M≥6.0 events. Interestingly the fault zones in a transtensional tectonic environment exhibit more triggered events during the surface wave passage. The observation is consistent with modeling that indicates these tectonic regimes require lower stress perturbatinos to trigger an earthquake (Hill, 2012).

In Chapter 4 I explore the changes in the depth of seismicity rates in The Geysers geothermal field in northern California during a 10-year period of high volume water injection to stimulate steam for power production. Induced seismicity is the crustal response to fluid injection. Fluid injection into the subsurface is a long-known phenomenon to produce changes in seismic activity (Healy et al., 1968) and the related seismicity can result from multiple failure processes with many questions still to be addressed. Depending on the subsurface environment, studies of individual wells indicate failure can be due to both thermoelastic and poroelastic stresses large enough to increase seismicity rates. The focus of the study at The Geysers is the migration of fluid with depth through the entire geothermal field. Most water injection occurs at depths between 0.5-2.0 km, but changes in seismicity are evident to depths of 5 km. The migration time of the seismicity suggests a steeply dipping fracture network allows the fluid to reach depths of 5 km during a 6-month period. The migration observed supports the failure models of thermoelastic stresses inducing seismicity in the near-field and poroelastic stresses resulting from fluid migrating deeper into the subsurface on time scales of months.

In Chapter 5 and 6 the source of transient loading explored is the natural cycles of seasonal and celestial loading. In Chapter 5 the water loading cycle in central and northern

California is characterized using continuous GPS recordings. Continuous GPS measurements indicate an annual undulation in the vertical displacement time series. A main source of the flexure of the crust is the response to the surface loading that results from seasonal snow and water accumulation during the winter months. The dense GPS network allows for high spatial and temporal resolution of water loading and facilitates the calculation of deformation at seismogenic depths from this loading source. To relate the deformation to excess events earthquakes during periods of slip encouraging stress conditions the focal mechanism catalog is exploited to provide the orientation of slip at the time of failure. The results suggest that seasonal stress perturbations of 1-5 kPa produce seismicity in excess of the background occurrence. In Chapter 6 the water loading cycle is augmented by fully describing the stresses associated with natural loads that stress the crust, i.e. atmosphere pressure, temperature gradients, ocean tides, and Earth pole and body tides. Quantifying all the loading cycles allows careful analysis of the contribution from each. The results suggest that considering all sources of seasonal loading is required to fully describe the seasonal deformation. More importantly the correct orientation of faults to resolve the stress is of great importance to accurately describe the magnitude of loading.

Chapter 2

Global catalog analysis shows that dynamic triggering of remote M≥5.5 earthquakes is rare

Published as: Johnson, C.W., R. Bürgmann, and F.F. Pollitz (2015), Rare dynamic triggering of remote M≥5.5 earthquakes from global catalog analysis, Journal of Geophysical Research: Solid Earth, 120, doi:10.1002/2014JB011788.

2.1 Abstract

Probing the effects of a transient stress on the timing of an earthquake occurrence is necessary for understanding the remote interaction of large-magnitude events. Global catalog data containing 35 years of M≥5.5 earthquakes allows exploration for periods of enhanced or suppressed seismic activity. We consider 113 M≥7.5 mainshocks between 1977-2012 and focus on seismic activity on time scales from seconds to days following these mainshocks. We search for evidence of dynamic triggering of large-magnitude events similar to the previously observed global increase during the first few days following the 2012 M8.6 Indian Ocean mainshock. We restrict the analysis to regions of elevated strain during the passage of surface waves. Using a threshold of 0.1 μstrain (∼3 kPa) and a temporal window of ±1-year, we stack daily seismicity rate curves using the exclusion-zone declustered M≥5.5 pre- and postshocks in order to resolve deviations from the background rate. Our results do not indicate a significant change in activity for at least 10-days when considering the collective set of 113 mainshocks and subsets at M8.0 and M8.5 thresholds. The results also do not indicate immediate triggering of M≥5.5 events. We do find two instances of increased seismicity in the elevated strain region within 10-days. These increases are subsequent to two mainshocks, the 1977 M8.3 and 2012 M8.6, both located in the Indian Ocean. We conclude that a global change in M≥5.5 earthquake rates following a transient stress from distant earthquakes is a rare occurrence.

2.2 Introduction

The phenomenon of triggered earthquakes provides insight into the state of stress on a fault prior to nucleation and the conditions required for rupture initiation. Studies of earthquake triggering involve spatiotemporal characterization of known stress perturbations and the associated seismic activity at various distances from a mainshock. In the near field, the region within 2-3 fault lengths of the rupture, static stress changes from a fault offset induce aftershock sequences that correlate in space and time with the stress perturbation (Freed, 2005; Harris, 1998). Within this near-field aftershock zone, a static stress transfer of 10 kPa or more is found to promote or suppress aftershock sequences, which can include large earthquakes, thereby altering the time to failure in the earthquake cycle (Reasenberg and Simpson, 1992; Stein, 1999). Complementing the near-field static stress change is the dynamic stress perturbation during the passage of seismic waves (Harris and Archuleta, 1991; Rybicki et al., 1985; van der Elst and Brodsky, 2010). Investigations into the effect of a strong dynamic pulse of energy in combination with the static stress change show that near-field aftershock sequences are enhanced by dynamic triggering (Parsons, 2002; Pollitz and Johnston, 2006). One method to separate the effect of static and dynamic stress perturbations is to consider remote earthquakes at distances of negligible static stress changes (Felzer and Brodsky, 2005; Kato et al., 2013; Richards-Dinger et al., 2010; van der Elst and Brodsky, 2010). Conversely dynamic stress shadows defined as quiescent periods at remote distances are possible following a transient stress (Parsons, 2005; Pollitz, Bürgmann, et al., 2014).

Widespread recognition of dynamically triggered earthquakes began after the 1992 M7.3 Landers earthquake in southern California triggered earthquake sequences at distances more than 1250 km from the epicenter, with many of these locations associated with geothermal or volcanic activity (Gomberg and Bodin, 1994; Hill, Reasenberg, et al., 1993). Brodsky, Karakosta, et al. (2000) found evidence for dynamic triggering in non-volcanic regions following the 1999 M7.4 Izmit, Turkey earthquake. Continued efforts have shown that at remote distances, beyond 2-3 fault lengths, transient stresses have the potential to immediately trigger microearthquakes (M<3.5) as well as non-volcanic tremor during or soon after the passage of seismic waves (Aiken, Peng, and Chao, 2013; Brodsky and Prejean, 2005; Gomberg, Bodin, et al., 2004; Peng, Hill, et al., 2010; Peng, Wu, et al., 2011; Prejean, Hill, et al., 2004; Velasco et al., 2008). Dynamic stress levels found to trigger microseismicity and non-volcanic tremor are on the order 1-10 kPa (Peng, Vidale, et al., 2009; Tape et al., 2013). These low-magnitude events and non-volcanic tremor often occur during the passage of the long-period surface waves and can go undetected in sparsely monitored regions. Less frequently, triggering of earthquakes ranging from $3 < M < 5$ is detected during the passage of the surface wave (Hill and Prejean, 2007; Husker and Brodsky, 2004; Pankow et al., 2004; Tape et al., 2013). Other studies have also observed delayed dynamic triggering; i.e. a temporal gap between a transient stress and an increase in remote seismic activity initiating hours to days after the stress perturbation and persisting for time period up to 2 weeks (Pankow et al., 2004; Peng, Wu, et al., 2011; Pollitz, Stein, et al., 2012). Velasco et al. (2008)

performed a systematic global search of waveform data and detected a significant increase in microseismicity for ∼0.8 hours following the surface wave arrival from 15 remote M>7.0 earthquakes. Their results are restricted to regions with broadband monitoring capabilities but independent of tectonic environment, which suggests dynamically triggered earthquakes could initiate due to multiple physical mechanisms.

The dynamic triggering of M>5 earthquakes is rarely observed beyond the near-field aftershock zone (Parsons and Velasco, 2011), but the phenomenon is documented for a few mainshocks. One example is the 1992 M5.3 Little Skull Mtn. event that occurred 22-hours after the 1992 M7.3 Landers mainshock in southern California (Gomberg and Bodin, 1994). The Little Skull Mtn. earthquake was the largest dynamically triggered event associated with the 1992 Landers mainshock and was preceded by a foreshock sequence that initiated at the time of the Landers event. Gomberg and Bodin (1994) report the fault rupture plane was preferentially oriented with respect to the peak dynamic strain of 4 μstrain calculated for the hypocentral depth. A second example is the M5.2 earthquake and an associated earthquake swarm in the Gulf of California that initiated in the hours following the passage of surface waves from the 2011 M9.0 Tohoku mainshock (Gonzalez-Huizar, Velasco, et al., 2012). A third example, and arguably the largest dynamically triggered earthquake, is the 2013 M7.5 Craig, Alaska earthquake that occurred 3 months following the M7.7 Haida Gwaii earthquake (Gomberg, 2013). The final event that had multiple triggered earthquakes, is the 2012 M8.6 Indian Ocean earthquake with 6 days of above-average global seismicity for M≥5.5 earthquakes followed by a 95-day period of global quiescence for M≥6.5 events (Pollitz, Bürgmann, et al., 2014; Pollitz, Stein, et al., 2012). The lack of additional observations of dynamic far-field triggering of M≥5 earthquakes suggests that these larger events are less responsive to transient stress changes (Parsons, Kaven, et al., 2012).

Questions remain regarding large-magnitude earthquakes remotely triggering other M≥5.5 earthquakes and the delay time for observable changes in earthquake activity (Gomberg and Sherrod, 2014; Pollitz, Stein, et al., 2012). In this study, we systematically examine global seismicity of M≥5.5 events in the months following the passage of large-amplitude surface waves at remote distances beyond the aftershock zone for M≥7.5 mainshocks. Our goal is to investigate if a resolvable triggering signal, either immediate or delayed within the first 10-days of the mainshock, exists in the catalog records. Additionally, we explore the data for periods of reduced global seismicity following a transient stress, i.e. a dynamic shadowing effect (Pollitz, Bürgmann, et al., 2014). This study relies on a systematic approach that examines 113 M≥7.5 events in 35-years of earthquake catalog data as a collective set and separated by fault mechanism. The techniques of this study allow us to test for periods of enhanced or suppressed activity following a transient stress perturbation by producing rate curves of far-field seismic activity for each mainshock.

2.3 Systematic catalog analysis for delayed dynamic triggering

2.3.1 Terminology

Throughout the paper, we will follow the terminology described here. A M≥7.5 earthquake is referred to as a mainshock, if it did not occur within 2.5 fault lengths and 36 hours of a preceding M≥7.5 event. A preshock is any event occurring before the mainshock within the elevated strain region described in the Methods section. Similarly, a postshock is any event occurring during or after passage of the mainshock surface waves within the elevated strain region. Here, we only consider M≥5.5 events as pre- and postshocks. To note, we do not use aftershock to describe the far-field earthquakes because we are interested in events beyond the region normally associated with that term and postshocks can be larger than the mainshock (Chen et al., 2013). The near field encompasses the region 2.5 fault lengths from a mainshock. The far field is the region beyond the near field. Static triggering can produce near-field postshocks. Dynamic triggering is the occurrence of postshocks during the passage of seismic waves. Delayed dynamic triggering can produce a postshock in the days following the passage of seismic waves. Dynamic stress shadowing is a seismic quiescent period following a transient stress.

2.3.2 Methods

Our analysis examines only the far-field, M≥5.5 seismic activity following M≥7.5 mainshocks in a global catalog. We build on the results by Parsons and Velasco (2011) that indicate no increase in 5<M<7 events following M≥7 mainshocks at distances greater than 1000 km from the epicenter. We allow for M≥7.5 events to trigger other large events and stack the seismicity to resolve a possible increase in the 10-days following the mainshocks. Our search area is spatially limited, using a model to define the region of elevated dynamic strain that is unique to each mainshock. This allows us to consider only far-field activity occurring in regions that are dynamically strained during the passage of seismic waves. We adopt a peak dynamic strain threshold of ≥0.1 μstrain (corresponding to a transient stress of ∼3 kPa) that has been previously shown to trigger activity in seismically active areas (Peng, Hill, et al., 2010; Pollitz, Stein, et al., 2012; van der Elst and Brodsky, 2010).

Earthquake catalog

Data from the Global Centroid Moment Tensor (GCMT) catalog between January 1976 and December 2013 containing 39,989 events was used for the analysis (Dziewonski, Chou, et al., 1981; Ekstrom et al., 2012). The GCMT catalog includes a moment magnitude and the moment tensor solution making it ideal for decomposing the earthquakes by fault mechanism. The magnitude of completeness was calculated using the maximum curvature (Gutenberg and Richter, 1944) and maximum likelihood methods (Aki, 1965; Wiemer and Wyss, 2000),

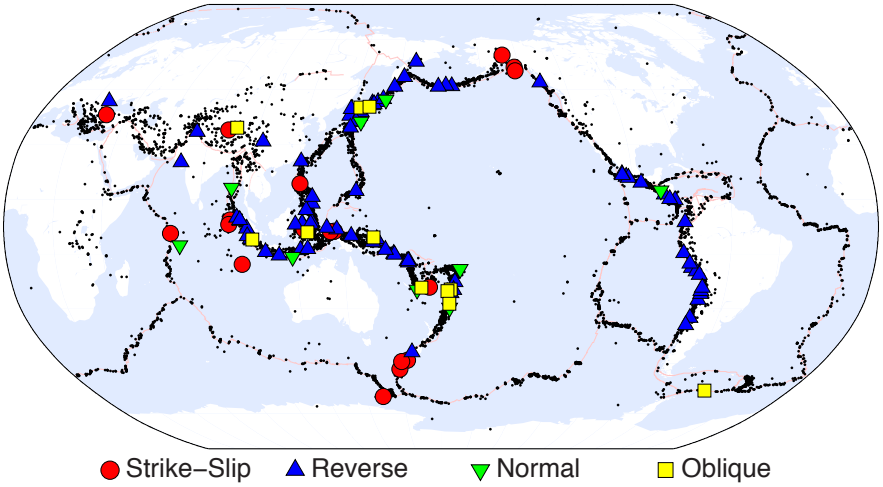

Figure 2.1: Locations of the 122 M≥7.5 mainshocks and exclusion-zone declustered M≥5.5 seismicity between 1977-2012 in the GCMT catalog. Symbols indicate the fault type determined using the plunge of the compression, tension, and null axis from the GCMT moment tensor solution. Black dots indicate the M≥5.5 trigger candidates.

finding a completeness level of M5.3 and M5.7, respectively. Due to the uncertainty in the magnitude of completeness we use the average of the two methods, M5.5, throughout this study (Gomberg and Sherrod, 2014). The event depth was limited to <100 km, with 77% of the events at a depth less than 35 km. The final catalog contains 12,707 M≥5.5 earthquakes meeting these criteria for the analysis.

The analysis considers all the 122 M≥7.5 mainshocks from 1977 through 2012 as sources of a transient strain perturbation (Figure 2.1). Each mainshock is assigned a faulting mechanism using the moment tensor solution to calculate the compression (P), tension (T), and null (B) axis plunge. Following Mallman and Parsons (2008), the earthquakes are classified with a T-axis plunge ≥50° as reverse events, a P-axis plunge ≥60° as normal events, and a B-axis plunge ≥60° as strike-slip events. All remaining events were classified as oblique. This allows the mainshocks to be characterized by mechanism for separate analyses. The time frame considered is a ±1-year window of cataloged seismicity around each mainshock in order to represent the natural variability in earthquake occurrence. Mainshock sequences are removed from the catalog if multiple M≥7.5 earthquakes are present within 36 hours of the original mainshock and within 2.5 fault lengths. When removing mainshocks the largest earthquake in the sequence is kept for the analysis. This allows the removal of rapid sequences of mainshocks such as the 2011 M9.0 Tohoku-Oki and the two M≥7.5 aftershocks that occurred within one hour. Similarly, the 36-hour time window removes mainshock clusters like the 2000 Papua New Guinea earthquake sequence of three M≥7.5 mainshocks that occurred within 35 hours [Park and Mori, 2007]. In total this procedure removes 9 M≥7.5 earthquakes and leaves 113 M≥7.5 mainshocks.

Declustering

We avoid using a declustering method that requires fitting multiple model parameters; instead we implement an exclusion-zone method for each mainshock in the catalog (Gomberg and Sherrod, 2014; Pollitz, Stein, et al., 2012; Shearer and Stark, 2012). The radial exclusion zone extends 2.5 characteristic fault lengths from each mainshock, calculated using the fault type and magnitude (Wells and Coppersmith, 1994), and removes all near-field events for a period of 1 year following all M≥7.5 mainshocks. The exclusion method is repeated for the $5.5 \leq M \leq 7.5$ catalog, removing earthquakes in the exclusion zone of each event within 24 hours and applying a minimum distance of 100 km while keeping the first. The exclusion-zone declustering method removes 1,849 near-field events for all mainshocks and 1,046 far-field events leaving 9,812 events for the analysis.

Defining spatial regions

Seismicity is selected from a spatial region of high dynamic strain determined for each mainshock, which is defined by an annulus centered at the epicenter of the mainshock that is scaled by the magnitude (Figure 2.2). The far-field region of interest is restricted to locations where surface waves are the primary source of a transient strain. The inner limit is 2.5 fault lengths, as previously determined during the declustering procedure. The distal limit of the search area is calculated for each mainshock using the minimum wave amplitude that corresponds to an estimated strain (van der Elst and Brodsky, 2010) with a threshold of 0.1 μstrain (Equation 2.1 and 2.2).

$$\varepsilon \approx \frac{V}{C} \approx \frac{A_{max} 2\pi}{CT} \tag{2.1}$$

$$log_{10} A_{max} = M_S 1.66 log_{10}(\Delta) - 2 \tag{2.2}$$

Here V is particle velocity, C is wave velocity, A_{max} is maximum displacement in micrometers, T is dominant period in seconds, M_S is surface wave magnitude, and Δ is distance (Lay and Wallace, 1995). The strain is estimated from Equation 2.1 using the amplitude as a function of distance and magnitude, as described in Equation 2.2. This study assumes a surface wave velocity of 3.5 km/s and a dominant period of 20 seconds. These are representative parameters for Rayleigh waves (Lay and Wallace, 1995). As noted by van der Elst and Brodsky (2010), if the Love wave results in the largest surface displacement, the assumptions for Equation 2.1 can overestimate the maximum strain by 20% if a constant period of 20 s is assumed. Assuming representative elastic moduli for the lithosphere (shear modulus of 30 GPa, Poissons ratio of 0.25) this corresponds to a shear stress transient of about 3 kPa, an order of magnitude greater than stress perturbation that induce non-volcanic tremor (Thomas et al., 2009).

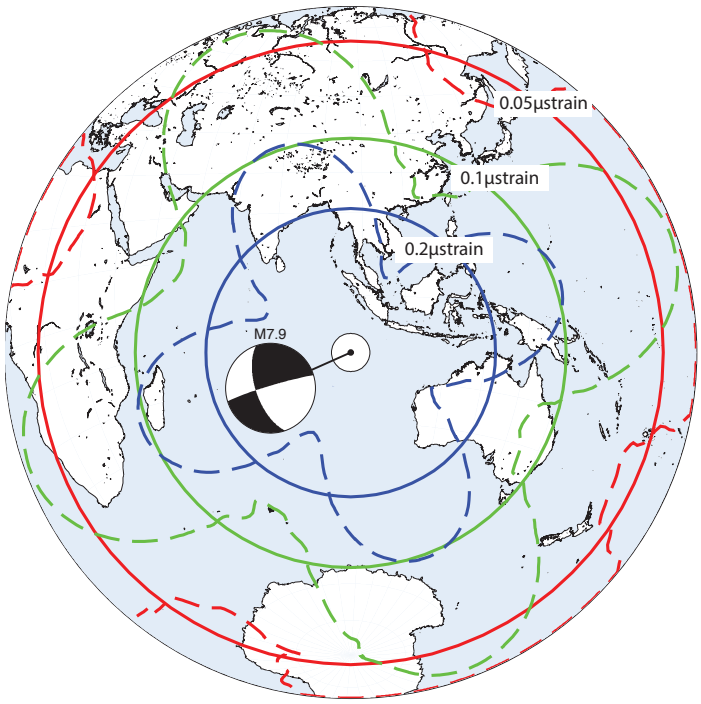

Figure 2.2: Extent of dynamically strained region calculated for the 06/18/2000 M7.9 earthquake in the Indian Ocean using the empirically derived shear-strain values (solid circles) from the magnitude and the modeled strain from synthetic waveforms (dashed lines). Shown are three regions of peak dynamic strain calculated for 0.2 μstrain (blue), 0.1 μstrain (green), and 0.05 μstrain (red). The modeled strain amplitudes are the square root of the second invariant of the deviatoric strain tensor obtained from a point-source model of surface waves generated by the event, using the focal mechanism shown from the GCMT catalog. The inner exclusion zone extends 2.5 rupture lengths from the epicenter to a distance of ∼500km and is represented as a white disk centered on the mainshock. For each mainshock, all events from the exclusion-zone declustered catalog in the high-strain region for ±1 year are used to produce the rate curves.

Synthetic waveform strain calculation

The empirical values obtained from Equations 2.1 and 2.2 do not consider the spatial pattern of dynamic strain and represent an estimated peak strain for a given distance. We complement the strain calculation from Equations 2.1 and 2.2 by modeling the expected displacements for a select group of mainshocks and the associated shear strain magnitude and duration. Seismic waves are modeled with a direct Greens function method using an isotropic PREM model on a symmetric sphere (Friederich and Dalkolmo, 1995; Pollitz, 1996; Pollitz, Stein, et al., 2012). Synthetic waveforms are produced using a point source solution at 5150 node points evenly spaced around the surface of the planet (Pollitz, Stein, et al., 2012). The mainshock moment solution, half width of the rate function, and the strike, rake, and dip of the fault plane from the GCMT catalog are used for the model calculation. The choice of nodal plane does not alter the solution and we use the parameters from the first nodal plane listed in the catalog. We treat each mainshock as a far-field point source and only consider the long-wavelength displacement. The shearing magnitude is estimated from the square root of the second invariant of the deviatoric strain tensor for each synthetic seismogram and should be considered an upper limit for the transient strain (Jaeger et al., 2007). The long-period synthetic seismograms are filtered to the GCMT half-duration time when calculating the strain field time-series. The strain duration represents the time, in seconds, above the strain threshold for each node point. The dashed contour line in Figure 2.2 illustrates the extent of the peak dynamic shear-strain field for a 06/18/2000 M7.9 strike-slip event in the southern Indian Ocean (13.47 °S, 97.17 °E) using a threshold of 0.05, 0.1, and 0.2 μstrain. Included in Figure 2.2 is the radial extent of the empirical strain calculation determined using Equations 2.1 and 2.2 shown with solid lines. We verify the results using data from the station CTAO to compare with the synthetic seismograms (Figure 2.3).

Rate Curves

We calculate the daily rate of seismicity for a ±365 day period for each mainshock using the M≥5.5 declustered catalog. The procedure is applied to all pre- and postshocks in the dynamic-triggering target region of all 113 M≥7.5 mainshocks and stacked as a whole and by fault mechanism. Curves are constructed using a moving average with a 1-day time step and 3-day half width. Pre-mainshock events are summed for the discrete time t_{before} using a bin width of [t_{before}− 3 days, min(0, t_{before}+ 3 days)]. Post-mainshocks events are summed for the discrete time t_{after} using a bin width [max(t_{after}− 3 days, 0), t_{after}+ 3days]. The rate is scaled to the correct bin width for every discrete time interval. This avoids averaging across time zero and ensures a separation between pre- and postshocks when calculating the daily rate (Pollitz, Stein, et al., 2012). The rate curves are stacked with time zero relative to each mainshock and normalized by the total number of mainshocks. We use a lower-magnitude cutoff for mainshocks of M7.5, M8.0, and M8.5. The background rate is determined using a Monte Carlo procedure that randomizes the event times in the catalog and perturbs each location by up to 50 km (Parsons and Velasco, 2011). This simulated catalog approach

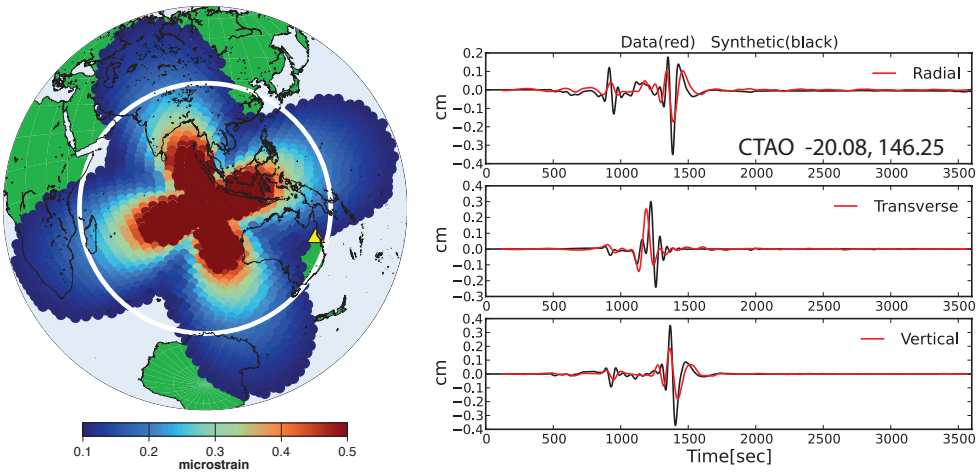

Figure 2.3: Strain field calculated for the 06/18/2000 M7.9 from the square root of the second invariant of the deviatoric train tensor, which represents the maximum shear magnitude of the strain tensor. The left panel indicates the location where 0.1 μstrain is exceeded during the passage of the seismic waves. The strain field is calculated from synthetic waveforms filtered at a period of 40s. The color scale is saturated at 0.5 μstrain to clearly represent the far-field levels. The superimposed white circle is the mainshock distance calculated using Equations 2.1 and 2.2 and used to determine the region of elevated strain for the initial rate curves. The right panel shows the synthetic seismograms with data recorded at the CTAO station (yellow triangle) to verify the calculations.

allows us to retain the spatial and temporal characteristics of the original catalog that are needed for the scaling used in our analysis. For each event a rate curve is produced using a simulated catalog for 2-years prior to the mainshock. The process is repeated 200 times and the background rate and confidence intervals are obtained from the distribution of rate curves.

2.3.3 Results

All fault types

For an observable delayed seismic response in the far field, either an increase or decrease in activity, we need a large population of mainshocks that contains multiple fault orientations and varying environments. Figure 2.4 shows the normalized daily rate curves stacked for the 113 M≥7.5, 26 M≥8.0 and 6 M≥8.5 mainshocks with time zero relative to each mainshock origin time. Since we are using a subset of declustered M≥5.5 events for each mainshock the rate curves represent the deviation in seismic activity and is reduced by the calculated background rate. The 95% confidence bounds are shown in gray. Periods of increased activity appear as peaks in the rate that occasionally exceed the 95% confidence interval. An increase

in postshock activity above the 95% level is not observed for at least 10-days after time zero for the three magnitude thresholds shown in Figure 2.4. we do not consider later pulses of activity as evidence for a systematic increase in far-field seismicity.

The first postshock in the M≥7.5 stacked rate curves occurs ∼8.5 hours following the mainshock (Figure 2.5). The M5.8 postshock is located ∼1,050 km from the 1991 M7.6 mainshock that occurred offshore from Costa Rica. No evidence for immediate triggering of M≥5.5 postshocks is observed in our study. Additionally, our results do not indicate a dynamic shadowing effect following the mainshocks. The results do indicate a subtle increase in daily rates but changes in activity are not outside the statistical confidence intervals.

Mainshocks by fault type

The mainshocks are separated by fault type and rate curves are produced in order to test if a particular mainshock faulting mechanism results in observable changes. The motivation for this separation is the difference in radiation pattern and dominant surface wave associated with differing fault mechanisms. The decomposition produces similar distributed pulses in activity above the 95% confidence level as are observed in the initial combined set of mainshocks. Figure 2.6 contains the rate curves for the M≥7.5 mainshock decomposed into 17 strike-slip, 77 reverse, 8 normal, and 11 oblique events. Figure 2.6a shows the strike-slip events, which indicates a sharp increase in daily rate following the mainshock. This increase in the rate curve immediately after the mainshock is strongly influenced by the 2012 M8.6 Indian Ocean event, which is shown to have increased global seismicity for 10-days (Pollitz, Stein, et al., 2012). Also evident in the strike-slip rate curve is a period of activity below the confidence interval from days 25 to 33 after the mainshock. The reverse events (Figure 2.6b) indicate a 3-day increase in activity 12 days after the mainshock. No sustained decrease in activity is observed for the reverse mainshocks. The normal mainshocks in Figure 2.6c indicate an increase in seismicity that initiates 4 days after the mainshocks and continues for 20 days. The observed increase following the normal mainshocks appears to be dominated by a rate increase following the 1977 M8.3 event in the southern Indian Ocean. The oblique mainshocks (Figure 2.6d) do not produce a resolvable increase or decrease in activity following the mainshocks. When stacking only the largest mainshocks we are increasing the extent of the region of elevated strain but sampling with fewer mainshocks to support any observation. The rate curves for the 26 M≥8.0 mainshocks produced using Equation 1 and 2 are separated by fault type and shown in Figure 2.7. The rate curves contain 4 strike-slip, 16 reverse, 3 normal, and 3 oblique mainshocks. We observe similar rate increases for the strike-slip and normal fault types that are sustained for 10 and 21 days, respectively.

Strain field derived from synthetic waveforms

To further test the significance of the possible far-field increase in seismicity following the strike-slip mainshocks we calculate a global strain field using synthetic seismograms derived from the GCMT moment tensor solution for the 17 strike-slip, 3 M≥8 normal mainshocks,

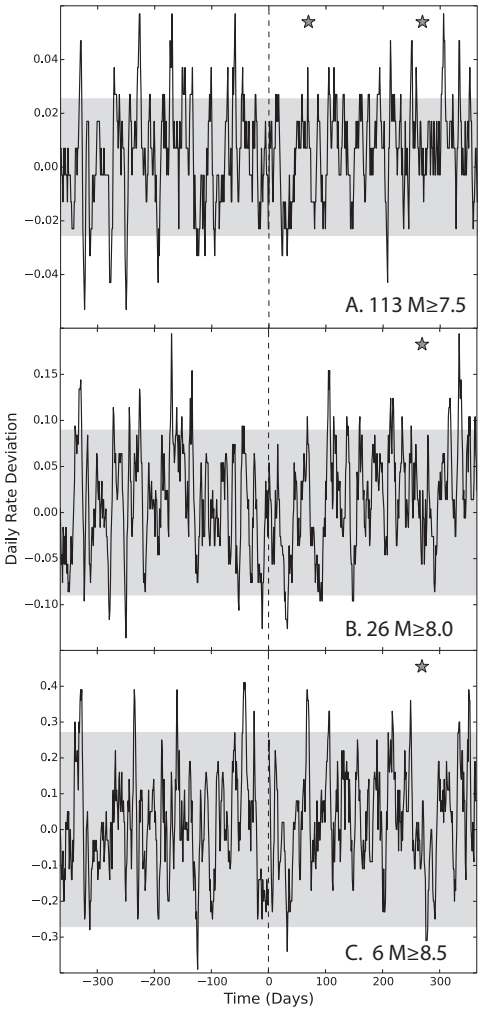

Figure 2.4: Stacked seismicity rate curves of exclusion-zone declustered M≥5.5 events in the region of elevated strain (≥0.1 μstrain from Equation 2.1 and 2.2) for populations of mainshocks with different magnitude ranges, with time zero relative to each mainshock. The curve indicates the deviation from the normalized background rate for the population using a moving average with a 1-day step and 3-day half width. The gray shading represents the 95% confidence interval calculated using only events within the defined high-strain region during a 2-year period prior to the mainshock. Stars indicate the occurrence of a M≥7.5 mainshock in the elevated strain area when calculating the rate curve. Pulses of activity, as well as brief periods of low activity, exist throughout the 2-year period but do not correlate with the timing of the mainshock. (a) shows the stacked rate curves for 113 M≥7.5 mainshocks between 1977-2012. (b) only considers the 26 M≥8.0 mainshocks and (c) is produced using the 6 M≥8.5 events.

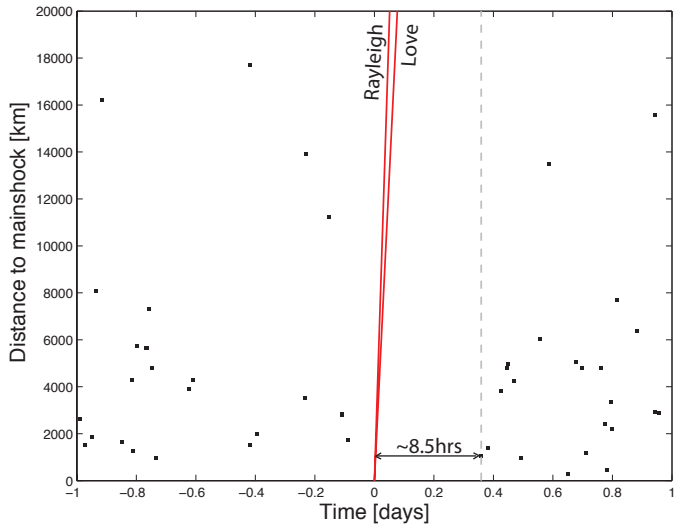

Figure 2.5: Seismicity (M≥5.5) for ±1-day relative to the 113 M≥7.5 stacked mainshocks. The red lines indicate the arrival time of the Love and Rayleigh waves. The times of the M≥5.5 events shown is relative to the associated mainshock and events are selected from the declustered far-field pre- and postshocks. The first event is a M5.8 that occurs ∼8.5 hours after and ∼1050 km away from the 1991 M7.6 mainshock located offshore Costa Rica.

and 5 M≥8.5 reverse mainshocks. We are redefining the elevated strain field from the original circular region determined using Equations 2.1 and 2.2 and use the modeled shear-strain magnitude and duration to represent a strain field based on the seismic radiation pattern. The computed strain field (≥0.1 μstrain) includes a larger region defined by the radiation pattern of the focal mechanism (Figure 2.2). The rate curves for the strike-slip mainshocks using the redefined strain field are shown in Figure 2.8. The modeled strain field increases the number of events in the far field of the 17 strike-slip mainshocks by 429 for a total of 3004 earthquakes. We investigate the influence of the 2012 M8.6 Indian Ocean earthquake on the analysis and find 20% of the 3004 events used to produce the rate curve in Figure 2.8a are associated with the 2012 event. The elevated seismicity is clearly observed in the top panels of Figure 2.8 for the M7.5 and M8.0 magnitude threshold, consistent with the results shown in Figures 2.6a and Figure 2.7a. The analysis is repeated with the 2012 M8.6 Indian Ocean mainshock removed and the results are shown in the bottom panels of Figure 2.8 where the elevated seismicity is no longer observable. Similar steps were taken to produce and stack rate curves for the normal mainshocks that indicate elevated rates. The increase is found to be due to activity following the 1977 M8.3 mainshock in the southern Indian Ocean.

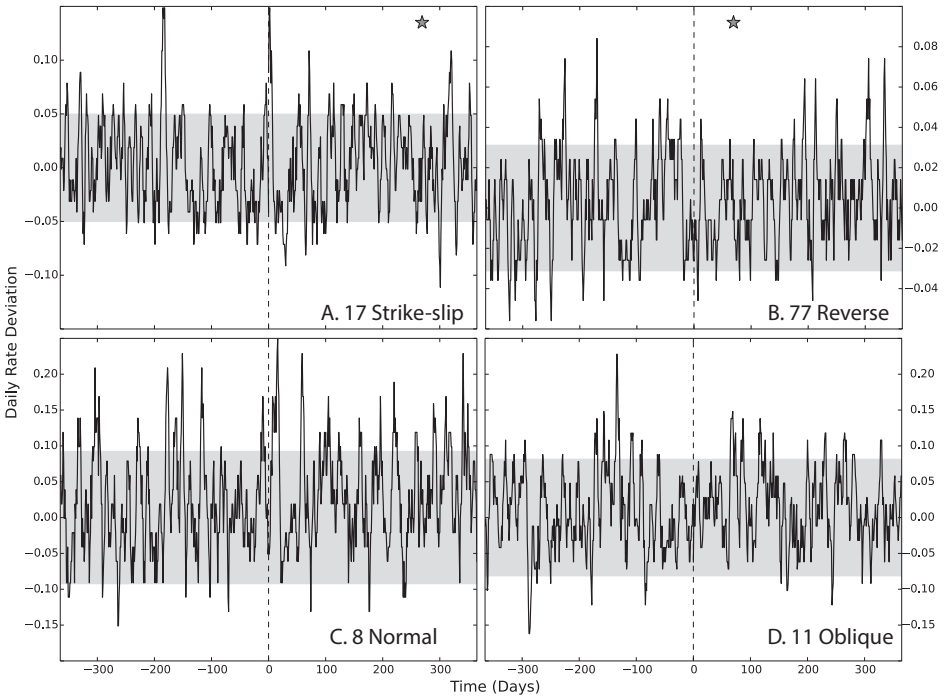

Figure 2.6: The 113 M≥7.5 mainshocks are separated by fault type and M≥5.5 exclusion-zone declustered seismicity is stacked to produce rate curves. Shown is the deviation from background rates with the 95% confidence interval in gray. Stars indicate the occurrence of a M≥7.5 mainshock in the circular ≥0.1 strain area calculated from Equation 2.1 and 2.2. The strike-slip and normal mainshocks indicate a period of elevated seismicity during the first 10-days following the mainshock. The elevated seismicity rate following strike-slip mainshocks is dominated by the 2012 M8.6 Indian Ocean mainshock. As shown in Figure 6 the rate increase during the first 10-day period is not present when the 2012 mainshock is removed from the rate curve. The increase following the normal mainshocks is attributed to the 1977 M8.3 mainshock.

2.4 Discussion

2.4.1 Findings and comparison with prior results

We focus our study on the remote triggering of M≥5.5 earthquakes and analyze the data for a systematic change in earthquake rates rather than focusing on single postshocks as potential triggered candidates. Our results indicate no immediate far-field triggering of M≥5.5 and are consistent with Parsons and Velasco (2011) who do not find immediate triggering of 5 < M < 7 events at distances greater than 2-3 rupture lengths following 205 M≥7 mainshocks. Our findings show that the first M≥5.5 postshock occurs ∼8.5 hours following the passage of seismic waves (Figure 2.5). A suppression of earthquake rates is also not observed in the M≥7.5 rate curves shown in Figures 2.4 and 2.6. For the M≥8.0 strike-slip mainshocks,

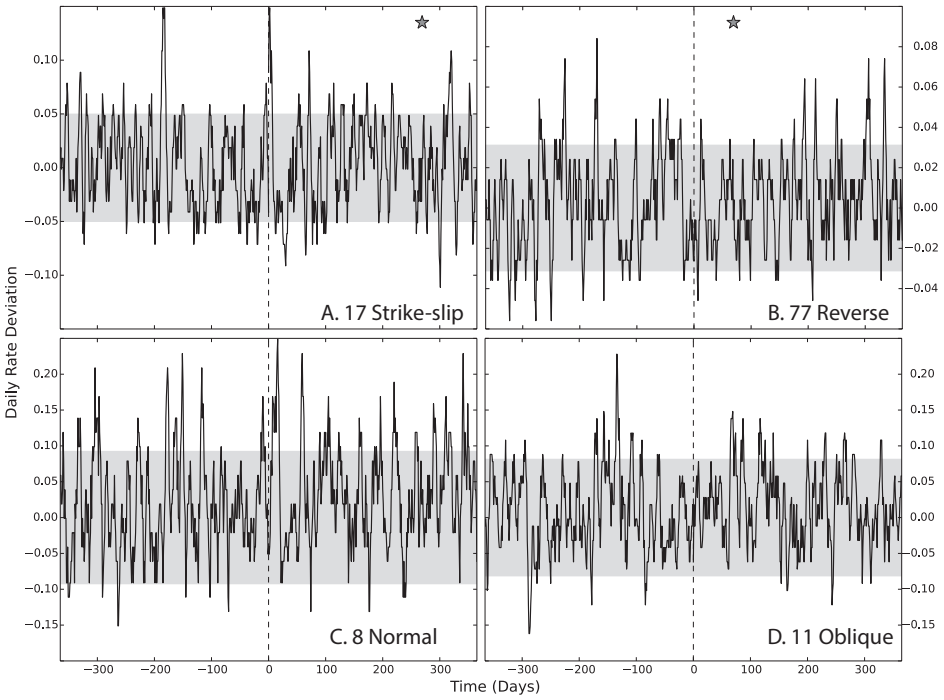

Figure 2.7: Stacked rate curves for M≥5.5 seismicity in the high strain region calculated using Equation 2.1 and 2.2 for the 26 M≥8.0 mainshocks are separated by fault mechanism. Shown is the deviation from background rates with the 95% confidence interval in gray. The strike-slip (a) and normal (c) mainshocks both indicate a period of elevated seismicity during the first 10 days and 20 days after time zero, respectively. The 16 reverse (b) and 3 oblique (d) mainshocks do not produce a significant increase. None of the rate curves show a prolonged period of reduced activity below the confidence intervals.

rate curves shown in Figure 2.8 indicate a period of reduced seismicity from 20 to 23 days following the mainshock. Similar periods of reduced activity are also present in the months before and well after the mainshock, and may represent natural fluctuations in seismicity. While the period of enhanced seismicity after the 2012 M8.6 Indian Ocean earthquake was followed by an unusual 95-day long absence of M≥6.5 events (Pollitz, Bürgmann, et al., 2014), we do not find a corresponding systematic reduction of M≥5.5 events.

Recent studies have suggested that the largest M≥8.5 mainshocks are capable of producing an increase in global seismicity (Pollitz, Stein, et al., 2012). We test this by exploring mainshock magnitude ranges above M7.5, M8.0, and M8.5 and find observable rate changes are associated only with a few individual mainshocks. As noted by Pollitz, Stein, et al. (2012), the two day rate increase following the five largest subduction events is less than the increase following the 2012 M8.6 Indian Ocean mainshock. Figure 2.4c includes the five largest subduction events and the 2012 M8.6 Indian Ocean mainshock, which indicates a subtle increase that is difficult to separate from the long-term variability in seismicity and does

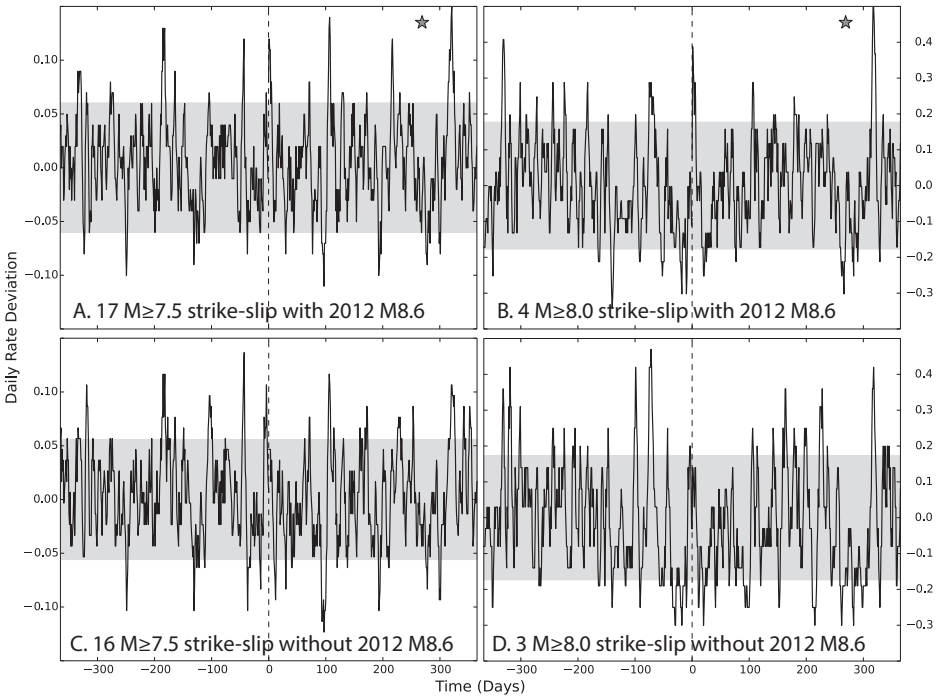

Figure 2.8: Seismicity rate curves for M≥5.5 events in the region of elevated strain (≥ 0.1 μstrain) for strike-slip events calculated using the synthetic waveforms. The strike-slip mainshock rate curves illustrate the influence of the 2012 M8.6 Indian Ocean mainshock and its associated elevated remote seismicity. (a), (b) Observed deviation of M≥5.5 event rates in the high-strain search areas for each mainshock including the 2012 M8.6 Indian Ocean earthquake for M≥7.5 and M≥8 strike-slip events. (c), (d) Rate variations with the 2012 M8.6 Indian Ocean mainshock removed from the catalog. No increase during the first 10-days above the confidence interval is observed when performing this test at the M≥7.5 and M≥8.0 threshold.

not exceed the 95% confidence bounds. We also consider the possible role of mainshock fault mechanism, which produce different amplitudes and patterns of Rayleigh and Love waves, but do not find substantially different rate curves as a function of faulting style (Figure 2.6). By extending the period of seismicity to many months before and after the mainshock, we observe the natural fluctuations in M≥5.5 events and avoid interpreting such background variations as significant rate changes. Several times, the calculated daily rate during the two-year period exceeds the confidence intervals but is not associated with transient seismic waves. The variability in rate is expected due to the stochastic occurrence of seismic events.

2.4.2 Target Selection, data windowing, and potential caveats

A unique feature in our study is the varying spatial window that selects the seismicity rate in regions of the largest dynamic strain. Our spatial scaling method tests the importance of wave amplitude with respect to the triggering potential. The justification of this scaling relationship is to limit the selection of postshocks to far-field regions that experience a substantial transient strain. We calculate rate curves for 113 M≥7.5 mainshocks using strain thresholds of 0.05, 0.1, and 0.2 μstrain and do not find notable differences in the distribution of postshock activity. Therefore, we maintain a strain threshold of 0.1 μstrain for the analysis. One limitation to our method is not considering the receiver fault orientation with respect to a transient strain when selecting possible trigger candidates (Gonzalez-Huizar and Velasco, 2011; Hill, 2012). Resolving the Coulomb shear and normal stress changes for each postshock considered would provide a better metric for the triggering potential of a transient strain but is beyond the scope of this study.

The postshock selection process is central to the results presented throughout this study and can be influenced by the preprocessing methods applied to the original set of cataloged earthquakes. Our study limits all mainshocks and postshocks to depths <100km and does not consider mainshock-postshock interaction that has been observed in deep-focus earthquake sequences (Tibi et al., 2003). We implement an exclusion zone that eliminates all postshocks within 2.5 fault lengths of the epicenter in order to avoid the classical aftershock zone produced by both static and dynamic stress changes. Our tests do not indicate a significant change in the results by decreasing the exclusion zone to a factor of 2 or increasing to a factor of 4 of the estimated fault lengths. Reducing the exclusion zone distance below a factor of 2 introduces local aftershocks into the rate curves. We also test the temporal window length for excluding near-field events and observe insignificant rate differences when shortening to a 35-day window from a 1-year window (Figure 2.9). Similarly, we evaluate rate curves without the far-field declustering of local aftershocks and obtain similar results.

The choice of a magnitude threshold of M5.5 represents the completeness of the catalog. Using the more conservative magnitude of completeness of M 5.7 for the GCMT catalog would reduce the number of events in the selection process. Performing the analysis at the higher magnitude of completeness does not significantly alter the results. Conversely, using events down to M5.0 increases the number of events considered and does change the background rate. Calculating rate curves using the lower magnitude threshold does not produce any additional deviations in seismic activity immediately following the transient strain. Therefore, we maintain a threshold of M5.5 with regards to the magnitude of completeness calculated. The choice of window width when smoothing the data set can also influence the results. Here the rate curves are smoothed using a 1-day bin with a 3-day half-width. Other studies have implemented 1-month windows over restricted spatial subsets (Gomberg and Sherrod, 2014) and 1-day windows on global scales (Pollitz, Stein, et al., 2012). We tested different windows as short as 1-day and up to 1-month without significant changes to our results.

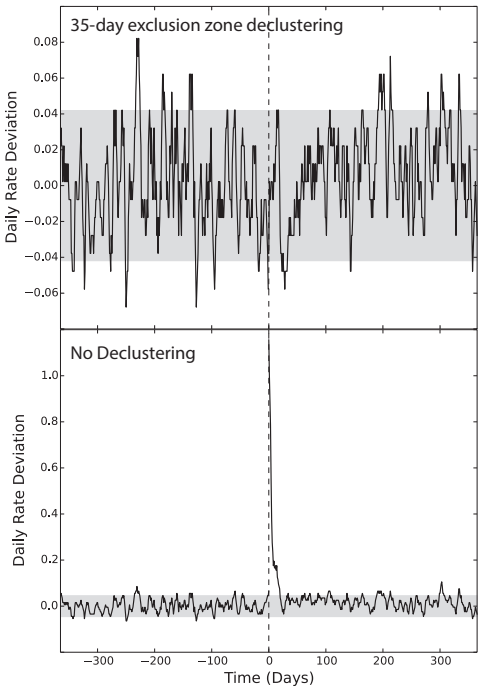

Figure 2.9: Testing the declustering influence by changing the spatial and temporal windowing. (Top) Rate curve containing 113 M7.5 mainshocks with a 35-day exclusion zone for all near-field events and no far-field declustering. (Bottom) Rate curve containing 113 M7.5 mainshock with ans exclusion zone distance of 0.5 fault lengths.

2.4.3 Significant rate changes

The rate curves indicate significantly elevated rates of far-field seismic activity in the immediate days following only two large mainshocks, each with different characteristics. These are the 1977 M8.3 normal and the 2012 M8.6 strike-slip earthquakes, both located in the Indian Ocean (Figure 2.10). The 1977 M8.3 mainshock produced a delayed response on the order of days. The first postshock outside the exclusion zone is a M5.5 two days after the mainshock with the far field not reaching significantly elevated rates until 10 days afterwards followed by about two weeks of enhanced activity. This delay time subsequent to the 1977 M8.3 is considerably greater than that found for the 2012 M8.6 Indian Ocean mainshock, which is followed by four M≥5.5 postshocks in the first 24 hours, the first being a M6.0 14 hours after the passage of the seismic waves. Pollitz, Stein, et al. (2012) show the significance of the 2012 M8.6 Indian Ocean earthquake triggering with respect to a global background rate. This study does not observe a similar increase when combining 35 years of M≥5.5 seismicity following 113 large mainshocks indicating the uniqueness of the 2012 M8.6 Indian Ocean earthquake. If this earthquake represents a unique occurrence of far-field triggering of M≥5.5 events, then what are the requirements for a large magnitude earthquake to trigger other large magnitude earthquakes at remote distances?

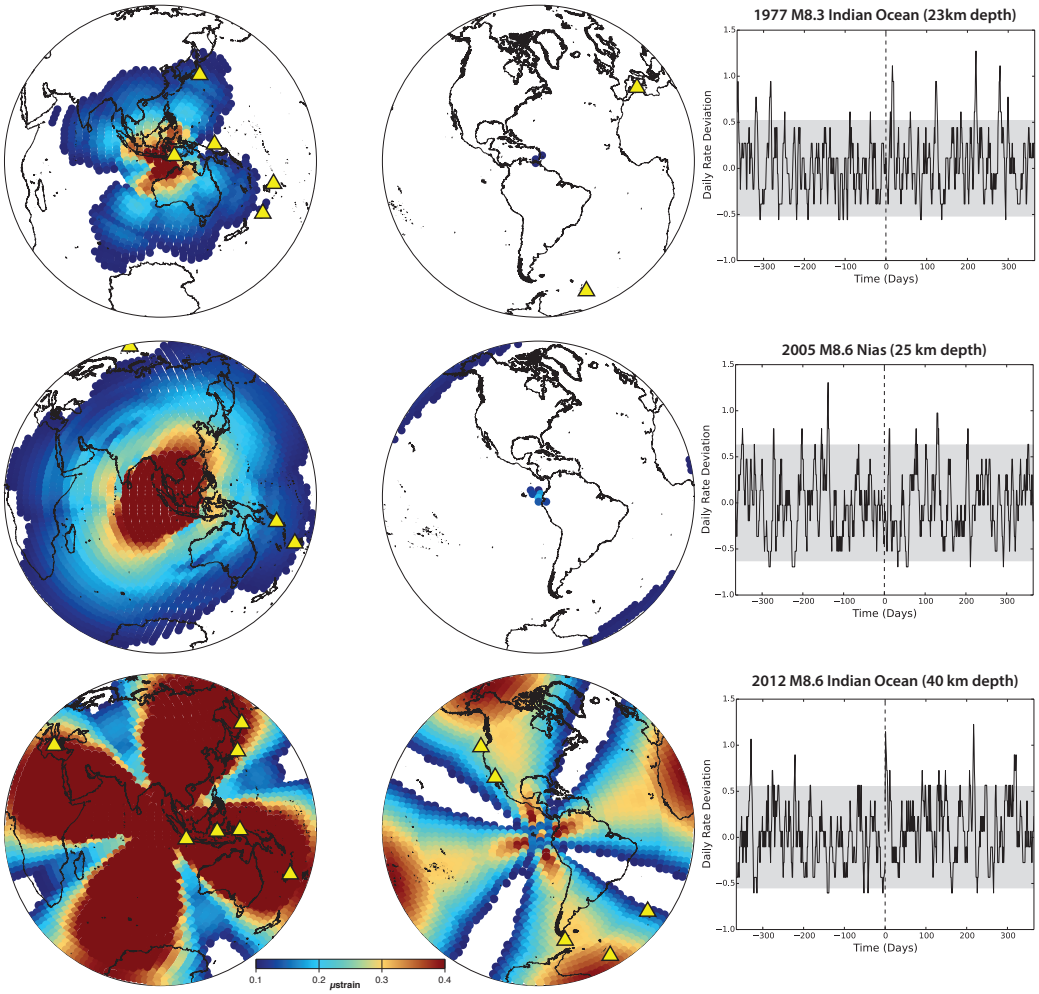

Figure 2.10: Comparison of modeled shear strain for three M≥8 mainshocks located in the east Indian Ocean with different magnitudes, centroid depths, and fault mechanisms. The spatial coloring represents the peak shear strain calculated from the square root of the second invariant of the deviatoric strain tensor using the strain time series filtered to 80 seconds. The color scale is saturated at 0.4 μstrain. Yellow triangles represent the far-field M≥5.5 seismic events for 10 days following the mainshock. To the right is the seismicity rate curve for the modeled event shown to the left. The top panel shows the 1977 M8.3 Indian Ocean normal event, the middle panel represents the 2005 M8.6 Nias subduction thrust mainshock, and the bottom panel is produced using the 2012 M8.6 Indian Ocean strike-slip event, with three M≥5.5 postshocks occurring within 24 hours of the mainshock.

The 2012 M8.6 Indian Ocean earthquake is the largest strike-slip event recorded with modern instrumentation and was comprised of a complex rupture sequence breaking deep into the mantle lithosphere (McGuire and Beroza, 2012; Meng, Ampuero, et al., 2012). The transient stress during the passage of the surface waves apparently was large enough to advance the earthquake cycle of multiple M≥5.5 events. The delayed dynamic triggering of postshocks found by Pollitz, Stein, et al. (2012) occurred in regions of >0.2 μstrains lasting more than 100 s during the passage of the surface wave train. We compare the strain duration and seismicity for the 2005 M8.6 Nias subduction thrust event and the nearby 2012 M8.6 Indian Ocean mainshock (Figure 2.10 and Figure 2.11). The two mainshocks are separated by 500 km and the centroid depth of the 2005 M8.6 Nias event is 25 km, making it 15 km shallower than the 2012 M8.6 Indian Ocean mainshock. Figure 2.10 displays the difference in spatial extent of the elevated strain regions. The far-field M≥5.5 seismicity of the first ten days following the two events shown in Figure 2.10 demonstrates the lack of large events in the much smaller region of prolonged strain for the Nias earthquake. The 2005 M8.6 Nias mainshock had 3 M≥5.5 postshocks, one of which is not within the elevated strain region, whereas the 2012 M8.6 Indian Ocean mainshock had 11 postshocks all within the region of elevated dynamic strain. We cannot dismiss the postshocks following the 2005 M8.6 Nias mainshock in the elevated strain region as being triggered even though they do not result in a systematic rate increase.

Frictional instability models using rate-and-state friction parameters indicate a clock advance can occur during the passage of seismic waves, but earthquake triggering is possible only if the fault is late in its earthquake cycle (Gomberg, Beeler, et al., 1998). This leaves the possibility that the 2005 M8.6 Nias postshocks nucleation times were advanced but the delayed occurrence does not produce a distinguishable rate change, which requires multiple postshocks to significantly exceed the expected background rate of large events. A key observation for the multiple postshocks following the 2012 M8.6 Indian Ocean mainshock is the overlap of Pacific-plate boundaries with the maximum transient strain duration extending to antipodal distances. The combination of multiple critically stressed faults within the plate boundary zone in conjunction with the long duration and large amplitude of transient shaking supports the uniqueness of the 2012 M8.6 Indian Ocean global earthquake rate increase.

No immediate triggering of M≥5.5 earthquakes is observed in this study, which agrees with previous results (Parsons and Velasco, 2011), but seems to be in contradiction to the evidence for dynamically triggered microseismicity and non-volcanic tremor. Using the Guttenberg-Richter relationship and extrapolating results of small-event triggering for 205 M ≥ 7 mainshocks, Parsons and Velasco (2011) estimate a total of 25 M≥6.0 earthquakes are expected to occur within 15 minutes of the surface waves. Instead, we find that the first M≥5.5 postshock following the 113 mainshocks we consider does not occur until 8.5 hours later. Parsons and Geist (2014) also observed an 8-9 hour delay in M>5 using a compilation of local catalogs, but no physical explanation exist for this apparent delayed phenomenon. The 2011 M9.0 Tohoku mainshock did not produce an increase in M≥5.5 postshocks but did immediately trigger non-volcanic tremor and M≤5.0 postshocks at remote distances (Chao et al., 2013; Gonzalez-Huizar, Velasco, et al., 2012; Kato et al., 2013). Similarly, the

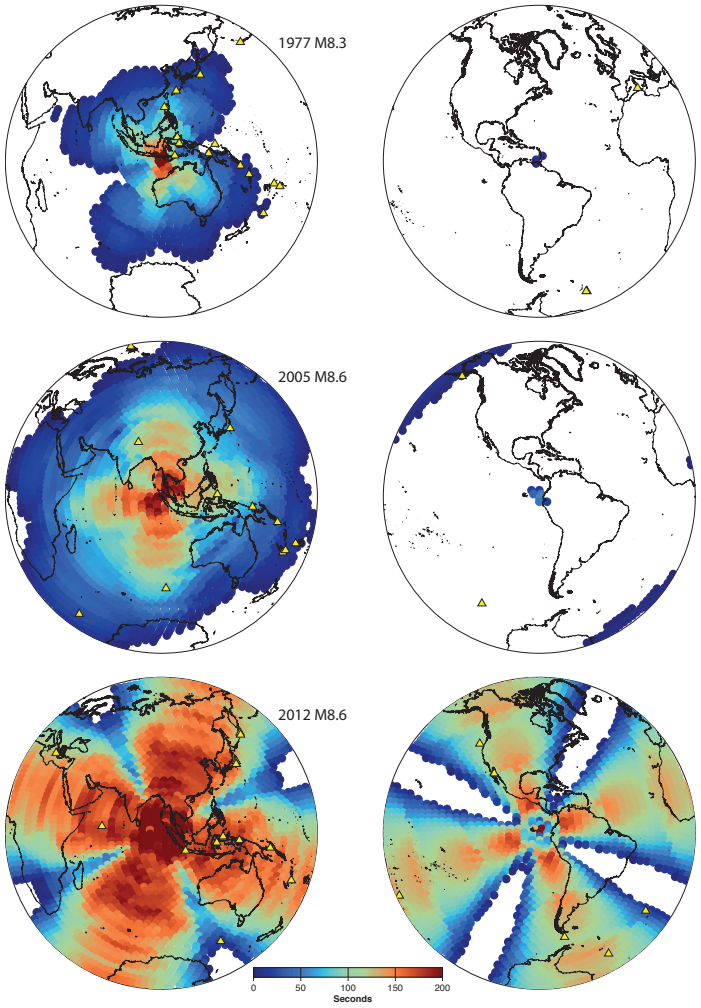

Figure 2.11: Strain duration comparison for three large mainshocks located in the east Indian Ocean with differing depths and fault mechanisms. The spatial coloring represents the number of seconds the strain rate curve is above the 0.1 strain threshold. The strain rate curve is low-pass filtered at 80s. Yellow triangles represent the far-field M≥5.5 seismic events for 20 days following the mainshock. The top figure shows the 08/19/1977 M8.3 normal event and its 17 postshocks. The middle figure is produced using the 03/28/2005 M8.6 Nias reverse mainshock and 13 postshocks. The bottom figure is produced using the 04/11/2012 M8.6 strike-slip event and contains 19 M≥5.5 events during the first 20 days with three postshocks occurring within 24 hours of the mainshock.

2002 M7.9 Denali, Alaska mainshock triggered widespread microseismic activity throughout the western U.S. in regions of low tectonic strain rates indicating that critically stressed faults are present in all tectonic environments (Gomberg, Bodin, et al., 2004). Gonzalez-Huizar and Velasco (2011) and Tape et al. (2013) provide unique observations emphasizing the importance of fault orientation with respect to incident seismic waves that trigger low magnitude earthquakes. Triggered microseismicity is more often observed in extensional or transtensional tectonic environments, with geothermal fields especially responsive to transient deformation, but not all large mainshocks trigger remote microseismic activity (Prejean and Hill, 2009). Parsons, Kaven, et al. (2012) and Hill (2012)] show that the stress perturbations on a fault plane occur only for a short duration and the amplitude is dependent on both fault orientation and depth, often reversing during the wave train. The short-lived occurrence of a positive shear stress perturbation may promote smaller magnitude events but does not appear to trigger larger earthquakes. A fundamental puzzle that still remains when observing low magnitude triggered events is to determine the environmental conditions required for triggered microseismicity to cascade into a M≥5.5 earthquake.

The lack of evidence for immediately triggering M≥5.5 events hints at the significance of the delayed occurrence of large-magnitude triggering, resulting in a global rate increase as well as the challenges associated with classifying triggered candidates. Parsons and Velasco (2011) also do not observe immediate large magnitude triggering using a magnitude threshold of M5.5 and M6.0 using the Advanced National Seismic System catalog. Incomplete centroid catalogs during 0.1- 0.5 days following a mainshock could account for the lack of events (Iwata, 2008), but missing earthquakes are typically located in the near-field. The first potential triggered candidate in this study occurs 8.5 hours following the mainshock (Figure 2.5). Our results show that the two largest rate increases occur within hours of the 2012 M8.6 mainshock and 10-days after the 1977 M8.3 mainshock. The mechanism of delayed dynamic triggering is not well understood and physical models attempting to explain this phenomenon include linear and non-linear friction models, the redistribution of crustal fluids, and asperity weakening via aseismic deformation (Harris, 1998; Hill and Prejean, 2007). Both the non-linear Coulomb failure and fluid redistribution models require elevated pore pressure at seismogenic depths in order to initiate a time dependent failure following transient stress (Brodsky and Prejean, 2005; Parsons, 2005). Some frictional failure models also indicate that a transient stress applied late in the faults seismogenic cycle results in a more significant clock advance toward failure (Gomberg, Beeler, et al., 1998).

One possible weakness in our methodology is the non-uniform times observed for delayed dynamic triggering and the possibility of destructive interference when stacking the time series, thereby not indicating an increase due to the variable time scales that might be involved in delayed triggering. The temporal variation is indicative of a complex nucleation process that may not be represented by a single failure model or initiated uniformly during seismic wave passage. These criteria suggest that only critically stressed faults with elevated pore-pressure conditions are susceptible to a delayed failure subsequent to a transient stress (Hill and Prejean, 2007; Prejean and Hill, 2009). An explanation for the rare observations of M≥5.5 delayed triggering may lie in the occurrence of an ongoing failure process that

is augmented by a transient stress, thereby promoting early failure during a multi-stage nucleation process. This requires that any triggered earthquake be located on a fault that is about to fail in the near future regardless of the external stressing.

2.4.4 Alternative approach

In the present study we have followed the practice usually adopted in triggering studies (Kane et al., 2007; Parsons and Geist, 2014; Parsons and Velasco, 2011), formulating a hypothesis that earthquake triggering is not occurring, then evaluating the significance of actual observations of remote events following a large mainshock. We find that when two particular mainshocks are excluded, we cannot reject the hypothesis that remote triggering does not occur. It is possible to instead formulate a hypothesis that remote earthquake triggering is occurring, and then evaluate the significance that remote events following a particular large mainshock, or composite set of mainshocks, are consistent with the hypothesis. An illustrative hypothesis is that the number of remote postshocks (e.g., occurring globally outside a 1000 km exclusion zone) within six days following a large mainshock is above the average background rate by 10 events, i.e., the excess that actually occurred following the 2012 M8.6 Indian Ocean mainshock (Pollitz, Stein, et al., 2012). In detail, the target excess number of events would be dependent on mainshock magnitude. A probability density function that could be used to test this hypothesis could be obtained by compiling counts of background remote seismicity in random six-day intervals plus 10. It would be possible to perform tests of all post-mainshock seismicity examined in the present study with this approach, and it is worthy of future study.

2.5 Conclusion

We have analyzed 35 years of global M≥7.5 mainshocks to investigate the effect of a transient stress on M≥5.5 seismicity. The systematic far-field triggering of M≥5.5 far-field events is not supported by our results and is not preferential to a faulting mechanism. In contrast to frequently observed triggering of microseismicity and tremor, we do not find any M≥5.5 far-field events triggered during passage of the seismic waves or during the first hours following an event. The 10-day increase in global seismicity following the 2012 M8.6 Indian Ocean earthquake appears to be unique in the global catalog record. Our results do not rule out the possibility of delayed dynamic triggering of some M≥5.5 events in the far field but we are unable to distinguish possible trigger candidates from background seismicity. We infer that only ruptures that have already advanced in their nucleation process are susceptible to triggering by surface waves from great remote earthquakes and that the short duration of encouraging stress transients may allow for triggering of smaller earthquakes and tremor, but not of large and damaging events. Based on our analysis of global seismicity spanning 35 years, we conclude that there is no evidence for significantly increased global earthquake hazard at greater than 2.5 rupture lengths away from great mainshocks.

Chapter 3

Delayed dynamic triggering of three remote M≥6 aftershocks of the 11 April 2012 M8.6 earthquake

Published as: Johnson, C. W., and R. Bürgmann (2015), Delayed dynamic triggering: Local seismicity leading up to three remote M6 aftershocks of the 11 April 2012 M8.6 Indian Ocean earthquake, J. Geophys. Res. Solid Earth, 120, doi:10.1002/2015JB012243.

3.1 Abstract

The 11 April 2012 M8.6 strike-slip Indian Ocean earthquake (IOE) was followed by an increase in global seismic activity, with three remote M≥6.0 earthquakes within 24 hours. We investigate delayed dynamic triggering by systematically examining three offshore regions hosting these events for changes in microseismic activity preceding the IOE, and during the hours between the IOE surface-wave arrival and the triggered-event candidate. The Blanco Fault Zone, USA and the Tiburón Fault Zone, Mexico each host a strike-slip event and the Michoacán Subduction Zone, Mexico hosts a reverse event. At these locations we estimate transient Coulomb stresses of ±1-10 kPa during the IOE. Each study area contains a regional seismic network allowing us to examine continuous waveforms at one or more nearby stations. We implement a short- /long-term-average algorithm and template matching to detect events and assess the seismicity with the β-statistic. Our results indicate low-magnitude seismicity in the days prior to the IOE and the occurrence of earthquakes during the surface-wave passage after more than 2-hours of transient loading. We find both transtensional tectonic environments respond to the transient stresses with a substantial increase observed in the seismicity rates during the hours after the surface waves passage. In contrast, seismicity rates remain constant in the subduction zone we investigate during the 14-hour delay between the IOE and the large-magnitude earthquake. The seismicity rate increases we observe occur after many hours of dynamic stresses and suggest the long duration of transient loading

initiated failure processes leading up to these M≥6.0 events.

3.2 Introduction

Seismic waves from large earthquakes are capable of transferring energy to remote distances, i.e. many fault lengths from the source, which is a well documented phenomenon and can potentially increase seismic activity in far-field regions (Freed, 2005; Gomberg, 2001; Gomberg, Bodin, et al., 2004; Gonzalez-Huizar, Velasco, et al., 2012; Hill and Prejean, 2015; Hill, Reasenberg, et al., 1993; Pollitz, Stein, et al., 2012; Prejean and Hill, 2009; Velasco et al., 2008; West et al., 2005). The 11 April 2012 M8.6 Indian Ocean earthquake (IOE; 08:38:36 UTC; 93.06°, 2.32°, 40 km) is the largest strike-slip earthquake observed in the modern era that ruptured a series of intraplate conjugate faults and was followed by a M8.2 strike-slip aftershock two hours after the initial rupture (McGuire and Beroza, 2012). The IOE is interesting with regards to earthquake communication because of the number of large magnitude (M≥5.5) events that occurred in the ensuing days. Pollitz, Stein, et al. (2012) quantify the significance of the 6-day increase in remote M≥5.5 earthquakes following the IOE and Johnson, Bürgmann, et al. (2015) document the rare occurrence of M≥5.5 events triggered by global remote M≥7.5 mainshocks, indicating the uniqueness of the large magnitude remote aftershocks of the IOE. Interestingly, M>5 triggering candidates appear to only occur after a delay period on the order of hours to weeks following the stress perturbation (Gomberg, 2013; Gomberg and Bodin, 1994; Gonzalez-Huizar, Velasco, et al., 2012; Parsons and Geist, 2014; Pollitz, Stein, et al., 2012) and physical evidence to connect these M>5 events to a transient stress via a seismic or aseismic process is lacking. The delay period coupled with a limited number of observations of M>5 triggered events (Parsons and Geist, 2014) seems to contradict the ubiquity of M<5 triggered earthquakes (Hill and Prejean, 2015; Velasco et al., 2008) and the physical process of delayed dynamic triggering still requires a full explanation (Parsons, Kaven, et al., 2012).

Establishing a tenable connection between small transient stresses and a seismic event becomes progressively more difficult as the delay time increases. Non-systematic delay times of larger-magnitude earthquakes following transient stresses alludes to the scenario that multiple failure conditions coincide, e.g. partial damaging of frictional contacts (Parsons, 2005) and changes in pore pressure (Brodsky, 2003), in order to advance the seismic cycle of M>5 earthquakes to the point of failure. Case studies quantifying seismicity rate changes find that transient stresses on the order of 1-10 kPa are capable of triggering low magnitude (M<4) earthquakes at remote distances (Aiken and Peng, 2014; Brodsky and Prejean, 2005; Pankow et al., 2004; Peng, Wu, et al., 2011; Peng, Hill, et al., 2010; Prejean, Hill, et al., 2004; Tape et al., 2013; van der Elst and Brodsky, 2010; West et al., 2005). Observable changes in seismic activity can be used to infer the state of stress on a fault to further explore earthquake nucleation and help explain the processes initiated during the passage of seismic waves that may be responsible for delayed triggering of subsequent earthquakes (Brodsky and van der Elst, 2014; Harris, 1998; Hill and Prejean, 2015).

The passage of seismic waves can promote two different changes in seismic activity, the first being an immediate increase in earthquakes during the cyclic loading on a fault. This is most easily explained using a Coulomb failure model that assumes the transient stresses exceed a failure threshold on an already critically stressed fault (Hill, 2012). The second is a delayed increase in seismic activity that initiates in the subsequent hours to days of a transient stress (Freed, 2005; Gomberg, Beeler, et al., 1998; Hill and Prejean, 2015; Parsons, 2005). Proposed models to explain delayed dynamic triggering include nonlinear friction, fluid migration, and/or aseismic deformation (Hill and Prejean, 2015). For a rupture to occur in either dynamic triggering scenario, a transient load on a preexisting fault late in the seismic cycle is required to advance the fault toward failure (Gomberg, Beeler, et al., 1998; Gomberg, Bodin, et al., 2004; Harris, 1998).

In this study we investigate the delayed dynamic triggering of three M≥6.0 earthquakes located along the North America plate boundary within one day of the 2012 M8.6 IOE. The global aftershock sequence described by Pollitz, Stein, et al. (2012) contains 16 M≥5.5 earthquakes in the subsequent 6-days, with three M≥6.7 mainshocks in that set of events. We limit our study to the first 24-hours following the IOE and carefully analyze the seismicity leading up to three large earthquakes, which includes two M≥6.7 earthquakes. Our focus is on resolving changes in near-field seismic activity with respect to the transient loading on the faults, specifically in the time period between the passage of seismic waves and these large-event occurrences. The location and orientation of the IOE produced a region of elevated strain along the active plate boundary margins of the Pacific Plate to antipodal distances and encompasses the three events of interest (Figure 3.1). The rate curve in Figure 3.1 indicates a multiday increase in global M≥3 events (see details of analysis described in Data Analysis and Methods Section) and motivates the search for a possible increase of low magnitude events within the vicinity of the three large magnitude trigger candidates. The three M≥6.0 trigger candidates are each located offshore in rapidly deforming plate boundary zones, two transform faults and one subduction zone, that regularly host large magnitude (M>5) earthquakes. The delayed response following the IOE surface waves may indicate that the catalog records are incomplete or an aseismic process is occurring prior to the rupture. For each of the three remote events we systematically investigate changes in microseismic activity preceding the IOE and during the hours between the surface waves arrival and the triggered event candidate using both catalog and waveform data obtained from each region. The methods applied to each region are described in Data Analysis and Methods and the data obtained and the associated results are presented in Study area, data, and results for each event of interest.

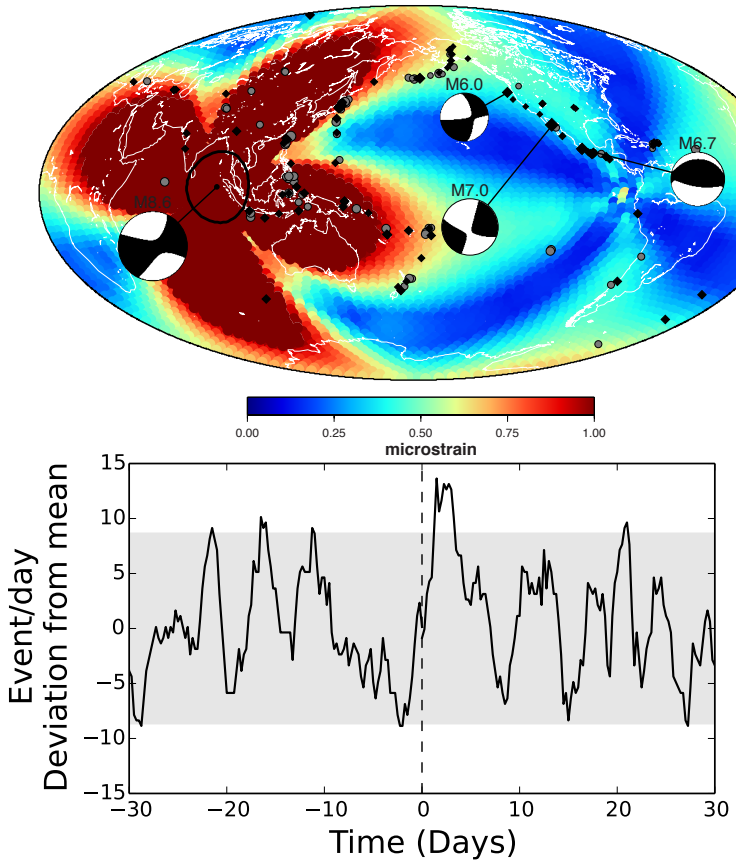

Figure 3.1: (Top) Dynamic strain field for the 11 April 2012 M8.6 IOE calculated from synthetic waveforms. The color represents the peak shear magnitude estimated from the second invariant of the deviatoric strain tensor and, as shown, is saturated at 1.0 μstrain (corresponding to ∼30 kPa). Moment tensors (`http://earthquake.usgs.gov`) are shown for the M8.6 IOE and the three remote M>6.0 mainshocks that occurred within 24-hours of the transient stress produced by the IOE surface waves. The remote events are located along actively deforming plate boundaries within the elevated strain region. The gray circles and black diamonds show the locations of the M≥3 declustered seismicity in the 3-days before and after the IOE, respectively. (Bottom) The M≥3 seismicity rate curve from 30 days before to 30 days after the IOE, with two-sigma confidence interval shown in gray for all events located within the elevated strain region (≥0.1 μstrain) with an exclusion zone of 1600 km around the IOE (black circle).

3.3 Data Analysis Methods

3.3.1 Seismicity Catalogs

Catalog data was analyzed for the presence of earthquake activity prior to the M≥6 mainshocks. The two sources of catalog events used are the Advanced National Seismic System (ANSS) and the Servicio Sismologico Nacional de Mexico (SSN), which contains lower-magnitude events not reported to ANSS for earthquakes in Mexico. Specifically, we are looking for local activity in the regions of interest preceding the IOE surface waves in order to document ongoing seismic sequences in each study area and any catalog events during the delay period before the M≥6 mainshocks. We also use all cataloged foreshocks and aftershocks located in the fault zones of interest are used as templates in the waveform template matching analysis.

3.3.2 Broadband Waveforms

The waveform data is analyzed for seismic activity during the days to weeks prior to the IOE. The temporal coverage is dependent on network availability in each region and is described in Study area, data, and results. Due to the offshore location of the three earthquakes of interest and the density of the seismic network coverage, we are limited to a single seismometer for each of the potential triggered mainshock locations for the waveform analysis (van der Elst, Savage, et al., 2013). The range of distances to the nearest seismometer is between 50-100 km and we use the vertical channel for the analysis.

The waveform data is inspected for evidence of immediate triggering during the passage of the surface waves. We apply a 7 Hz high-pass filter in order to remove teleseismic events and highlight local seismic activity. We calculate the spectrogram for the time series using a 5 s Hanning window (Peng, Long, et al., 2011) and look for bursts of high-frequency energy superimposed on the long-period signal. In conjunction with the spectral analysis, we generate audio files using the waveform data (Kilb, Peng, et al., 2012) and listen for earthquakes during the IOE passage and the hours between the local mainshock. Following Kilb, Peng, et al. (2012), the audio is combined with the spectral analysis to produce animated time-series for 11 April 2012 to find events during the surface wave passage. In addition, we calculate the cumulative energy density (Brodsky and Prejean, 2005) during the IOE for multiple bandwidths using,

$$E = \rho c \int v^2 dt \tag{3.1}$$

where, ρ is the bulk rock density of 3000 kg m^{-3}, c is the phase velocity of 4500 m s^{-1}, and v is the particle velocity obtained from the waveform data. To quantify the visual and audio analysis, we perform a single-station event detection analysis using a recursive short-term-average / long-term-average (STA/LTA) algorithm (Ketner and Power, 2013; Withers et al., 1998). The STA/LTA method is widely used in seismological applications and requires

Event	Blanco fracture zone	Michoacán sub zone	Tiburón fault zone
M_W	M6.0	M6.7	M7.0
Date	04/11/2012	04/11/2012	04/12/2012
Time (UTC)	22:41:46	22:55:10	07:15:48
Location	-127.64°, 43.58°, 8km	-102.7°, 18.23°, 20km	-113.10°, 28.7°, 13km
Strike, Dip, Rake	288°, 81°, 168°	116°, 68°, 95°	311°, 89°, 179°
IOE Distance	13,558 km	17,216 km	15,644 km
Coulomb stress	-4.2 - 5.4 kPa	-3.7 - 3.7 kPa	-11.5 - 10.0 kPa
Delay time	14.08 h	14.28 h	22.62 h
STA/LTA Corner	5 Hz	4 Hz	4 Hz
STA/LTA Window	0.1/5.0 s	0.05/5.0 s	0.005/5.0 s
STA/LTA On/Off	20/12	22/12	22/12

Table 3.1: IOE global aftershocks within 24-hours.

tuning of the parameters for regional or global event detection and station noise levels. We start by applying a high-pass filter and use STA/LTA parameters applied to earthquake early warning systems (Wurman et al., 2007), then adjust for the different noise conditions at each station (Table 3.1). Our usage of the algorithm is limited to the temporal identification of a local event with no information determined for the location. For this analysis the algorithm was performed on continuous waveform velocity records for the five days before the IOE and we are able to establish a short-term record of activity that is used to calculate a change in seismicity rates following the IOE. To verify the performance of the algorithm we visually inspect the waveforms of the automated picking process and adjust the parameters based on the inclusion of false event detections.

To further look for unreported seismic events we employ a match template technique using longer time periods of waveforms, where available, and use aftershocks from each trigger candidate as templates to identify unreported seismic events (Kato et al., 2013; Meng and Peng, 2014; Peng, Vidale, et al., 2009; Shelly, Beroza, et al., 2007; van der Elst, Savage, et al., 2013). To remove background noise and enhance any local earthquake signal the seismic records are band-pass filtered using a two-pass, four-pole, Butterworth filter with corners of 7-15 Hz. The choice of frequency range is subjective so we test additional frequency ranges of 2-8 Hz and 4-14 Hz and found the higher frequency range produced better results with less false positive detections considering the long distances between the source locations and the seismometer (van der Elst, Savage, et al., 2013). Templates are manually selected using the vertical channel of the filtered records by visually searching through the waveform data for earthquakes. All cataloged aftershocks, and the associated secondary aftershocks, are utilized as templates. The template time window is different in the three fault zones due to the travel time required to the nearest seismic station. Regardless of template duration, each starts one second before the P-wave and ends two seconds after the S-wave arrival. The same filter parameters are applied to the continuous records and the

templates are iterated through the time series to calculate the cross-correlation value at each time step. The median average deviation (MAD) is calculated from the cross-correlation results to determine a positive match threshold. Due to large distances from source to receiver we define a detection threshold of 18 times the MAD of the cross-correlation results to select local seismic activity assumed to be associated with the template. Using a lower multiplier value for the MAD threshold results in an unmanageable number of false positive detections due to correlation with noise. Other studies have implemented MAD multiplier values between 8-15 in order to successfully match microseismicity in the waveforms (Kato et al., 2013; Meng and Peng, 2014; Shelly, Beroza, et al., 2007). Due to the network distance constraints we am able to identify the occurrence of microseismic events with a single station but no information for the magnitude or location is determined when applying this method (van der Elst, Savage, et al., 2013; Velasco et al., 2008).

3.3.3 Seismicity Rates

We use the STA/LTA results to calculate a change in seismicity rates using the β-statistic (Mathews and Reasenberg, 1988) and is calculated as

$$\beta = \frac{N_a - E(N_a)}{var(N_a)} = \frac{N_a - N_b \frac{t_a}{t_b}}{\sqrt{N_b \frac{t_a}{t_b}(1 - \frac{t_a}{t_b})}} \tag{3.2}$$

where, N_a and N_b are the number of events and t_a and t_a are the time intervals before and after the passage of the IOE surface waves, respectively. The number of events and the time periods are used to calculate the expected number of events and the variance of the number of events afterwards. Following a uniform distribution of events, if no events occur during the time interval t_a, then the expected number of events, $E(N_a)$, is set to 0.25. Usage of the β-statistic requires the assumption that the seismicity is a stationary Poisson process and the value represents the number of standard deviations the rate increases or decreases during the time after. We acknowledge the fact that we are not preconditioning the seismicity data through a declustering procedure to ensure a stationary Poisson process as required for the correct usage of the β-statistic, but are limited to the temporal occurrence of events without any information about the magnitude or location. Additionally, we would like to comment on the fact that the choice of starting time will strongly influence the β-statistic calculation and can bias the value if a period of abnormal activity, either high or low, occurs within t_a. Due to data availability limitations, we choose to use a short time period of only 5 days of events selected by the STA/LTA algorithm to test the three regions equally for a seismicity rate change and do not rely solely on the β-statistic values to assess changes in seismic activity. The choice of using the STA/LTA results instead of the template matching results does not change the rate change results.

We also calculate the daily seismicity rate for M≥3 remote events in the ANSS catalog within ±30 days of the IOE for the spatial region above 0.1 μstrain during the surface wave passage (Figure 3.1) following Johnson, Bürgmann, et al. (2015). The rate curve is

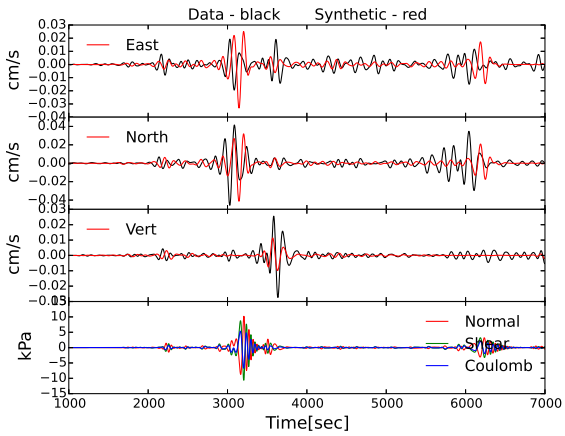

Figure 3.2: Synthetic waveform comparison and stress curves for station J06A. Shown are the east, north, and vertical components with the corresponding stresses resolved on the plane with strike = 288°, dip = 81°, and rake = 168°.

produced using a ∼1600 km exclusion zone around the IOE epicenter to remove local aftershocks. The remote M≥3.0 events are limited to depths less than 50km and the seismicity is declustered using the Reasenberg algorithm (Reasenberg, 1985) with default parameters. The declustering we perform is a first-order approach to remove aftershocks from the rate curve, especially during the days following the IOE when a known global increase in activity occurs. For purposes of this study, a more rigorous declustering effort is not warranted due to catalog completeness differences at the global scale. The rate curve in Figure 3.1 represents a deviation from the background rate calculated only for the events occurring within the temporal and spatial constraints and is averaged using a 3-day moving window.

3.3.4 Stress Modeling

The dynamic stresses are calculated in each fault zone using the direct Greens function method to model displacement waveforms and the associated strain (Friederich and Dalkolmo, 1995; Pollitz, 1996). The long-period synthetic waveforms are validated using the local seismic records (Figures 3.2, 3.3, 3.4). The stress tensor time series is calculated from the six-component strain tensor time series for an isotropic elastic solid. We assume a Poisson ratio of 0.25 and a shear modulus of 30 GPa, standard values for the seismogenic crust. The stress tensor is rotated to the fault plane, which we assume to have an orientation equal to the strike, dip, and rake of the moment tensor solution and the geometry of the respective plate-boundary fault (`http://earthquake.usgs.gov`). We estimate the transient Coulomb stress using a friction coefficient of 0.4 with the normal and shear components of stress on the fault plane.

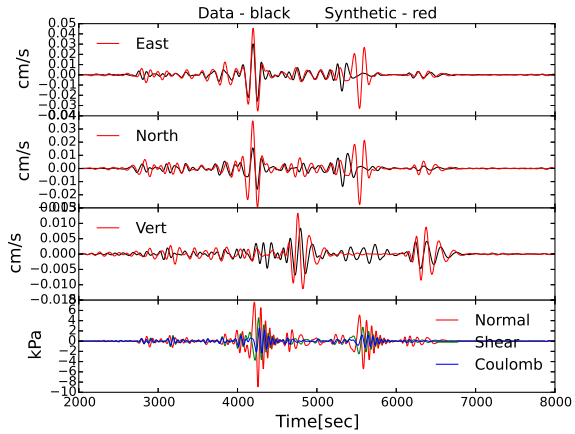

Figure 3.3: Synthetic waveform comparison and stress curves for station MMIG. Shown are the east, north, and vertical components with the corresponding stresses resolved on the plane with strike = 116°, dip = 68°, and rake = 95°.

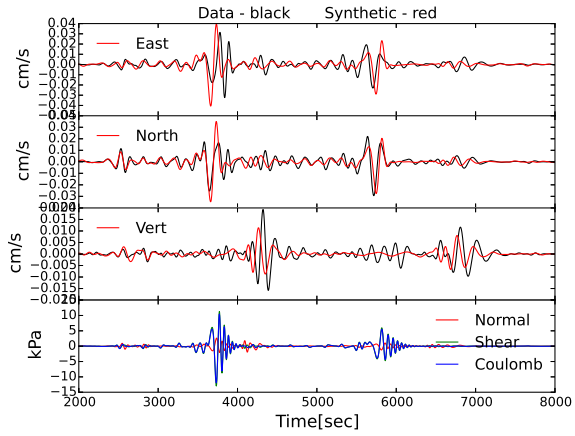

Figure 3.4: Synthetic waveform comparison and stress curves for station BAHB. Shown are the east, north, and vertical components with the corresponding stresses resolved on the plane with strike = 311°, dip = 89°, and rake = 179°.

3.4 Study area, data, and results

The three regions of proposed triggered activity shown in Figure 3.1 are described in chronological order with respect to their time of occurrence following the IOE. Each subsection contains a brief geologic description of the area, the data obtained, and an additional subsection describing the results. Pertinent information for each mainshock is summarized in Table 3.1.

3.4.1 Blanco Fault Zone, Offshore Oregon, USA

The Blanco Fault Zone (BFZ) is a transform fault system between the Juan de Fuca plate and the Pacific Plate that links the Juan de Fuca and Gorda spreading ridges located offshore from Oregon, USA (Figure 3.5). The eastern termination of the BFZ is ∼150 km offshore from the Oregon coast and extends ∼400 km WNW before intersecting the Juan de Fuca spreading ridge. The fault zone is a series of right stepping right-lateral transform faults with a long-term slip rate of ∼5.6 cm/yr (Dziak et al., 2000; Wilson, 1993). The trigger event candidate in the BFZ we study is the 11 April 2012 (DOY 102) M6.0 that ruptured ∼14 hours after the IOE. Within fifty-six days prior to the BFZ M6.0, two cataloged events occurred in the fault zone within 10 km of the hypocenter (Figure 3.5). The first is a M5.8 on 15 February 2012 (DOY 046) and a M4.4 occurred on 28 March 2012 (DOY 088), possibly an aftershock of the M5.8. The broadband waveform data near the BFZ was recorded by the temporary deployment of ocean bottom seismometers for the Cascadia Initiative project (Toomey et al., 2014). We obtained records for the period of 1 February 2012 to 15 April 2012. The distance to the nearest seismic station J06A is ∼100 km from the BFZ M6.0 reported location (-127.64°, 43.58°; Figure 3.5). The next closest station is 170 km from the M6.0. During the IOE surface wave passage we estimate transient Coulomb stress levels from -4.2 - 5.4 kPa (Figure 3.2). For the analysis, we perform the template matching on waveforms from DOY046-106 and the STA/LTA event picking is performed on the waveforms from DOY097-102.

Blanco Fault Zone Results

The spectral and audio results suggest local events occurring during the passage of the IOE surface waves, with the first notable event occurring at ∼11:15UTC more than 2 hours after the first teleseismic wave arrival (Figure 3.6 and Figure 3.7). The filtered time series and spectrogram shown in Figure 3.6 indicate three low magnitude events during the IOE. The audio of the waveforms confirms these events during the IOE surface waves and indicates earthquakes beginning within the first hour of DOY102. The audio in also contains a high-pitch noise that starts after the IOE surface waves and Figure 3.6 shows an increase in energy at 15-18Hz. We further investigate this high-frequency signal by preparing additional audio files and spectrograms, and find it is also present in the daily records from DOY099-DOY101 at the same frequency range as a discontinuous signal lasting for many hours. We

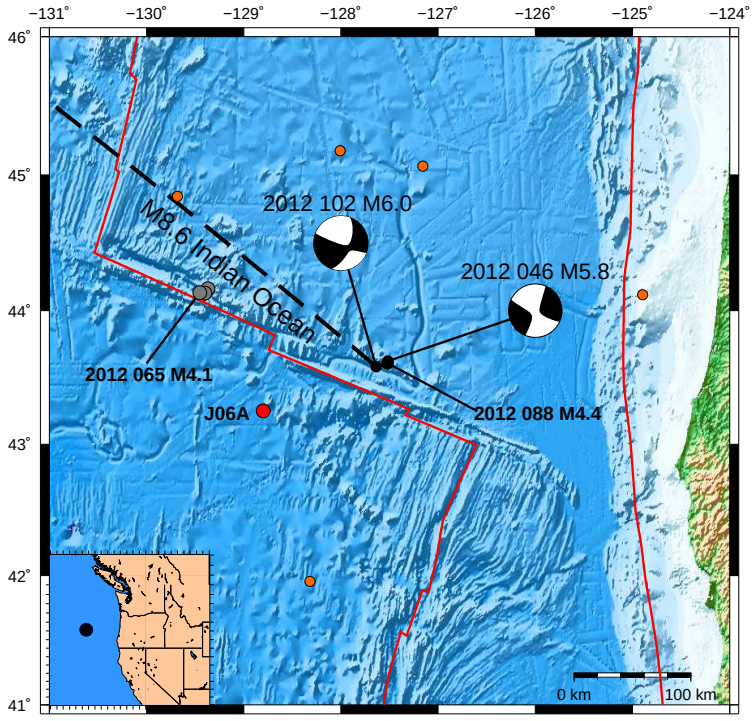

Figure 3.5: Blanco Fault Zone located offshore Oregon, USA comprised of right-lateral right-stepping transform faults. The dashed black line indicates the back azimuth orientation of the 2012 M8.6 IOE. The red circle is the location of station J06A used in the analysis and is ∼100 km from the M6.0. The orange circles are the locations of additional ocean bottom seismometers in the network. Moment tensors (`http://earthquake.usgs.gov`) are shown for the M5.8 and M6.0 occurring on 02/15/2012 (DOY 046) and 04/11/2012 (DOY 102), respectively. A M4.4 event occurs 14 days before the M6.0 and three M4.1 - M4.3 events occur in the northwest section of the fracture zone 47 days before (DOY 065).

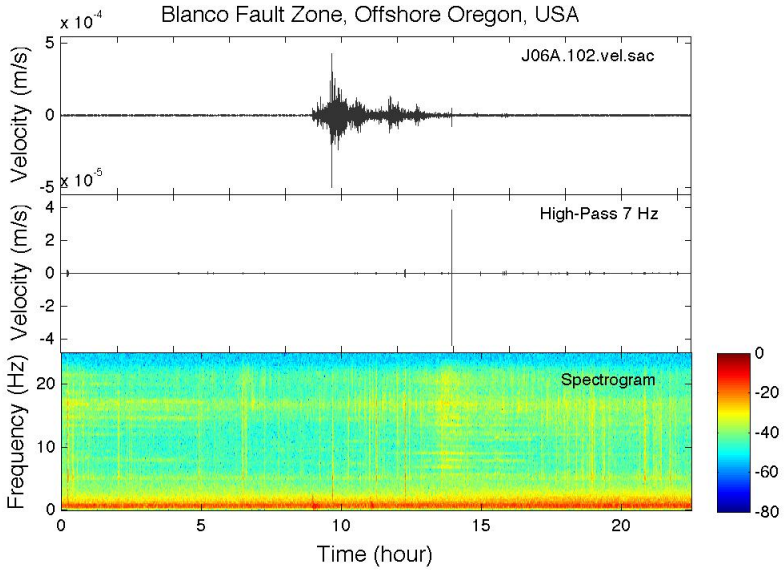

Figure 3.6: (Top) Vertical waveforms of the day of the IOE M8.6 and M8.2 aftershock on 11 April 2012 (DOY 102) from 08:20-13:50 UTC at station J06A located ∼100 km from the BFZ M6.0. Top panel is the original velocity data showing the long-period teleseismic waves. Middle panel is high-pass filtered at 7Hz to show the near-field earthquakes. Bottom panel is the spectrogram. High-frequency energy shown in the spectrogram indicates near-field events. We find three events that occur ∼2-hours after the initiation of dynamic shaking (∼11.3, ∼12.3, and ∼13.6) as well as other events occurring throughout the day.

quantify the spectrogram and audio results using the seismicity rates obtained from the STA/LTA algorithm and find an increase in activity beginning on 10 April 2012 (DOY101) that continues to increase during the IOE surface wave passage with the occurrence of 20 events (Figure 3.8). The cumulative energy density in Figure 3.9 indicates an increase in high-frequency energy at DOY102.6, which corresponds to the pulse of activity shown in Figure 3.8 during the delay period. The β-statistic values in Figure 3.8 are indicative of a positive rate change with values above 2, but we hesitate to state that the subtle change in activity above background levels following the IOE is representative of a rate increase with the very short temporal record used to determine that value.

The ANSS catalog records contain only one aftershock following the M5.8 (DOY046) to use as a known event template. All other templates are selected due to the temporal relation with the known earthquakes in order to limit ourselves to the apparent short-term aftershocks of the cataloged events. Hence, we avoid scanning the entire set of waveforms and selecting every observable event since we lack any location constraint and are working in a seismically active fault zone. We restrict the template selection period to 48-hours following the event to reduce the number of non-associated microseismic events. We manually scan the

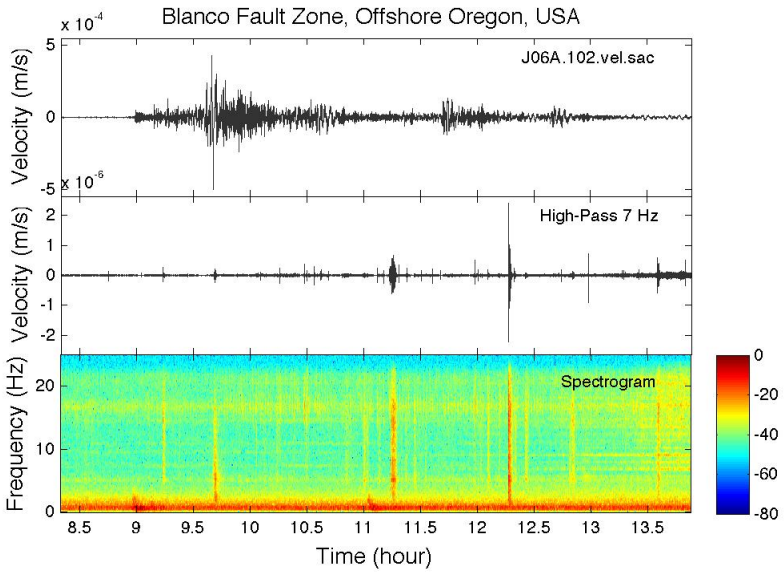

Figure 3.7: Spectrogram for station J06A during IOE surface waves.

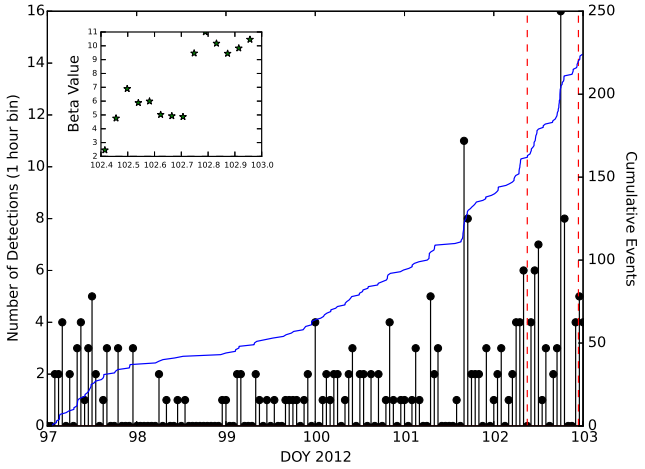

Figure 3.8: STA/LTA results for the BFZ from 6-12 April 2012 (DOY 97-103). Blue curve is the cumulative number of events. Black stems are number of events per 1-hour bin. The two dashed red lines represent the time period between the IOE surface waves and BFZ earthquakes. The figure insert is the β value calculated for the time period between the dashed red lines. For the β-statistic value the time period before (tb) is from 97 to the first red dashed line.

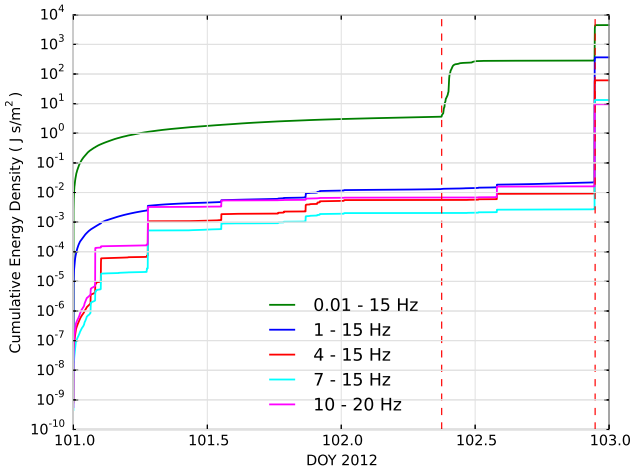

Figure 3.9: The cumulative energy density is shown for the BFZ using five different bandwidths. Dashed red lines indicate the IEO and local event times. The green line is the greatest and represents the long period energy from the surface wave arrival. The high frequency energy increases at DOY102.6 and supports the increase of activity at the same time that is shown in Figure 3.8.

waveforms following the M5.8, M4.4, and M6.0 and generate 41, 4, and 38 templates from their aftershocks, respectively, using a 13 second duration. The match template correlation coefficient results from the 83 templates are shown in Figure 3.10. The results are used to produce cumulative and rate curves, which capture the decaying aftershock sequence of the DOY 046 M5.8 and DOY 102 M6.0 mainshocks (Figure 3.11). The largest increase in the hourly rate of events in Figure 3.11 does not occur until the BFZ M6.0, but the rate does indicate a similar increase at DOY102.5 that we observe in the STA/LTA results (Figure 3.8).

3.4.2 Michoacán, Middle America Trench, Mexico

The Michoacán subduction zone segment (MSZ) is located between the subducting Cocos plate and the North American plate in southern Mexico. The MSZ is north of Guerrero, Mexico with a local convergence rate of 5.4 cm/yr (DeMets et al., 2010). Here the slab is shallowly descending to a depth of 40 km and transitions to a subhorizontal orientation for >100km before steeply subducting into the mantle (Perez-Campos et al., 2008). Near this section of the subduction zone, non-volcanic tremor and slow slip events are shown to respond to teleseismic surface waves and possibly promote a stress redistribution via aseismic creep (Zigone et al., 2012). The event of interest in the MSZ study area is the 11 April 2012 M6.7 (DOY 102) that ruptured ∼14 hours after the M8.6 IOE surface wave arrival and 15 minutes after the M6.0 BFZ event (-102.70°, 18.23°; Figure 3.12). We obtained seismicity

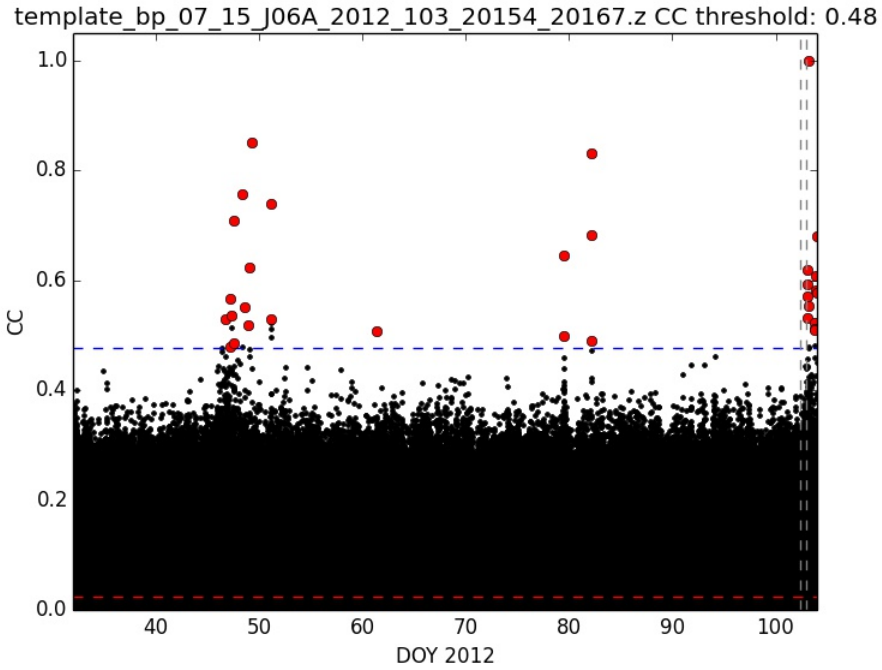

Figure 3.10: (Top) Black stems represent detected events per hour from template matching results using 83 template events from the aftershocks of the15 February 2012 M5.8 (DOY046), the 28 March 2012 M4.1 (DOY088), and the 11 April 2012 M6.0 (DOY 102) mainshocks in the BFZ. Overprinted is the cumulative event curve (blue), which indicates the decay of the aftershock sequence following the 15 February 2012 (DOY 046) M5.8 earthquake. The bottom panel is a close up of the seismicity rate from 6-12 April 2012. The red dashed lines represent the time of the M8.6 IOE and the M6.0 TFZ earthquake. The increase observed during the delay period initiates >2 hours after the IOE surface wave arrival.

catalog records from the SSN catalog which shows a M4.8 and an associated M3.6 aftershock are cataloged in the MSZ on 3 April 2012 (DOY 094), 8 days before and ∼100 km from the M6.7 mainshock. Additional seismicity in the MSZ include a sequence on 8-9 March 2012 of M3.3-M3.8 earthquakes that rupture ∼35 km from the mainshock and continue propagating ∼20 km NW along strike.

The Universidad Nacional Autonoma de Mexico (UNAM) operates a continuously recording seismic network with stations along the coast near the MSZ (Figure 3.12). We obtained waveform records from 1-15 April 2012 for four stations in the vicinity. The station MMIG is the closest to the M6.7 mainshock and located at a distance of ∼100 from the epicenter. The next closest station is >200 km from the mainshock and both the proximity to the shoreline and distance to the mainshock do not create favorable conditions for observing microseismic events. We estimate transient Coulomb stress as high as ±3.7 kPa during the IOE surface

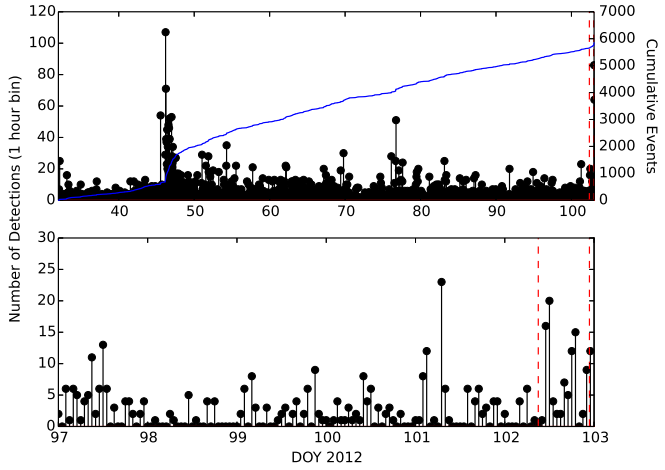

Figure 3.11: J06A template cross-correlation example. Black dots are cc values and red circle are event picks above CC threshold shown in figure title. Black dots above the blue dashed line are events above threshold and not counted twice. Template matched events from the M5.8 on DOY046.

wave passage (Figure 3.3).

Michoacán Results

The high-pass filter, spectrogram, and audio results indicate the occurrence of one event during the surface wave train at hour 11.6 (Figure 3.13 and Figure 3.14). We do observe high-frequency pulses in the high-pass filter data but upon inspection these do not appear to be local earthquakes and are very low-amplitude emergent signals in the data. The spectrogram in Figure 3.13 does indicate high-frequency energy, but the audio files during this time period does not contain the impulse-like sound that is found for other earthquakes. The STA/LTA produced rate curves (Figure 3.15) and the cumulative energy (Figure 3.16) agree that no increase in high-frequency activity is present during the delay period before the MSZ M6.7 event. The β-statistic values for this time period are negative, indicating a reduction in observed events from background levels and can also be seen in the cumulative number of events (Figure 3.15).

Templates are generated using the 19 M6.7 aftershocks within 25 km of the hypocenter listed in the SSN catalog and additional events observed in the MMIG waveforms within 2 days of the mainshock. In total, 34 templates with an 11 second duration are used for the analysis. Template results (Figure 3.17) do not indicate a change in seismic activity before the IOE or during the delay period (Figure 3.18). The results do indicate ongoing microseismic events but the rates remains constant prior to the M6.7 MSZ mainshock.

Interestingly, the arrival time of the M6.0 BFZ seismic waves coincides with the M6.7

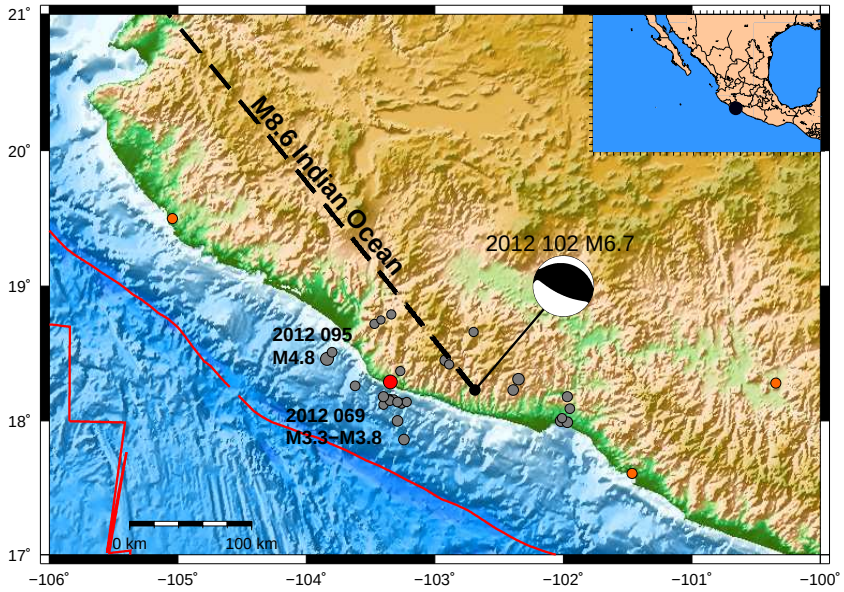

Figure 3.12: The Michoacán subduction zone earthquake is located in southern Mexico along the Middle America Trench. The 11 April 2012 (DOY 102) M6.7 moment tensor (`earthquake.usgs.gov`) is shown with the black dashed line indicating the back azimuth to the IOE. Red circle is station MMIG, located ∼100 km from the M6.7 and used to perform the analysis and the orange circles are other seismic stations in the region operated by UNAM. Gray circles are the seismicity occurring between 1 March 2012 - 10 April 2012. The locations for the 03 April 2012 (DOY 094) M4.8 and the 09 March 2012 (DOY 069) M3.8 sequence are labeled. The red lines represent the plate boundary.

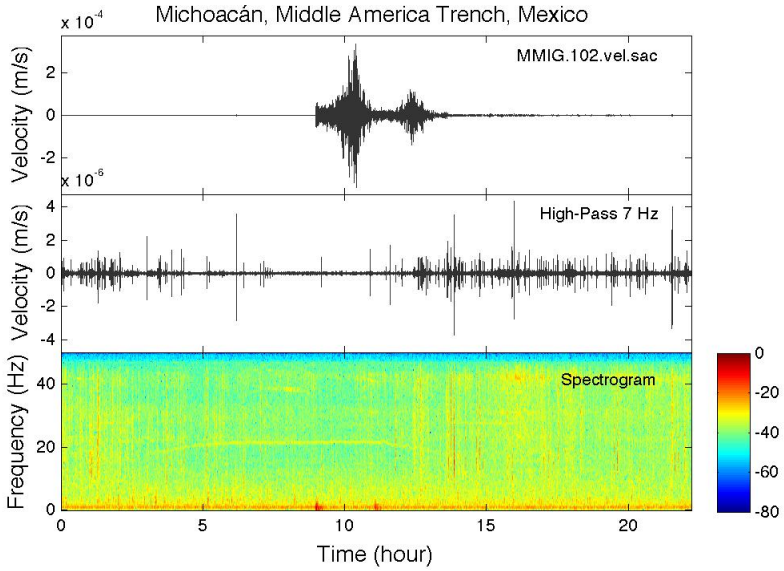

Figure 3.13: (Top) Seismic record for the day of the IOE surface waves for the vertical channel of station MMIG located 100 km from the M6.7 in the MSZ. The top panel is the original velocity data, the middle panel is the high-pass filter data, and the bottom panel is the spectrogram. The high-pass data shows high frequency signals after 12:30UTC that show an increase in energy in the spectrogram and is consistent with high frequency energy earlier in the day. Analysis of the audio files does not suggest that these are local earthquakes and this signal is observed consistently through the high-pass filter data in the hours and days before the IOE.

MSZ rupture. The ak135 travel-time-tables (Kennett et al., 1995) indicate the P-wave and S-wave arrive 410 seconds and 90 seconds before the M6.7, respectively. Visual inspection of the MMIG station records do not clearly show the P- and S-wave arrivals due to the signal to noise ratio obscuring the expected body waves. Using a distance of 3650 km and velocity of 4.25 km/s we estimate the Love wave arrival to be ∼60 seconds after the M6.7 MSZ mainshock. We model the BFZ waveforms and strain field for the MSZ and calculate a transient stress change between ±0.022 kPa, significantly less than the stresses associated with the IOE and we do not consider this a likely factor in the failure process.

3.4.3 Tiburón Fault Zone, Gulf of California, Mexico

Beneath the Gulf of California lies the North America Pacific plate boundary that separates mainland Mexico and Baja California, Mexico. The plate boundary is a transtensional shear zone that contains a series of right stepping right-lateral transform faults and spreading centers. GPS derived displacement rates indicate ∼4.7 cm/yr of lateral motion between

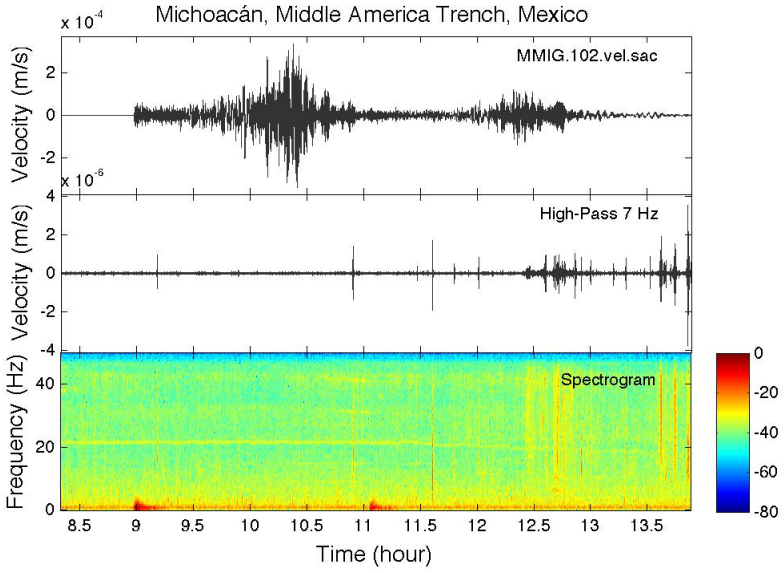

Figure 3.14: Spectrogram for station MMIG during IOE surface waves.

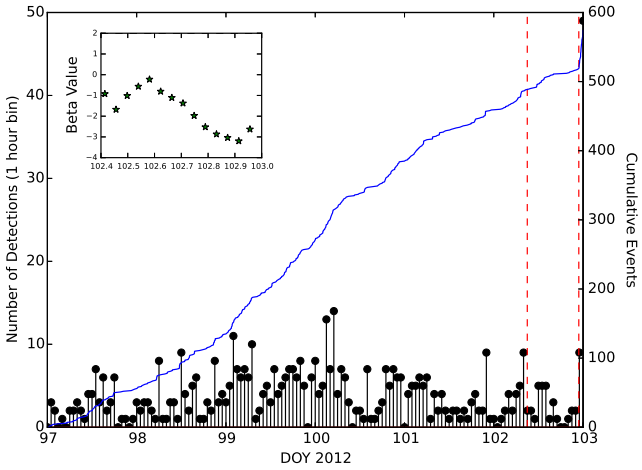

Figure 3.15: STA/LTA results for station MMIG in the MSZ from 6-11 April 2012 (DOY 97-103). Blue curve is cumulative events and the black stems are events per hour. Dashed red lines indicate the delay period between the IOE surface wave arrival and the MSZ M6.7 earthquake. The figure insert showing the β-statistic values does not indicate an increase during the delay period.

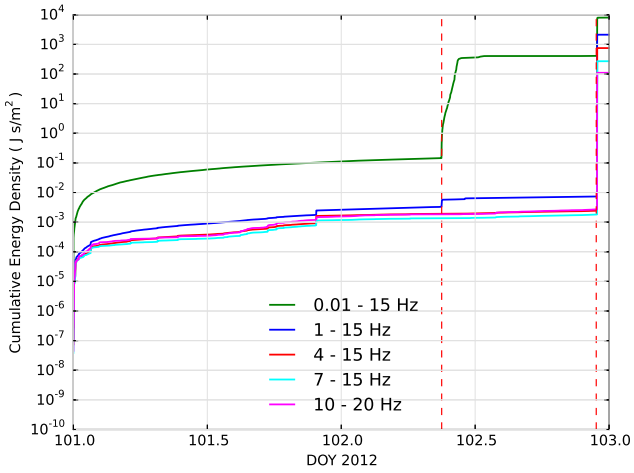

Figure 3.16: The cumulative energy recorded at station MMIG is shown for multiple bandwidths. The dashed red lines indicate the delay period between the IOE and MSZ earthquakes. No increase in high frequency energy is observed during the delay period.

North America and Baja California, Mexico (Plattner et al., 2007). The Tiburón fault zone (TFZ) is located in the central section of the shear zone and contains en echelon right-lateral transform structures (Figure 3.19). The event of interest is the 12 April 2012 (DOY 103) M7.0 mainshock that ruptured ∼22 hours after the IOE surface waves. The mainshock is preceded by 4 cataloged foreshocks 2 hours before, with the largest being a M6.0 that occurred 9 minutes before the M7.0 mainshock. Aside from the foreshocks, seismicity records from the SSN catalog do not indicate an ongoing sequence in the days or months prior to the M7.0 mainshock. The SSN catalog shows no earthquakes occurring within 100 km of the mainshock for more than 100 days. We estimate a transient Coulomb stress on the TFZ of up to ±10.0 kPa during the IOE surface waves on a fault plane nearly parallel with the back azimuth orientation to the IOE (Figure 3.4). This favorable fault orientation results in the maximum possible Coulomb stress change during a Love wave passage (Hill, 2012), the dominant wave from the IOE.

The TFZ waveform data from 5-15 April 2012 was obtained from the Red Seismologica de Banda Ancha del Gulfo de California (RESBAN) network operated by Centro de Investigacion Cientica y de Educacion Superior de Ensenada (CICESE). The closest station to the TFZ is BAHB, which is located ∼50 km from the M7.0 reported location (-113.10°, 28.70°) and recording at 100 Hz (Figure 3.19). Additional regional seismic stations are located at distances >125 km from the M7.0 mainshock and are recording at 20 Hz. The combination of distance and sample rate is not optimal for detecting low magnitude earthquakes at multiple stations.

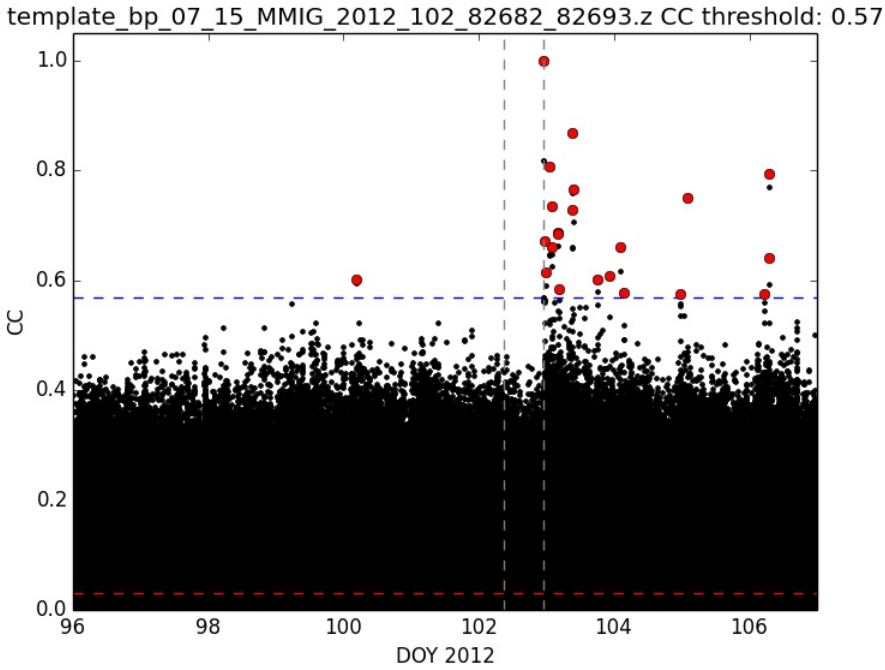

Figure 3.17: MMIG template cross-correlation example. Black dots are cc values and red circle are event picks above CC threshold shown in figure title. Black dots above the blue dashed line are events above threshold and not counted twice. Templates match mostly aftershocks.

Tiburón Fault Zone Results

The TFZ audio results indicate one event during the passage of the M8.2 IOE aftershock surface waves at ∼11.5 hours as a soft knocking sound following more than two hours of long-period shaking (Figure 3.20 and Figure 3.21). This event is not clearly identified in the waveforms or the spectrogram (Figure 3.20) and is presumed to be a low-magnitude local event based on the audio results. We note a high-frequency signal is present in the BAHB data stream, which appears as an emergent signal and persists for many minutes and is shown in the high-pass filter results starting at ∼12.25 hours (Figure 3.20). The audio results for entire day of 11 April 2012 indicate the high-frequency energy is present in the early hours of the day and diminishes ∼2 hours before the IOE wave arrivals, then returns at ∼12.25 hours. For the purpose of this analysis, we choose to ignore this signal since we cannot match the arrival of the emergent signal at any of the other regional stations. The STA/LTA results (Figure 3.22) do indicate a seismicity rate increase ∼6 hours before the TFZ M7.0. This is confirmed with the audio analysis with the rapid succession of foreshocks starting at the beginning of 12 April 2012 (DOY103). Similarly, the cumulative energy also shows an increase in high-frequency energy in the hours prior to the M7.0 (Figure 3.23).

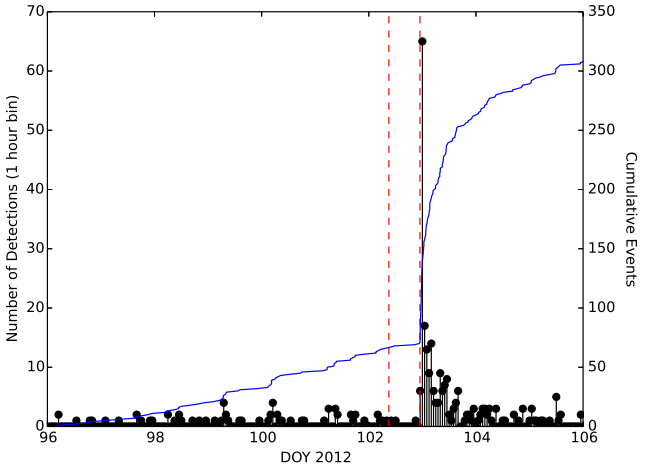

Figure 3.18: Match template results converted to an hourly rate for station MMIG from 5-15 April 2012. Cumulative number of events is shown with blue curve and red lines indicate the time of the IOE and MSZ earthquakes. Rate curve does not indicate precursory activity during the delay period between the M8.6 IOE stress perturbation and the M6.7 shown with two red dashed lines.

We generate 20 templates with an 8 second duration from the cataloged foreshocks and aftershocks associated with the M7.0 mainshock and 73 additional templates from visible inspection of the waveforms for a total of 93 templates. In the template selection process, we carefully select events as impulsive earthquake signals that we detect by manually scanning the waveform records and ignore the emergent signal previously described. The match template results indicate minimal microseismic activity in the 5 days prior to the IOE (Figure 3.24 and Figure 3.25). Consistent with the spectrogram analysis, we do not find triggered earthquakes during the IOE surface waves or an increase in the first 14 hours following the IOE surface waves. We do observe an increase in the seismicity rate in the hour before the surface waves of the M6.7 MSZ mainshock, located ∼1575 km to the southeast and described in Michoacán Results, which persists until the M7.0 TFZ mainshock and is consistent with the STA/LTA results. We observe a foreshock sequence that initiates following the surface waves from the M6.7 MSZ earthquake, which cascades to the 12 April 2012 04:54 M3.9 SSN catalog event, 145 minutes before, and the M 6.0 foreshock 9 minutes before the M7.0 TFZ mainshock. We estimate the transient Coulomb stress in the TFZ from the M6.7 MSZ at ±0.8 kPa.

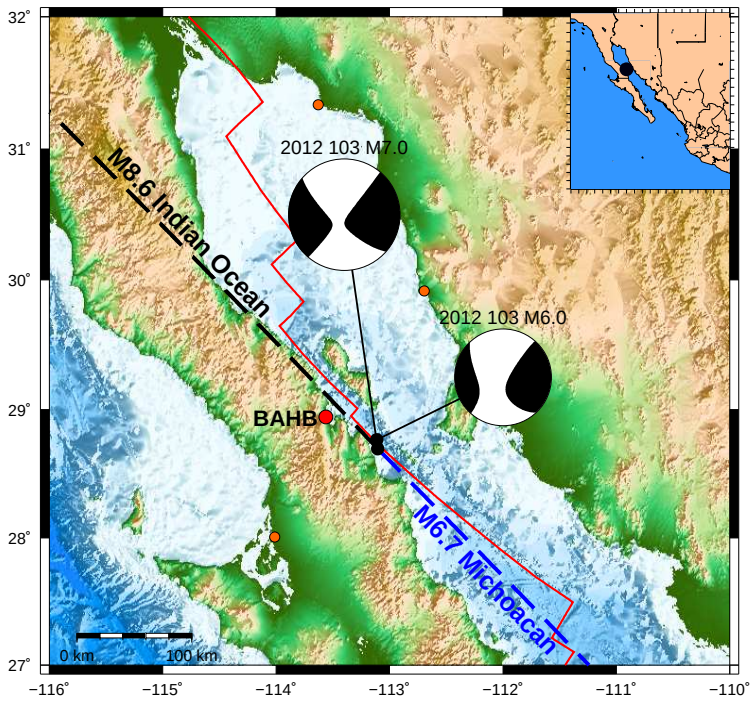

Figure 3.19: The central Gulf of California TFZ with the 12 April 2012 M6.0 and M7.0 moment tensors (`earthquake.usgs.gov`). Black and blue dashed lines indicate the back azimuth orientation to the M8.6 IOE and M6.7 MSZ earthquakes. Both travel paths are subparallel to the fracture zone. Station BAHB is shown with a red circle and is located ∼50 km from the mainshock. Additional stations are shown as orange circle and are located >125 km from the area of activity with a low signal to noise ratio that limits observation of small events.

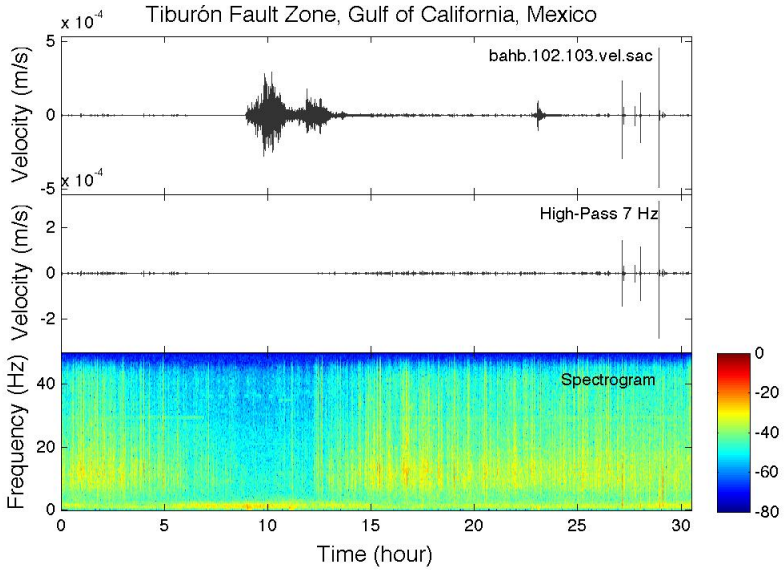

Figure 3.20: Waveform records of the vertical channel at station BAHB showing the entire day of the IOE and the time period leading up to the TFZ M7.0. Top panel is the original data, middle panel is the filtered data and the bottom panel is the spectrogram. The spectrogram does not indicate any evidence for immediate triggering during the IOE surface waves and this is confirmed with audio files. The high frequency energy at ∼11.2 hours is the arrival of the seismic waves from the M8.2 IOE aftershock. The event at ∼23 hours is the MSZ M6.7 followed by local foreshocks. We note the presence of minutes-long, tremor-like waveforms with high frequency energy in both the high-pass filtered waveforms and the spectrogram that are not representative of earthquake activity and similar signals are present in each day of the waveform records we obtained.

3.5 Discussion

3.5.1 Delayed dynamic triggering in each fault zone

The three fault zones we investigate each indicate ongoing, low-magnitude seismic activity in both the template matching and STA/LTA results, and this is not surprising for the rapid deformation. We do detect a few events during the passage of surface waves and each of these occur during the M8.2 IOE aftershock, not during the initial long period shaking induced by the M8.6 IOE. The spectrogram and audio results indicate three events in the BFZ and one event each in the MSZ and TFZ that were possibly triggered during the M8.2 aftershock. The STA/LTA cumulative event curves show an increase in activity in the BFZ the day before the IOE, the MSZ shows a reduction of events initiating two days before, and the TFZ shows a near constant rate of events before the IOE. Essentially, each fault zone contains

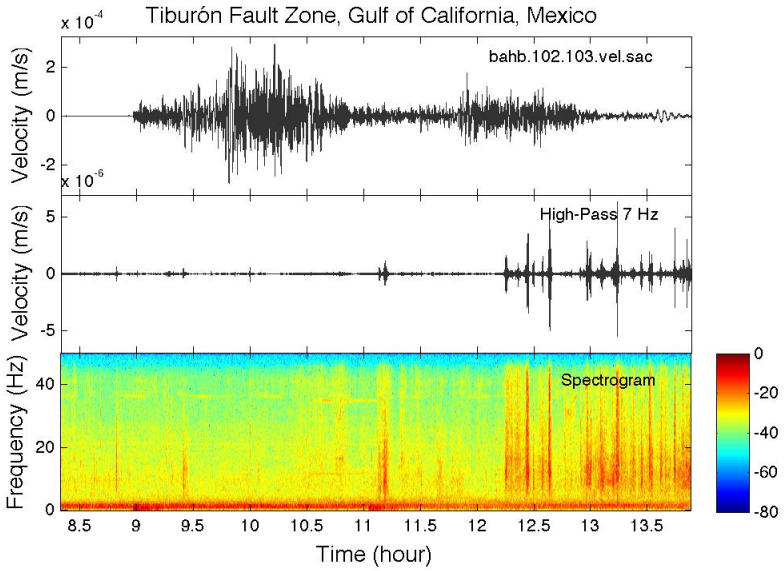

Figure 3.21: Spectrogram for station BAHB during IOE surface wave

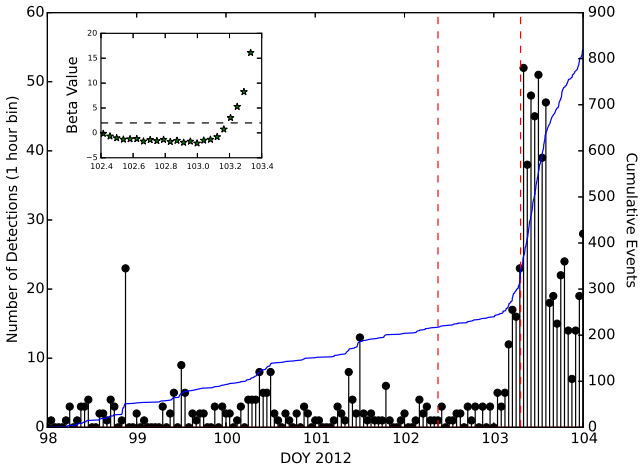

Figure 3.22: STA/LTA results for station BAHB from 7-13 April 2012 (DOY98-104). The blue curve is the cumulative events and the black stems are the number of detected events per hour. The largest increase in event count occurs in the hours before the TFZ M7.0 (dashed red line on right). The figure insert shows the calculated β-statistic values, which indicate a rate change exceeding 2 standard deviations in the hours before the mainshock during the foreshock sequence.

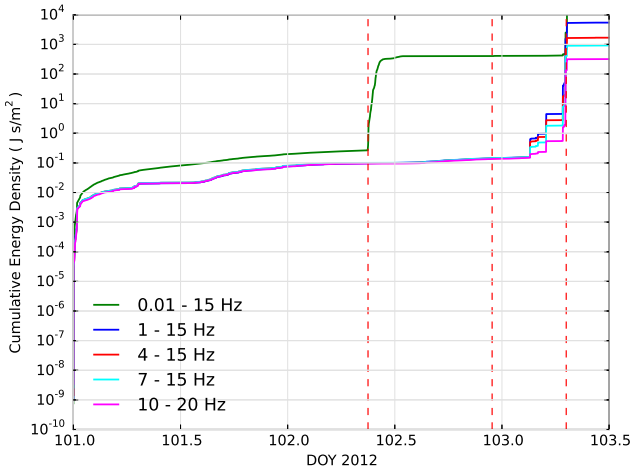

Figure 3.23: Cumulative energy density is shown for multiple bandwidths. The dashed red lines indicate the times of the IOE, MSZ, and the TFZ from left to right. An increase is observed in the 6 hours prior to the mainshock and is consistent with the STA/LTA results and the template matching results.

different changes in seismicity rates during the days before the local mainshock and all three culminate in a M≥6.0 mainshock. To further assess the significance of the rate change we need a much longer time period of microseismic events that includes location and magnitude to establish a more robust background rate that can support the daily rate fluctuations we observe. With the current data set this is challenged by the lack of spatial station coverage.

Both the template matching and STA/LTA results for all three study areas do not suggest a change in earthquake rates that initiates with the timing of IOE surface waves. Instead, the change is seismicity rates we observe occurs more than 2 hours after the onset of shaking and this delayed response is consistent with catalog studies (Parsons and Geist, 2014). Pollitz, Stein, et al. (2012) postulates the long duration (100s of seconds) of shaking at elevated strains (>0.1 μstrain or ∼3kPa) is a contributing factor for dynamically triggering large magnitude events. The immediate triggering we observe supports this argument with fault patches failing during the second period of transient loading. The transient stresses associated with the passage of surface waves from the IOE is variable in each fault zone (Table 3.1) and is dependent on the source faulting mechanism with respect to the receiver fault orientation and distance from the source (Gomberg and Bodin, 1994; Gonzalez-Huizar and Velasco, 2011; Hill, 2012). At these remote distances, the transient Coulomb stress changes we estimate from the modeled IOE surface wave displacements are on the order of ±1-10 kPa (Table 3.1), with the greatest in the TFZ. Our results for the TFZ do provide evidence for a foreshock sequence initiating after multiple episodes of cyclic loading, but we are limited by a high-frequency noise that may mask the onset of additional small events closer in time to the surface waves of the IOE to show a direct seismic connection. A plausible explanation for

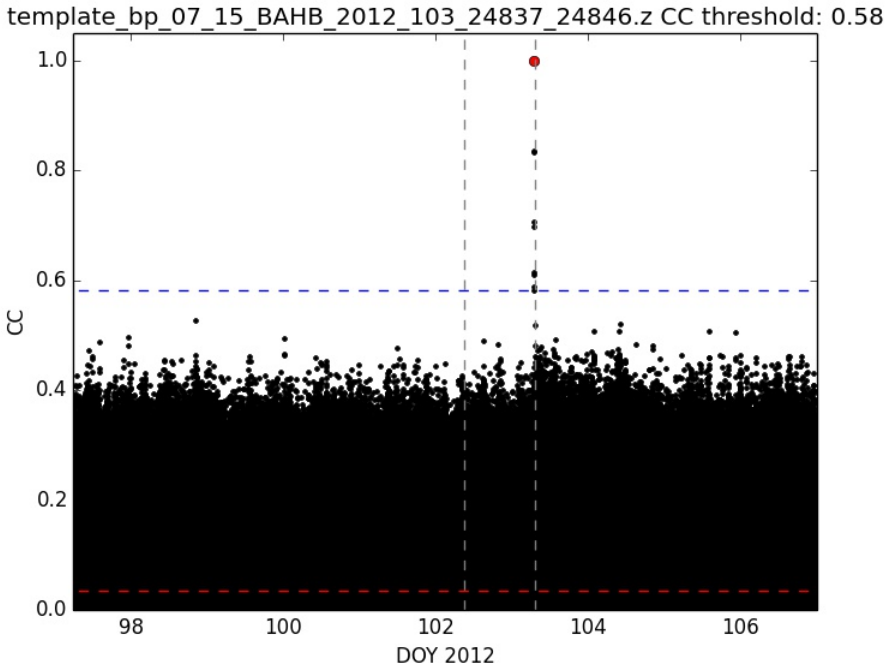

Figure 3.24: BAHB template cross-correlation example when template only matched itself. Black dots are CC values and red circle are event picks above CC threshold shown in figure title. Black dots above the blue dashed line are events above threshold and not counted twice.

the delayed response is the transient loading from two remote large-magnitude events with similar location, fault mechanism, and orientation that initiated a failure process, then the repeat passage of surface waves as they circle the Earth contributed to the large magnitude triggering (Peng, Wu, et al., 2011).

3.5.2 Triggered M>5 earthquakes indicate a time-dependent failure process

Seismicity catalogs indicate that no M>5 remote earthquakes are known to immediately trigger during the passage of surface waves (Johnson, Bürgmann, et al., 2015; Parsons and Velasco, 2011), with the caveat that global catalog records may be incomplete during the hours following a large magnitude earthquake (Iwata, 2008). The absence of remote M>5 dynamically triggered earthquakes may suggest that these larger events are not susceptible to immediate failure during the rapidly changing transient stresses during the surface wave passage (Parsons, Kaven, et al., 2012). Instead, a >8 hour delay period after the passage of surface waves appears to be required before the onset of triggered larger events (Bodin

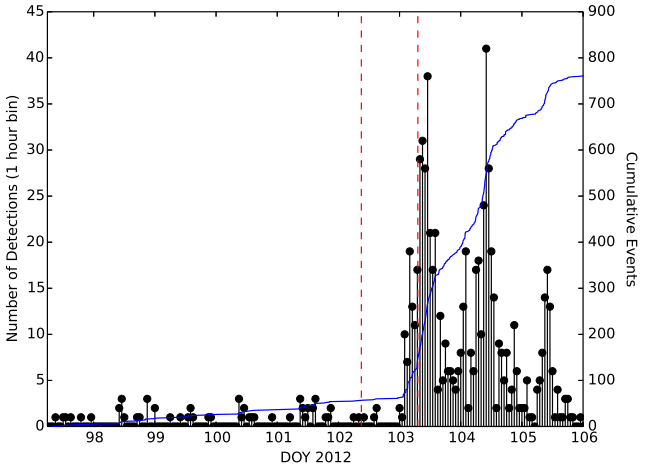

Figure 3.25: Match template results from the BAHB station are converted to an hourly rate and shown for 6-15 April 2012. The cumulative number of events is shown in blue and the red lines indicate the time of the M8.6 IOE and M7.0 TFZ earthquakes. Seismicity rate does not and increase prior to the M8.6 IOE. The increase in microseismic activity is greatest 15 hours after the IOE surface waves and remains elevated until the M7.0 TFZ mainshock.

and Gomberg, 1994; Gonzalez-Huizar, Velasco, et al., 2012; Parsons and Geist, 2014; Pollitz, Stein, et al., 2012). Our results indicate an increase in seismicity rates in the BFZ (Figure 3.8) and the TFZ (Figure 3.22) are consistent with a >8 hour delay period before a triggered M>5 mainshock with the largest perceptible change in microseismicity detected many hours after the onset of transient loading from the IOE earlier that day. However, we do find events occurring during surface wave passage, suggesting the possibility of a static stress change from these smaller events to critically stressed locked patches that ultimately fail. For this assumption to be plausible, the triggered events must be located very near the mainshock hypocenter because static stress changes decay as 1/r3 from the source. Using a simple in-plane static shear stress calculation (Chen et al., 2013), a M2 earthquake would result in ∼0.66 kPa stress change and a M3 event would result in a ∼20 kPa stress change within 1 km of the event. The data resolution does not allow us to explore the possibility of these static stress changes due to the lack of magnitude and location information of the detected events.

We present evidence showing transient stresses that coincide with M≥6.0 earthquakes in the following 24-hours, but do not address the question of whether this global sequence of large-magnitude earthquakes itself could be a random occurrence. Using a compilation of regional earthquake catalogs that include a lower magnitude of completeness for actively monitored regions, Parsons and Geist (2014) investigate seismicity rate changes following 260 global M≥7.0 mainshocks and do not find a uniform response, with only 2-3% of the mainshocks remotely triggering low-magnitude earthquakes. Looking at larger earthquakes

spanning a 30-year period, Parsons and Velasco (2011) find no increase in M>5 events beyond 1000 km following 205 M>7 mainshocks. When examining both catalog and waveform records, the number of observations of M>7 earthquakes remotely triggering earthquakes within the first hour of a stress perturbation deviates below Gutenberg-Richter scaling for the expected number of triggered M>5 earthquakes, given the observed rate of triggered low-magnitude events (M<4) (Parsons and Velasco, 2011; Velasco et al., 2008). This apparent deficit of rapidly triggered M≥5.5 earthquakes illuminates the challenge of identifying delayed dynamic triggering of larger earthquakes if no evidence exists in the data, either seismic or aseismic, to support the onset of a failure process at the time of a transient stress. Similarly, Parsons, Segou, et al. (2014) examine clusters of global M>5.6 earthquakes between 2010-2014.3 and do not find deviations in the natural fluctuation above the 95% confidence level assuming a temporal Poisson process. However, the IOE is shown to have enhanced M>5.5 for 10-days and suppressed M>6.5 global earthquakes for 95-days suggesting that transient stresses are altering global fault systems and do require a physical explanation (Pollitz, Stein, et al., 2012; Pollitz, Bürgmann, et al., 2014). The global increase following the IOE is a unique occurrence that has been observed only once during the 24-hour period following a M≥7.5 mainshock when examining 35-years of M≥5.5 seismicity (Johnson, Bürgmann, et al., 2015). Our thorough analysis of seismicity in the three fault zones of interest does produce consistent observations for immediate triggering of a foreshock after >2 hours of shaking, but we lack additional data to further investigate the possibility of aseismic deformation occurring between the transient stress and the delayed M≥6.0 earthquakes.

The 16 M≥5.5 triggered earthquakes reported by Pollitz, Stein, et al. (2012) all occur more than 14 hours after the IOE suggesting a failure process must exist that is more complex than Coulomb failure for these larger events (Hill, 2015). The IOE did immediately trigger remote tremor and low magnitude earthquakes (M<4) during the surface wave passage (Aiken, Peng, and Chao, 2013; Aiken, Zimmerman, et al., 2015; Fuchs et al., 2014; Gomberg, 2013; Linville et al., 2014; Tape et al., 2013). However, the data resolution in the study areas is not applicable to resolving triggered tremor. Further exploration of the catalog records for the 12 additional delayed dynamically triggered earthquakes reported by Pollitz, Stein, et al. (2012) indicate that 4 of these events do have M<5.5 events within 50 km that occur during the time period between the IOE transient stress and the mainshock of interest. The first is a M4.4 in offshore Japan on 13 April 2012 in the 2011 M9.0 Tohoku aftershock zone, which occurs temporally between two M≥5.5 earthquakes rupturing ∼30 and ∼50 hours after the IOE. Delorey, Chao, et al. (2015) attribute the triggering of the two offshore Japan earthquakes to a weakening of the forearc normal faults due to dynamic shaking with an observed increase in microseismicity and increase in seismic velocities in the wake of the IOE surface wave train. The second low-magnitude event occurs offshore of Chile on 15 April 2012, two days prior to the M6.7 Valparaiso, Chile mainshock. The third event occurs on 19 April 2015, two days prior to the M6.7 Papua, Indonesia mainshock. The fourth event occurs on 12 April 2012, eight days before the M5.7 mid-Atlantic ridge mainshock. Consistently, all these earthquakes occur within an active plate boundary zone and do not provide causal evidence for delayed dynamic triggering as the delay times are

considerably greater than the 24-hour period we more thoroughly investigate. Each of these additional events would require additional analysis that is beyond the scope of this work to verify changes in microseismic activity that can be directly related to the IOE if a seismic station is proximal to the mainshock.

Conversely, a M_b5.5 earthquake did rupture in Adak, Aleutian Island, Alaska, 8 minutes after the M8.6 P-wave arrival and ∼1 minute before the S-wave arrival. Upon visual inspection of the Alaska waveforms, the S-wave arrival is not clearly observed but the timing is determined using the ak135 travel-time-table (Kennett et al., 1995) and this event ruptures several minutes before the large amplitude surface wave arrival. Although not nearly as common as surface-wave triggered earthquakes, P-waves are capable of triggering tremor (Ghosh et al., 2009; Shelly, Peng, et al., 2011) and earthquakes near volcanic sources (Miyazawa, 2012) and this M_b5.5 may represent another observation of this triggering phenomenon in a volcanic environment.

3.5.3 Observed seismicity changes

Two regions we investigate, the BFZ and TFZ, show an increase in seismic activity many hours after the IOE and before the M≥6.0 mainshocks. In both the BFZ and TFZ, the fault plane orientation is more favorable for maximum Love wave induced transient stress (Hill, 2012) with a subparallel azimuth to the arriving surface waves from the IOE (Figure 3.5 and Figure 3.19). Our observations suggest that the triggered mainshocks located in transtensional tectonic environments exhibit a more pronounced response to the transient stresses when compared to the compressional environments found in the MSZ. The oblique divergent tectonic environment in these two fault zones is optimal for dynamically triggering M<5 earthquakes due to reduced compressive stress on the faults when compared to convergent tectonic regions (Hill and Prejean, 2015; Prejean and Hill, 2009). The M8.6 IOE could have initiated a time-dependent, but nominally aseismic, failure process during the transient loading (Shelly, Beroza, et al., 2007; Taira et al., 2009). Then the continued stressing from the surface waves of the M8.2 aftershock provided enough additional loading to immediately trigger the microseismic events we observe (Figure 3.6 and Figure 3.20) and further enhance the previously initiated time-dependent failure process that resulted in the delayed dynamic triggering of a M≥6.0 earthquake.

With regards to the duration of shaking as a contributing factor to delayed dynamic triggering, the TFZ experiences additional transient stressing during the MSZ M6.7 surface wave passage that ruptured 1575 km to the SE. Our results indicate a rapid increase in microseismic events following the MSZ mainshock that cascade into the M7.0 TFZ earthquake. The seismicity rate curves and the cumulative energy density in the TFZ (Figure 3.22, 3.23, 3.25) do indicate an increase before the MSZ M6.7 that continues to increase, and then accelerate, after the additional loading. To note, the calculated transient stresses from the M8.2 IOE is 30% (∼3.0 kPa) and the MSZ are ∼7% (0.8 kPa) of the IOE. However, we suggest that the preferred fault orientation with many hours of cyclic loading in the TFZ prior to the M7.0 primed the fault system for failure and should not be discredited as a

contributing factor in the failure process. Considering the fault orientation with regards to peak transient stressing as a contributing factor to the failure process assumes the fault is already late in the seismic cycle. A question that remains is whether or not the triggered large events would have occurred without the transient loading from the M8.2 aftershock that immediately triggered events in each fault zone. Further studies are needed to differentiate the conditions required to trigger both small and large earthquakes in different tectonic environments, as well as the statistical significance of fluctuations in seismicity with respect to transient loading.

3.6 Conclusions

We investigate delayed dynamic triggering in three offshore fault zones following the 2012 M8.6 IOE by examining changes in seismicity prior to the rupture of three remote M≥6.0 mainshocks. Template matching and STA/LTA results both suggest ongoing low-magnitude seismicity in each fault zone prior to the IOE. We estimate transient Coulomb stresses on the order of 1-10 kPa for ∼4 hours during the passage of surface waves from the IOE and an associated M8.2 aftershock. We find possible evidence of immediate triggering of small-magnitude events during the passage of surface waves from a M8.2 aftershock that occurred two hours after the IOE. Rate increases occur in two transtensional fault zones prior to the M≥6.0 mainshocks that initiate after multiple hours of transient loading. No change of activity is observed in the subduction environment we investigate, supporting evidence that dynamic triggering is more plausible in extensional environments. We conclude that the long duration of transient loading in conjunction with the occurrence of small earthquakes during the surface wave passage advanced the seismic cycle for the three M≥6.0 events investigated in this study.

Chapter 4

Depth Migration of Seasonally Induced Seismicity at The Geysers Geothermal Field

Published as: Johnson,C.W., E.J.Totten, and R. Bürgmann (2016), Depth migration of seasonally induced seismicity at The Geysers geothermal field, Geophys. Res. Lett., 43,61966204, doi:10.1002/ 2016GL069546

4.1 Abstract

Seismicity from injected fluids provides insight into the hydraulically conductive fracture network at The Geysers, California (TG) geothermal reservoir. Induced earthquakes at TG result from both thermo- and poroelastic stresses as injected fluids cool the rocks and increase pore pressure. The spatio-temporal evolution of M$\geq$1.5 seismicity is characterized as a function of depth in the northwest and southeast regions of TG to develop time-dependent earthquake rates using an Epidemic Type Aftershock Sequence model. The seismicity and injection follow an annual cycle that peaks in the winter months and is correlated by depth. The results indicate a time lag of $\leq$6 months for fluids to migrate >3 km below the injection depth. Water injection is the main cause of seismicity as fluids penetrate into the reservoir. The results suggest a steeply dipping fracture network of hydraulically conductive faults allows fluid migration to a few kilometers below the point of injection.

4.2 Introduction

The Geysers geothermal reservoir (TG), located in northern California (Figure 4.1), began operations in 1960 and is the largest geothermal power facility in the world. A decrease in reservoir steam pressure beginning in 1987 led to the construction of tertiary wastewater supply pipelines in 1998 and 2004 to augment existing water injection facilities. Large-volume

fluid injection into the subsurface has long been recognized to induce earthquake activity in the host rock (Evans, 1966; Healy et al., 1968). TG is no exception with fluid injection known to induce seismicity (Eberhart-Phillips and Oppenheimer, 1984; Majer et al., 2007; Marks et al., 1978; Stark, 1991; Trugman et al., 2016). The focus of this study is to quantify the seismicity rates at the TG using time-series characterizing specific depth intervals within the reservoir to illuminate the first-order depth migration of fluids in response to injection.

TG is a sub-hydrostatic vapor reservoir of fractured Franciscan metagraywacke above a Pleistocene felsite intrusion (Hartline et al., 2015). The normal reservoir extends to a depth of ∼2.5 km with a temperature of ∼240°C in both the northwest (NW) and southeast (SE) region of TG. In the NW a high temperature zone (HTZ) exists from ∼2.5-4.0 km depth where temperatures increase to ∼340° C (Beall, Wright, et al., 2010; Stark, 2003; Walters and Combs, 1992). The injection interval depth at TG for the largest injection wells are within the upper 2.1 km of the reservoir (Gritto, Dreger, et al., 2014). Induced seismicity near the injection and production wells is more common in the NW than the SE (Beall, Wright, et al., 2010). Beall and Wright (2010) identify a boundary that divides TG into a NW and SE region based on the extent of the HTZ and the location of 90% of the M≥3 seismicity. The induced seismicity in the NW extends to ∼5 km depth with a time lag of 3-5 months following peak injection suggesting that fluids penetrate into the HTZ (Beall, Wright, et al., 2010; Stark, 2003).

In this study, we characterize seismicity at TG by depth and quantify the time lag as fluids migrate deeper into the reservoir. Seismicity rates can be used to detect and characterize transient stresses (Hainzl and Ogata, 2005; Marsan et al., 2013), in particular forcing from fluid injection and extraction (Brodsky and Lajoie, 2013). We explore the fluid migration from the injection interval depth to greater depths by correlating the seismicity rate time-series with the gross injection and production monthly totals. Our objective is to characterize the large scale spatiotemporal patterns of the induced seismicity in the SE and NW and to compare our results to site-specific geomechanical models at TG that describe thermoelastic and poroelastic strains related to injection (Jeanne, Rutqvist, Hartline, et al., 2014; Kwiatek et al., 2015). We present results that support the migration of fluids deeper into the reservoir following an annual cycle of large volume injection.

4.3 Data

4.3.1 Seismicity Catalog

In 2003 the Lawrence Berkeley National Lab (LBNL) began operating a 31-station monitoring array at TG for microseismicity detection. The seismicity catalog produced by LBNL is available from the Northern California Earthquake Data Center using the Enhanced Geothermal Systems Earthquake Catalog search (`http://ncedc.org/egs/catalog-search.html`, last accessed on 01 December 2015). The catalog is limited to the active production field (Figure 4.1) and contains 360,307 $M_L \geq 0$ events from 01 January 2005 to 31 December

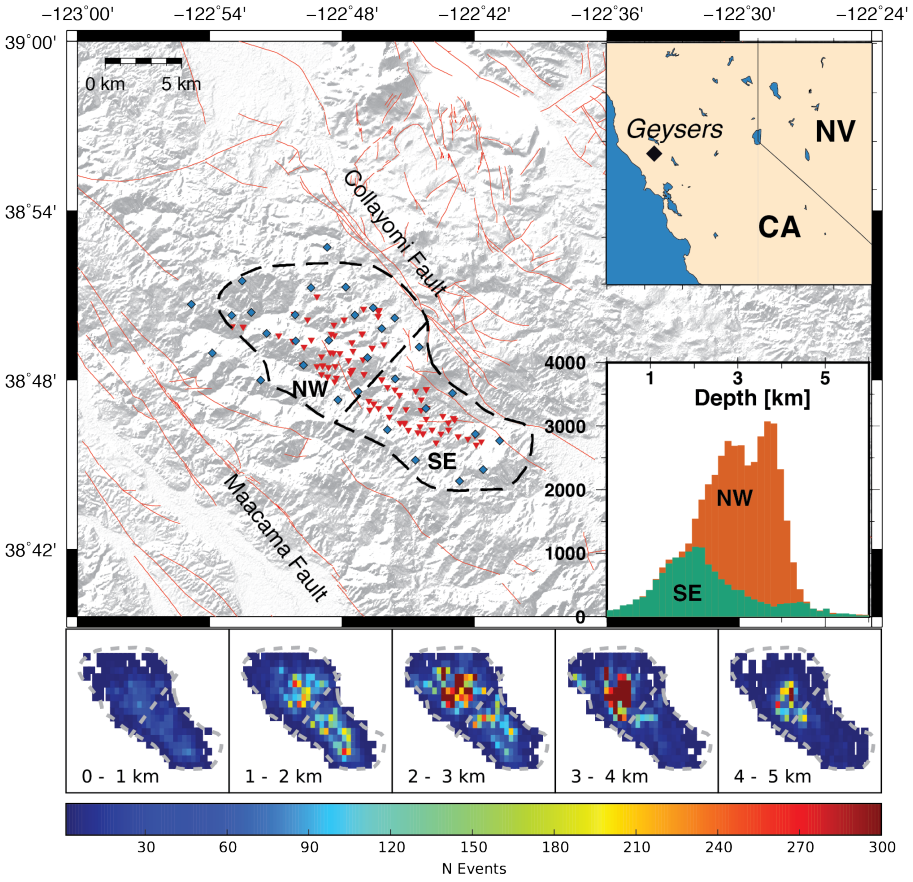

Figure 4.1: The Geysers (TG) geothermal field in northern California (top-right insert) lies between the Maacama Fault and Collayomi Fault. The reservoir is outlined with a black dashed line and divided into NW and SE regions by the dashed line across the reservoir. Blue diamonds indicate the local seismic network and red inverted triangles are the active injection wells during 2005-2015. Red lines are the USGS mapped faults (`http://earthquake.usgs.gov/hazards/qfaults/`). The bottom right insert is the depth distribution for the M≥1.5 earthquakes in the NW shown in orange and SE shown in green between 2005-2015. The five bottom panels show the total number of M≥1.5 catalog events by color per 0.75 km grid cell for the corresponding depth interval.

2014, with 13 $M_L \geq 4.0$ events in the study area. Event hypocentral locations are obtained using standard single-event location techniques with SimulPS (Thurber, 1983) for a three-dimensional velocity structure that is updated annually (Hutchings et al., 2015). Using the reported errors, we estimate the mean horizontal and vertical uncertainty of 210 m and 400 m, respectively, for the events used in this study. We estimate a catalog magnitude of completeness of $M_c 1.1$ using the maximum curvature method (Wiemer and Wyss, 2000) and a b-value of 1.325 ± 0.007 using the maximum likelihood method (Aki, 1965; Bender, 1983) with 2σ confidence intervals (Shi and Bolt, 1982) (Figure 4.2). To ensure a complete catalog and stability for the seismicity modeling presented in Section 3, we implement a magnitude cutoff of $M_L 1.5$ and use the remaining 60,703 earthquakes during the 10-year study period.

For the analysis we separate TG into NW and SE regions (Beall and Wright, 2010; Convertito et al., 2012) as outlined in Figure 4.1 and 94% of the earthquakes are located at a shallow depth of 0-5 km. When the events are separated by region, the depth distributions indicate shallower events in the SE with the majority occurring at a depth interval of 1-2 km (see inset histogram in Figure 4.1). The NW region contains 66% of the events and there is a bimodal distribution of depths with peaks at ∼2.5 km and ∼4.0 km depth, which agrees with long-term trends for the depth distribution at higher magnitudes in the reservoir (Trugman et al., 2016). Additionally in Figure 4.1 we show the spatial distribution of earthquakes at 1 km depth intervals for a 0.75 km square grid. The spatial distribution by depth in Figure 4.1 shows that the concentration of earthquakes correlates with the locations of injection wells and that the seismicity deepens from SE to NW.

4.3.2 The Geysers Injection Well Records

The California Department of Conservation Division of Oil, Gas, and Geothermal Resources is the state repository for all non-confidential geothermal field records (`http://www.conservation.ca.gov/dog/geothermal/`). The data is publicly available and records for TG are available from 1997 - 2014. We obtained monthly injection and production data between January 2005 to December 2014 and make no assumptions about unreported wells. We assemble the data as a time-series for each well and the gross total mass is summed for the NW and SE regions of TG (Figure 4.1). The records do not include the injection well depth and we rely on reported injection interval depths <2.1 km for 49 highest-volume injection wells throughout the reservoir (Gritto, Dreger, et al., 2014). From this we infer in the NW >95% of the injection depths shown are in the injection interval between 0.9-1.5 km and in the SE >90% of the injections occur between 0.0 - 0.9 km. The subsurface location of the wells do not deviate by more than 1 km from the surface wellhead location [see Figure 3 in Boyle and Zoback (2014)].

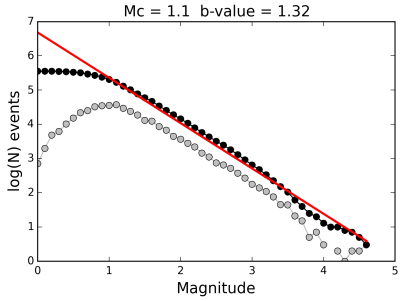

Figure 4.2: Shown in gray circles is the magnitude frequency distribution for 360,307 M≥0 events from the Enhanced Geothermal Catalog from 01 January 2005 to 31 December 2014. Black circles are the cumulative distribution. The magnitude of completeness M_c is estimated to be M1.1 using the maximum curvature method. The b-value is estimated to be 1.325 0.007 using the maximum likelihood method and 2σ confidence interval. The red line has a slope of b for the M_c. The catalog is limited to the area bound by the polygon (-122.733465, 38.814179, -122.716618, 38.796988, -122.692208, 38.782205, -122.663329, 38.774297, -122.656658, 38.769882, -122.661457, 38.747579, -122.678961, 38.735439, -122.719614, 38.734875, -122.724664, 38.735355, -122.733809, 38.737166, -122.760626, 38.755388, -122.807727, 38.775672, -122.841420, 38.792863, -122.855860, 38.803177, -122.887490, 38.834119, -122.892647, 38.850278, -122.867135, 38.864932, -122.843139, 38.867812, -122.787443, 38.868156, -122.758907, 38.859217, -122.736903, 38.837558, -122.735528, 38.821399).

4.4 Seismicity Modeling

Time-dependent background seismicity rates are calculated for all M_L1.5 events using the temporal Epidemic Type Aftershock Sequence (ETAS) model shown in Equation 4.1

$$\lambda(t,\theta) = \mu + \sum_{t_i<t} \frac{K e^{\alpha(M_i - M_c)}}{(t - t_i + c)^p} \tag{4.1}$$

where λ is the rate function, μ is the background seismicity rate, K is the aftershock productivity, α is the aftershock efficiency, and c and p are the Omori decay parameters, and θ is a vector of [μ, K, α, c, p] (Ogata, 1992). The ETAS model separates background events from the associated aftershocks and provides an estimate of the background earthquake occurrence rate for a given time interval. The best-fit parameters for the rate function λ are computed by maximizing the log likelihood function shown in Equation 4.2 (Ogata, 1992) for the event times and corresponding magnitude. We refer the reader to Zhuang, Harte, et al. (2012) for a complete review of temporal ETAS models.

$$\ln L = \sum_{i=1}^{N} \ln \lambda(t_i) - \int \lambda(t) dt \tag{4.2}$$

Fitting the model variables is a non-linear optimization problem and we minimize the negative log likelihood using a quasi-Newton algorithm (bfgs function in the SciPy package). Upon convergence we estimate the covariance and standard deviation for each best-fit parameter in the vector θ using Equation 4.3 (Ogata, 1999).

$$\sigma^2 = (J^{-1}); \quad J_{ij} = \frac{d^2 \ln L}{d\theta_i d\theta_j} \tag{4.3}$$

Formally, ETAS model fitting requires solving for five free variables and can result in trade-offs between values giving unreasonable solutions that do not agree with Omori law, Gutenberg-Richter scaling, or the network used to develop the catalog. For the model fitting in this study we elect to hold α and c constant using a priori information due to the unstable nature of ETAS inversions for catalogs with significant swarm-like earthquake activity (Brodsky and Lajoie, 2013; Hainzl and Ogata, 2005). The α value represents the aftershock productivity for a mainshock, where values less than 1.0 indicate low aftershock productivity (Felzer, Abercrombie, et al., 2004; Helmstetter, 2005). Here, we hold the α value constant at 0.75 based on previous studies analyzing seismicity in geothermal fields (Hainzl and Ogata, 2005; Trugman et al., 2016). We also perform all model calculations for an α value of 1.0 to ensure we are not biasing the results by our parameter selection. The second value we hold constant is the c parameter, which depends on the seismic network detection threshold and for a given magnitude of completeness. To determine the c value we modify the approach described by Brodsky and Lajoie (2013). See Figure 4.3 for a description of the method. We hold the c parameter constant at 43 seconds indicating that all events M$\geq$1.5 beyond this time interval are observed following a mainshock.

We estimate time-dependent earthquake background rates (Brodsky and Lajoie, 2013; Hainzl and Ogata, 2005; Marsan et al., 2013; Trugman et al., 2016) by fitting the ETAS model using a 6-month window of events and step through the time-series in 1.0-month intervals. This procedure is performed for 1.0 km depth intervals from 1.0 km to 5.0 km with respect to mean sea level. With the use of discrete intervals for the event selection we anticipate some correlation due to event interaction between intervals and depth uncertainty. For our time series generation we find similar results when shortening the moving window to 4-months, but observe short-term spikes in the time-series of background rate μ when reducing to 3-months or less (Figure 4.4). Extending the moving-window to longer time intervals provides smoother rate curves and does not change our results. Therefore we maintain the 6-month window for the analysis.

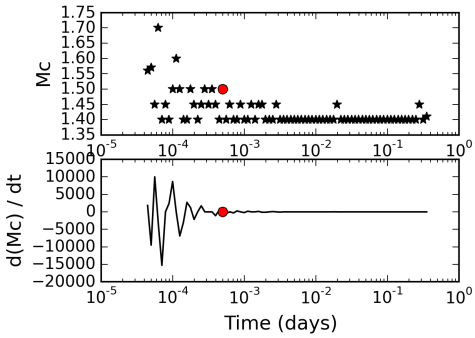

Figure 4.3: Earthquakes are binned according to the interevent time with respect to the prior earthquake occurrence time. For example, if a M2.0 event is followed 60 seconds later by a M1.8 event, then the M1.8 event will be binned according to the 60-second lapse time since the last event. Time bins are calculated using a 0.05 log unit interval from $10^{-}5.0$ to $10^{-}0.05$ days. The magnitude of completeness is then estimated for each set of events corresponding to the interevent time. Shown is the magnitude of completeness for each interevent time bin. The red circle is the M_c used in the analysis. (bottom) We then take the derivative $\frac{dM_c}{dt}$, where dt is the bin width used, and estimate the interevent time beyond which this derivative approaches the limit of zero, that is where M_c stabilizes. The derivative of the M_c series indicates that the interevent times stabilize at a time of 5x$10^{-}4$ days, or 43 seconds (red dot). All time bins above this 43 second interevent time are complete above M_c1.5. The 43 second value determined with this method is used as the constant c in the seismicity model inversion.

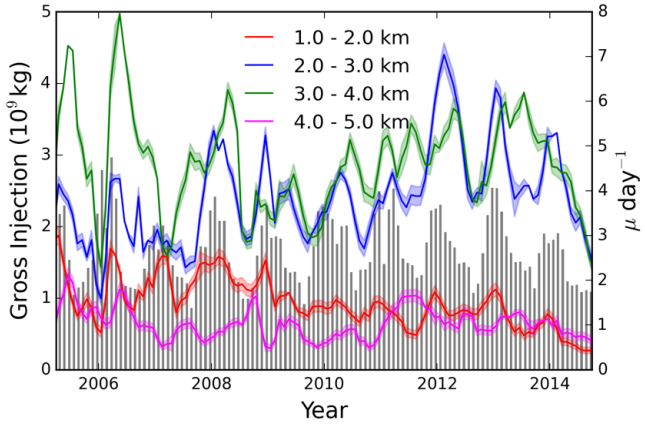

Figure 4.4: Seismicity rate curves produced using a 3-month moving window.

4.5 Seismicity Rates and Depth Dependence

The time series of monthly background seismicity rates for events between 1-5 km depth for the NW and SE study areas are shown in Figure 4.5 at 1 km depth intervals with the corresponding total monthly water injection mass. The time series are shown with one standard error on the order of 0.1 events per day. The ETAS model results indicate that 89% percent of the earthquakes are independent events for both the NW and SE region. The total number of events considered aftershocks changes by <0.5% when the α variable is held constant at 1.0 for the calculations. The rate curves indicate an annual period with peak seismicity rates following peak injection times. In the NW study area the rate curves indicate the highest seismicity rates and largest annual rate variations between 2-4 km, which is just below the injection well interval ranging from 0.9-1.5 km. The rate curves in the SE region are much lower with peak rates in the 1-3 km depth range and annual fluctuations are resolvable down to about 4 km.

We perform a 48-month moving window cross-correlation analysis to compare the seismicity rates with the monthly totals of gross injection, gross production, and net injection (injection less production). Figure 4.5 shows the correlation coefficient and time lag for maximum correlation for the gross monthly injection. For the NW region, we find an increase in the mean time lag from 0 to 6 months with increasing depth. The time lag at greater depths agrees with Beall, Wright, et al. (2010) observation of the occurrence of M≥3 events in the HTZ 3-5 months after peak injection. In the NW region of TG we find a correlation coefficient >0.5 for the 1-2 and 2-3 km depths for the study period with the exception of a few months in 2007 and 2010. For the 3-5 km depth intervals we also find good agreement but more variability shown by periods of low correlation. After 2007 the correlation values indicate a more systematic increase of time lag with increasing depth. The rate curves indicate fewer events per day in the 3-4 kilometer depth range and that rate decreases until 2010. The correlation curves for the SE region contain values above 0.5 for the 2-3 km depth range with a time lag between 2-5 months. Lower correlation with the injection is seen in the 1-2, 3-4 and 4-5 km depth interval before 2013. Even with the variability and low correlation values we do observe a general trend of time lag increasing with depth. We test shorter correlation windows and find similar results using a 24-month moving window and elect to use the smoother 48-month window (Figure 4.6).

Additionally we test for correlation with the production and the net totals (injection minus production) using the same procedure as described for the injection (see Figure 4.7 and 4.8). Our results indicate no correlation in the NW or SE region with the production values. The net injection totals produce nearly identical values as the injection since the steam production totals remain near constant throughout the year. We consider the injection as the main driver of the induced seismicity and do not explore further the production or net injection results.

The 10 years of M≥1.5 seismicity data is compiled by time-of-year and depth to illuminate the depth migration of seismicity with time using the entire catalog of events. Figure 4.9 shows the monthly average injection and production totals, the cumulative number of M≥1.5

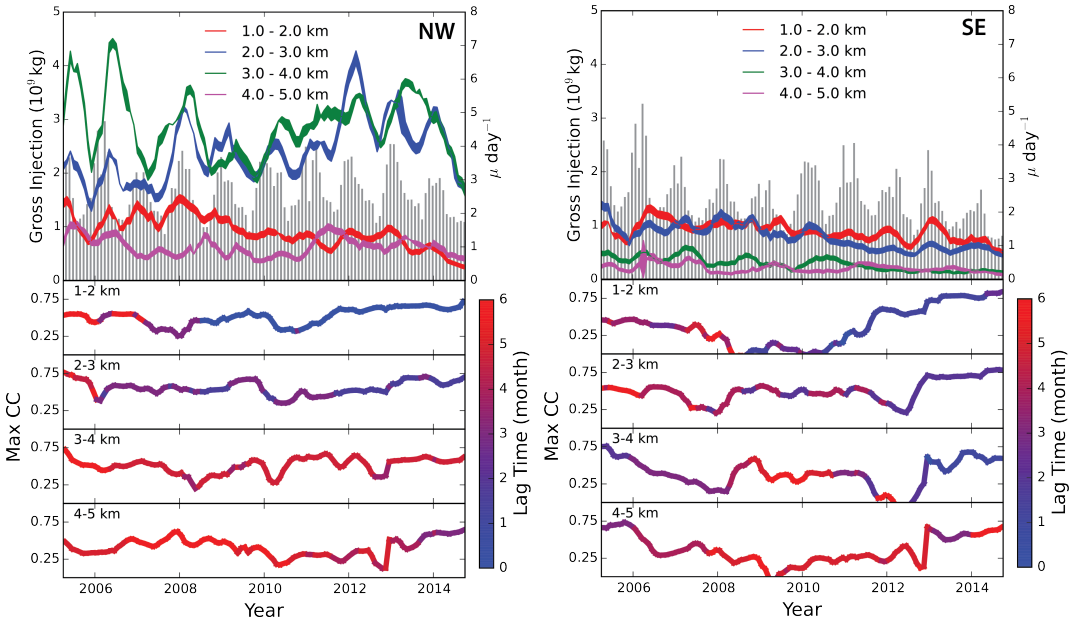

Figure 4.5: Background seismicity rates with monthly injection totals and cross-correlation time-series shown as a function of depth for the NW (left) and SE (right) regions as indicated in Figure 4.1. The top frame shows the monthly seismicity rates with the depth interval indicated by color. The gray bars in the background are the gross monthly injection totals for the two regions. The seismicity rate curves are calculated using the ETAS model with a 6-month moving window stepping forward in 1-month increments. The half-width of the curve indicates one standard deviation from the estimated rate. The lower panel shows the temporal variations in cross correlation coefficients for the background seismicity rate and injection at each depth interval using a 48-month moving window. The color of the curve represents the time lag in months for the maximum correlation coefficient.

events from the original catalog for every 0.5 km depth interval by 0.5 months, and the percent excess number of events in each bin for the NW and SE regions. The percent excess value is calculated by first reducing each depth interval by the depth interval average, then normalizing by the average number of events in that depth interval. Assuming downward fluid flow from the injection interval (Gritto, Dreger, et al., 2014), we include three linear diffusion curves in Figure 4.9 using Equation 4.4 for hydraulic diffusivity values (D) of 10.00, 1.00, and 0.10 $m^2\ s^{-1}$ to indicate a possible range of effective hydraulic properties in the reservoir and estimate the diffusion distance (d).

$$d = \sqrt{Dt} \tag{4.4}$$

The diffusion curves are positioned at January, the peak month of injection, and a depth of 1.5 km for the NW and 0.9 km for the SE corresponding to the lower extent of the depth

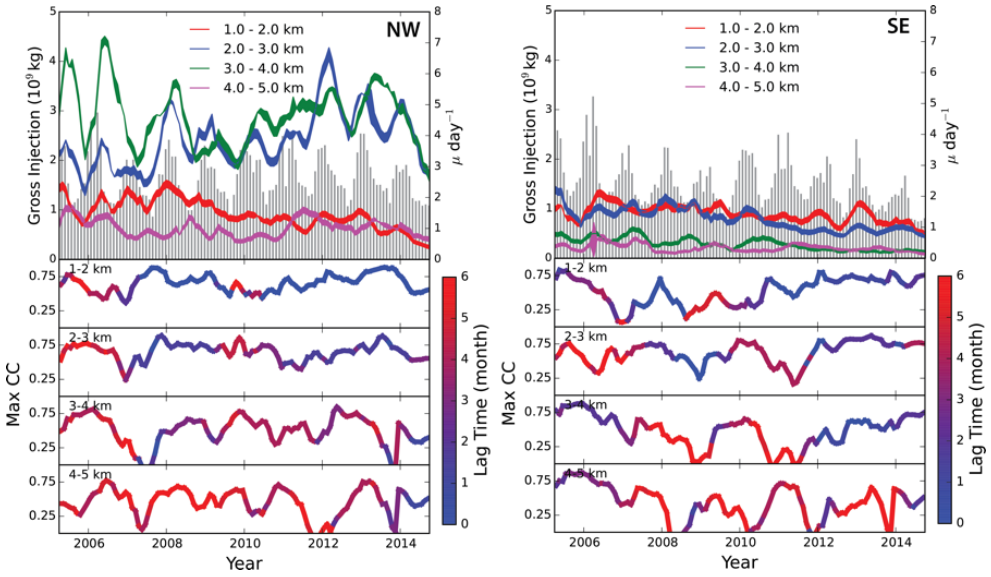

Figure 4.6: The top frame shows the monthly seismicity rates with the depth interval indicated by color and the gray bars are the gross monthly production totals. The seismicity rate curves are the same as Figure 4.5 and are calculated using the ETAS model with a 6-month moving window stepping forward in 1-month increments. The half-width of the curve indicates one standard deviation from the estimated rate. The lower panel shows the temporal variations in cross correlation coefficients for the background seismicity rate and production at each depth interval using a 24-month moving window. The color of the curve represents the lag-time in months for the maximum correlation coefficient.

interval where >90% of the injection wells are located (Gritto, Dreger, et al., 2014).

The NW region indicates near constant production throughout the averaged years and a peak in total injection in January (Figure 4.9a). The stacked seismicity in Figure 4.9c shows an increase of events in early November when monthly injection totals are increasing. Included are the time of year and depth of the M_L4.0 events in the NW region. The timing of the largest events corresponds to the maximum injection and increase in depth over time. The maximum number of events stays within the 2.0-3.5 km depth range for a period of ∼2.5 months before migrating ∼1 km deeper when injection totals begin to decline. Between February and June the greatest number of earthquakes are located at a depth of 3-4 km, which is much deeper than the injection depth interval of 1.5 km in the NW. The change in seismicity is an indication of fluid migration deeper into the reservoir. The deepening is more pronounced in Figure 4.9e with the normalized totals. We focus on the months and depths with more than 40 events and the excess events lie between the 0.1 and 1.0 $m^2\ s^{-1}$ diffusion curves.

We observe similar patterns in the SE region with near constant production and peak injection in January (Figure 4.9b). The number of events by depth (Figure 4.9d) is con-

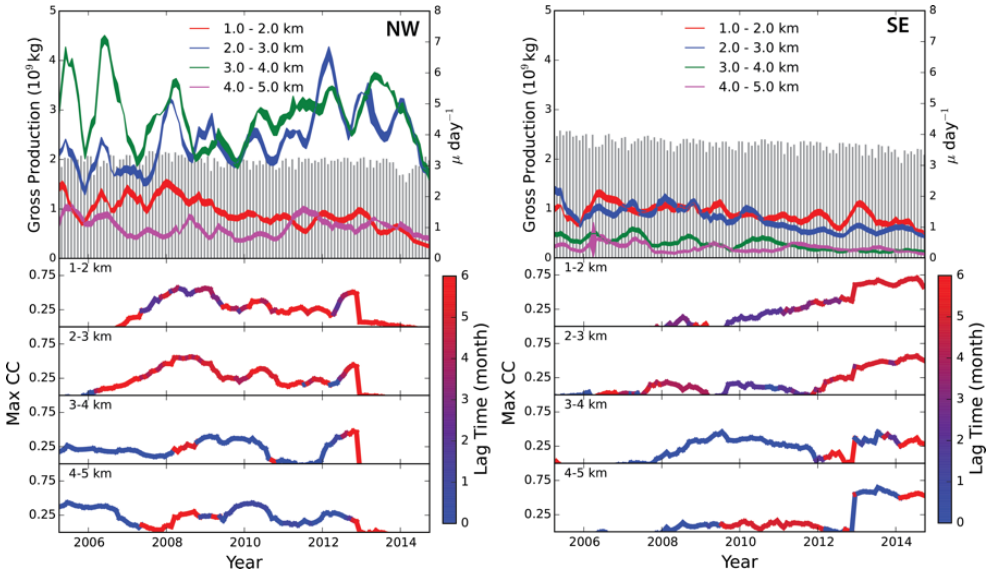

Figure 4.7: The top frame shows the monthly seismicity rates with the depth interval indicated by color and the gray bars are the gross monthly production totals. The seismicity rate curves are the same as Figure 4.5 and are calculated using the ETAS model with a 6-month moving window stepping forward in 1-month increments. The half-width of the curve indicates one standard deviation from the estimated rate. The lower panel shows the temporal variations in cross correlation coefficients for the background seismicity rate and production at each depth interval using a 48-month moving window. The color of the curve represents the lag-time in months for the maximum correlation coefficient.

strained to a shallower portion of the geothermal field, which agrees with the seismicity rate curves shown in Figure 4.5. Microseismic activity increases in November and peak activity occurs at ∼2 km depth when injection totals are maximum during December and January. After ∼4 months of high volume injection, increases in seismicity are observed to depths of ∼3.5 km. The normalized seismicity totals shown in Figure 4.9f indicate an excess number of events during the first 6 months of the year reaching a depth of >4 km. Similar to the NW, the peak excess event values concentrate between the 0.1 and 1.0 $m^2\ s^{-1}$ diffusion curve. Below 4 km we find excess events above the 1.0 $m^2\ s^{-1}$ diffusion curve, but this depth range contains less than 40 events per bin during the study.

4.6 Discussion and Conclusions

The use of the temporal ETAS model to characterize depth-dependent seismicity rates at TG allows for exploration of the spatio-temporal evolution and extent of induced seismicity in the reservoir. The seismicity rate curves show good correlation with fluid injection, but are not observed to respond to the extraction of steam in either the NW or SE region of the

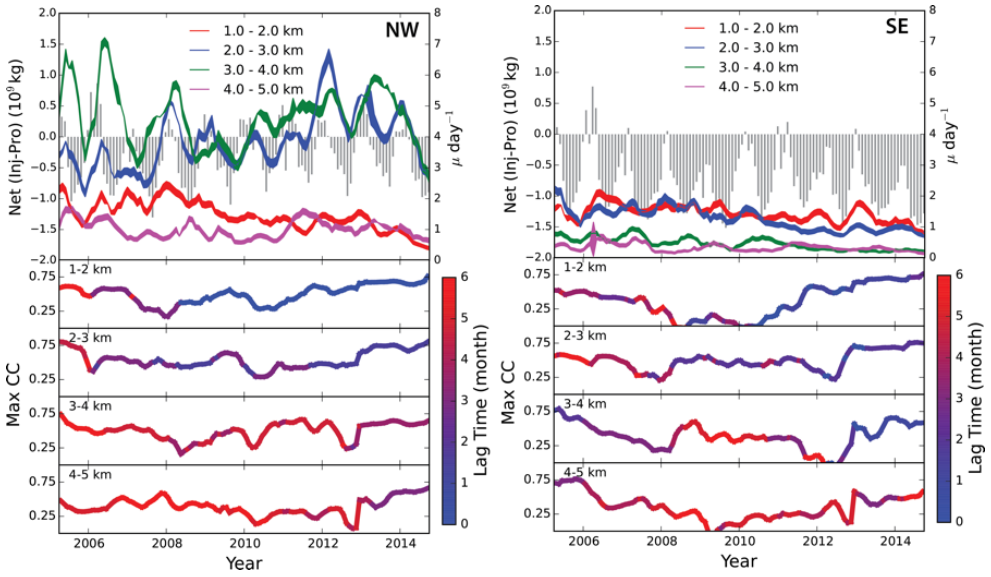

Figure 4.8: The top frame shows the monthly seismicity rates with the depth interval indicated by color and the gray bars are the gross monthly net injection totals. The seismicity rate curves are the same as Figure 4.5 and are calculated using the ETAS model with a 6-month moving window stepping forward in 1-month increments. The half-width of the curve indicates one standard deviation from the estimated rate. The lower panel shows the temporal variations in cross correlation coefficients for the background seismicity rate and net injection at each depth interval using a 48-month moving window. The color of the curve represents the lag-time in months for the maximum correlation coefficient.

geothermal field. This field-wide observation is consistent with wells in the northernmost region of TG (see Figure 9 in Kwiatek et al. (2015)) and supports the notion that fluid injection is the main driver of induced seismicity at TG (Majer et al., 2007) and references within].

In the NW region, the seismicity rates during 2005 - 2007 indicate a 2-5 month time lag for all depth intervals, while after 2007 there is no resolvable time lag in the shallow depth intervals (1-2 km) where most of the injection is occurring (Figure 4.5). Interestingly, Gritto and Jarpe (2014) find a ∼1-year time lag in time-dependent V_P/V_S tomography results from the start up of the Santa Rosa water injection project in 2004 until 2007, indicating a delayed elastic response to fluid injection. After 2007, the V_P/V_S results indicate no more time lag with injection. Our seismicity rates show that the time lags in the NW increase more uniformly with depth after 2007, indicating that more earthquakes are occurring near the injectors in both space and time as the reservoir becomes more saturated. Beall and Wright (2010) suggest that the delay in elastic response is the time needed to fully saturate portions of the reservoir previously not receiving injection water. In the SE region, the correlation values increase and the time lags decrease in the shallow portions of the reservoir, after 2010

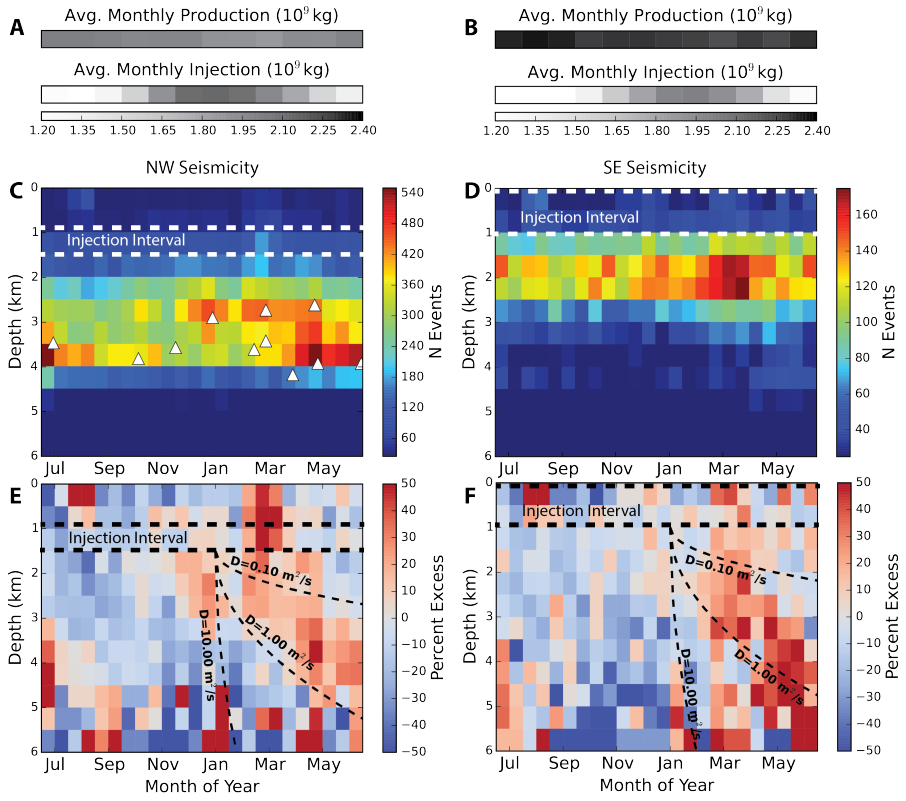

Figure 4.9: (A and B) The average monthly injection and production totals are shown for the NW and SE study areas in gray. Note the x-axis for A and B align with the lower panels and all are centered at December-January to more clearly represent the annual cycle of peak seismicity rates and fluid injection. The injection and production averages indicate peak injection in the winter months and production near constant throughout the year. The M≥1.5 events are shown by depth and time of year for the NW (C) and SE (D) study areas using a bin width of 0.5 months and 0.5 km using all cataloged events from January 2005 to December 2014. In the NW (C) the time of year and depth of the M_L ≥4.0 are shown as white triangles. The lower panels show (E and F) the percent above or below the average number of events for each depth interval where warm colors indicate more events and cool colors indicate fewer events. The injection interval depth is shown with a thick dashed line to indicate the depth of large volume injection. The thin dashed black lines are for diffusivities of 0.10, 1.00, and 10.00 m^2 s^{-1} and correspond to the diffusion distance.

(Figure 4.5). The excess events shown in Figure 4.9f for the SE region suggest fluid migration and triggering also extend to depths of 5 km even though seismicity rates there are very low. The SE correlation curves exhibit more variability and probably reflect the true heterogeneity of injection activity not captured by our reservoir partitioning. The main difference between the two regions is that more earthquakes are occurring in the NW compared to the SE and, as Beall and Wright (2010) point out, the occurrence of larger events is concentrated in the NW. We find the $M_L \geq 4.0$ events follow the same general trend of deepening over time after peak injection (Figure 4.9c) and this suggests a more connective fracture network exists in the NW region that extends into the HTZ in order to rupture a $M_L \geq 4.0$ earthquake.

The pattern of the onset and deepening of earthquakes in the field-wide study presented here is consistent with the evolution of seismic activity at individual wells documented in several recent studies. In the NW study area, previously offline, isolated injection wells were targeted in focused studies to monitor microseismic activity in response to injection. Kwiatek et al. (2015) find systematic deepening of seismicity at one well (P9), while seismicity at a second injection well (P29) did not exhibit deepening with time. Thermo-hydro-mechanical models describing microseismicity patterns during an Enhanced Geothermal System (EGS) demonstration experiment for injection well (P32) in the NW region of TG suggest near-field cooling during flash boiling of water to steam, thereby contracting the host rock and producing strains large enough to trigger microseismicity (Jeanne, Rutqvist, Hartline, et al., 2014; Rutqvist et al., 2013). Additionally, Jeanne, Rutqvist, Hartline, et al. (2014) observe the reactivation of sub-vertical fractures near the injection well that allow the propagation of fluids and infer that changes in poroelastic stress are responsible for elevated seismic activity farther from the injection location. Jeanne, Rutqvist, Rinaldi, et al. (2015) estimate a diffusivity of 0.18 $m^2\ s^{-1}$ for the EGS experiment at P32; whereas diffusivity estimates as high as 10.0 $m^2\ s^{-1}$ have been reported for injection well P9 (Martinez-Garzon et al., 2014). We place diffusivity curves on the seasonal excess seismicity (Figure 4.9) and see a pattern consistent with depth migration of seismicity with diffusivities in the range of 0.1 - 1.0 $m^2\ s^{-1}$ in both the NW and SE regions. The higher diffusivity value at P9 could be the result of multiple reactivated faults that are interconnected thereby creating new hydraulic conduits as new areas of production are coming online in the unexploited parts of the NW region.

The vertical movement of fluids requires a network of preexisting pathways that are always present or reactivated during large-volume injection (Barton et al., 1995). The low porosity of the reservoir matrix ($\sim$2%) suggests that hydraulic conductivity is controlled by the large number of variable-sized fractures that are reactivated during injection (Martinez-Garzon et al., 2014). Outcrop samples from TG reveal randomly oriented fractures with mineralization implying relatively low permeability throughout the reservoir (Sammis et al., 1992). However rock coring samples indicate a weak, highly fractured rock matrix suggesting an easily sheared material that could maintain hydraulically conductive conduits (Lockner, Summers, et al., 1982). After decades of injection, the regional maximum horizontal compressive stress orientation still dominates the reservoir, consistent with a normalstrike-slip faulting regime in and surrounding TG (Boyle and Zoback, 2014). This implies that regional tectonic stresses have produced fracture networks that are in a favorable orientation

to reactivate and provide steeply dipping fault planes for fluid transport.

The extent of the depth migration we observe can be described by the conceptual model put forth by Stark (2003) and supported by Beall, Wright, et al. (2010), which suggests earthquakes extending from injection depths to ∼5 km in the HTZ are due to injected water that is not boiled due to the rapid cooling of the surrounding rocks. Excess water is then driven by gravitational flow to greater depths producing the time lag we observe in the seismicity rate curves. We observe the deepening of events in both the NW and SE. The deeper triggered events are a result of both thermoelastic and poroelastic stress as the slow wave of fluid penetrates into the reservoir while decreasing the effective normal stress on preexisting faults. Our exploration of the spatio-temporal evolution of seismicity at TG supports the notion of a field-wide network of hydraulically conductive faults that provides steeply dipping fluid pathways to a few kilometers below the point of injection.

Chapter 5

Seasonal water storage, stress modulation and California seismicity

Published as: Johnson, C.W., Y. Fu, and R. Bürgmann (2017), Seasonal water storage, stress modulation and California seismicity, Science

5.1 Abstract

Establishing what controls the timing of earthquakes is fundamental to understanding the nature of the earthquake cycle and critical to determining time-dependent earthquake hazard. Seasonal loading provides a natural laboratory to explore the crustal response to a quantifiable transient force. In California, water storage deforms the crust as snow and water accumulates during the wet winter months. We used 9 years of global positioning system (GPS) vertical deformation time series to constrain models of monthly hydrospheric loading and the resulting stress changes on fault planes of small earthquakes. The seasonal loading analysis reveals earthquakes occurring more frequently during stress conditions that favor earthquake rupture. We infer that California seismicity rates are modestly modulated by natural hydrological loading cycles.

5.2 Main Text

Changes in water storage and associated surface loads produce elastic deformation of the Earth's crust (Amos et al., 2014; Argus et al., 2014; Borsa et al., 2014). In California the accumulation of winter snowpack in the Sierra Nevada, surface water in lakes and reservoirs, and groundwater in sedimentary basins follow an annual wet and dry cycle. Seasonal vertical and horizontal surface displacements reflect the elastic response of the lithosphere under hydrospheric loads (Chanard et al., 2014; Fu and Freymueller, 2012) and have been linked to modulating large-scale regional seismic activity (Bettinelli et al., 2008; Bollinger et al., 2007; Heki, 2003; Pollitz, Wech, et al., 2013). Seismicity may also be correlated with annual

variations in atmospheric pressure (Gao et al., 2000), surface temperature (Ben-Zion and Allam, 2013), snow accumulation (Heki, 2003), and crustal pore pressure (Hainzl, Ben-Zion, et al., 2013). Seasonal earthquake modulation provides a natural experiment to investigate the earthquake nucleation process by probing the effects of low amplitude stress perturbations on active faults (Beeler and Lockner, 2003).

The hydrosphere in California exhibits a strong annual cycle following the wet and dry seasons. Time series from the continuously operating Plate Boundary Observatory and Bay Area Regional Deformation GPS networks provide dense spatiotemporal resolution of surface loading due to changing water storage (Argus et al., 2014; Borsa et al., 2014; Fu, Argus, et al., 2015). Seasonal vertical and horizontal surface displacement amplitudes in the Sierra Nevada and California Coast Ranges are on the order of >6 mm and ∼5 mm, respectively, and peak late in the year following the dry summer months (Amos et al., 2014). The recent drought conditions in the western U.S. amplify the observed uplift signal as the Earth's crust responds to the loss of mass (Borsa et al., 2014). In the Central Valley and other sedimentary basins the observed seasonal vertical displacements are dominated by the poroelastic response to the head level in the local aquifer system and peak in the spring after the wet winter months (Amos et al., 2014). Stress changes in the crust from the seasonal water loads in the Sierra Nevada, Coast Ranges, and Central Valley may drive the periodic seismicity patterns, thus providing a physical connection to modulated earthquakes.

In central California periodic signals in earthquake catalogs indicate that 12 months and its harmonics are statistically significant and document the modulation of earthquakes at natural loading cycles (Dutilleul et al., 2015). Laboratory fault experiments simulating periodic loading conditions suggest that seismicity should more strongly correlate with the stressing rate if the stressing period exceeds the earthquake nucleation time (Beeler and Lockner, 2003). We expect a weaker correlation with the stress amplitude as the stressing period decreases, indicating a nucleation time exceeding the loading period (Beeler and Lockner, 2003). Numerical simulations predict the strongest correlation should occur at periodic loading near the characteristic nucleation time (Ader, Lapusta, et al., 2014). Earthquake triggering by the short-period daily tides, which are comparable in amplitude to the seasonal loads, suggests a very weak correlation of seismicity rates with tidal stresses (Vidale et al., 1998) except in regions with unusually large tides (Cochran et al., 2004). This supports the notion of earthquake nucleation times longer than the hourly tidal cycles thereby obfuscating a detectable earthquake response to the short-period loading (Ader, Lapusta, et al., 2014; Beeler and Lockner, 2003). We might expect to find a correlation with the seasonal stressing rate if earthquake nucleation times for California faults are less than 1 year. We expect a somewhat weaker correlation with stress amplitude if annual periods are shorter than the nucleation timescale.

Determining the terrestrial water storage is an inverse problem that estimates the change in the surface mass load from the observed vertical deformation (Argus et al., 2014). To avoid large seasonal signals associated with local aquifers we examine the annual vertical displacement amplitudes and remove stations that exhibit uplift in the winter and subsidence in the summer. This includes many stations located in the Central Valley of California

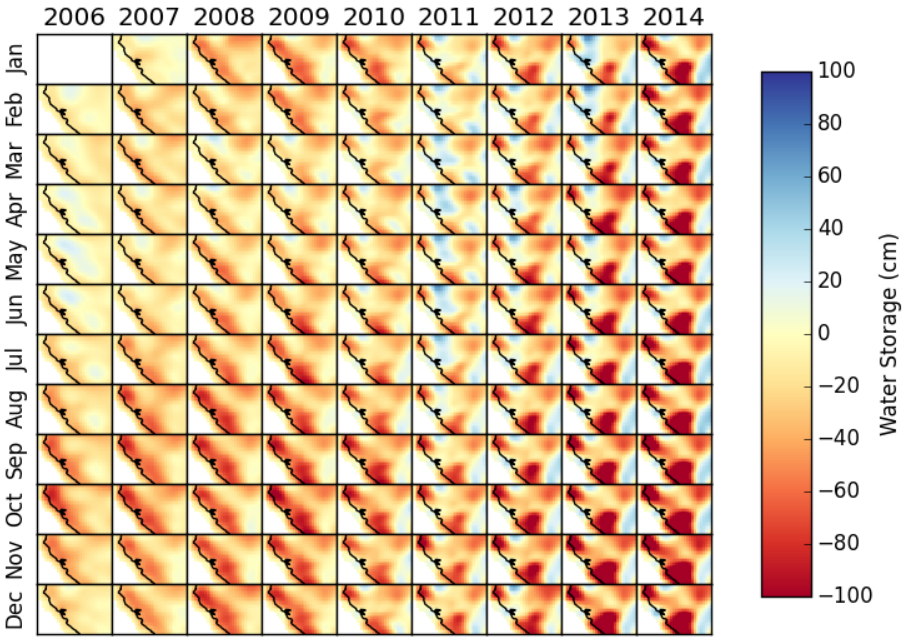

Figure 5.1: Distributed terrestrial water storage in northern California shown as a monthly time series derived from GPS vertical displacements between 2006-2014. The surface load is distributed on a 0.25° x 0.25° grid throughout California and Nevada (125°W - 117°W and 34°N - 42°N).

where large volumes of groundwater are pumped seasonally for agricultural purposes and the GPS peak amplitude is anticorrelated with the Sierra Nevada and Coast Ranges modulation (Amos et al., 2014). The data from the remaining 661 GPS sites are averaged to monthly time series of vertical motions from January 2006 to December 2014. Changes in elevation are mapped to a surface mass load using Greens functions for a spherical gravitating Earth model (Farrell, 1972). The inversion method (Fu, Argus, et al., 2015) estimates surface mass loads on a 0.25°x0.25° grid from 32°N - 42.5°N and 125°W - 115°W (Figure 5.1). Knowing the time-dependent hydrological surface loads we can calculate the monthly stress variations at seismogenic (8 km) depth in a stratified spherical elastic Earth (Pollitz, Wech, et al., 2013). Our focus is seasonal forcing and the long-term trend is removed from the stress time-series.

Our analysis attempts to provide the best hydrologically induced stress-change estimate by selecting the most plausible failure plane for tectonically driven earthquakes. Detailed investigations of focal mechanisms in California reveal a heterogeneous stress field and variations in faulting style (Provost and Houston, 2003; Yang and Hauksson, 2013) that need

to be considered when investigating the effect of applied stress transients on fault activity. Plate boundary deformation in central California involves right-lateral strike-slip faulting along the San Andreas Fault (SAF) system and distributed regional shortening in fold and thrust belts of the Coast Ranges (Page et al., 1998; Titus et al., 2011). To fully capture the complex fault structures in California we examine a declustered (Zhuang, Ogata, et al., 2002) catalog of focal mechanisms (M≥2.0, N= 3,612) in the region 34.5°N - 41.5°N and 124.5°W - 117°W between Jan 2006 and Dec 2014 (Figure 5.2). The focal plane geometry is calculated using first motion data recorded by the Northern California Earthquake Data Center. We exclude events from two geothermal and volcanic centers where variation in the seismicity is mainly a response to large volume fluid injection (Johnson, Totten, et al., 2016) or the upwelling of volcanic fluids (Shelly and Hill, 2011). The focal mechanism nodal plane selection process is non-trivial; while shear-stress changes are identical on the two orthogonal planes, normal stresses generally are not. We address ambiguity in the focal mechanism geometry by selecting the preferred plane using a geometric approach. For the strike-slip mechanisms we select the plane that is best aligned with the SAF (325°) for a geometry consistent with the tectonic environment. For the normal and reverse mechanisms we assume Andersonian geometry and select the plane with a dip angle closer to 30° for reverse events and 60° for normal events. Using the preferred focal geometry, the shear, normal, and Coulomb (μ=0.4) stress is calculated for each earthquake (Figure 5.3).

If slight changes in static stress influence the timing of earthquakes, either promoting or discouraging nucleation, then earthquakes will occur more often during slip encouraging loading conditions. We quantify the percent excess seismicity (N_{Ex}) using 0.5 kPa and 6.0 kPa/yr stress intervals centered on zero for the resolved stress amplitude and stressing rate, respectively. The focal mechanisms are separated into populations of dip-slip containing the reverse, normal, and oblique events (N=2,345) and strike-slip (N=1,344) events (Figure 5.4, 5.5, 5.6). Figure 5.4 shows the results for the shear stress amplitude and rate for the dip-slip and strike-slip events. A positive trend is observed for the shear stress amplitude and the strike-slip events of 22.5 ± 18.2 N_{Ex}/kPa (at 95% confidence) between -1.1 and 1.6 kPa, indicating a seismic response to the peak shear amplitude. The dip-slip events exhibit a response to the shear stressing rate with a positive trend of 12.5 ± 5.9 N_{Ex}/kPa/yr, ranging from -11.8 to 26.7 kPa/yr. Excess events are not observed for the strike-slip events from an increase in the shear stressing rate and similarly the dip-slip events do not show excess seismicity as the shear stress amplitude increases. Interestingly, in all tests performed the excess seismicity is 0% for the near zero stress interval. We repeat the analysis for a series of sensitivity tests and assess our assumptions regarding magnitude cutoff threshold, focal plane ambiguity, and the error in the focal plane solutions (Figure 5.7, 5.8, 5.9). The population of M≥2.3 (N=1,861) events indicate similar results for the strike-slip events (N=762) but no significant trend for the population of dip-slip events (N=1,099) (Figure 5.7). The N_{Ex} values indicate that earthquakes are occurring at different times of the shear stress cycle for different fault types, suggesting that the strike-slip events are mechanically different from the dip-slip population.

The dominant faults in California belong to the northwest-striking SAF system consisting

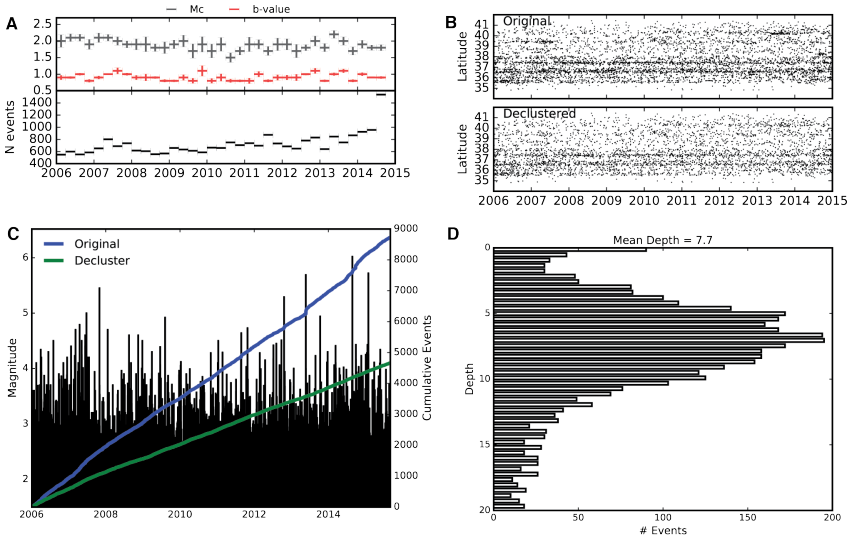

Figure 5.2: Details of the northern California earthquake focal mechanism catalog are shown from 2006-2014. (A) Temporally changing magnitude of completeness (Mc∼2.0) and b-value (∼1.0) using a 0.25-year moving window with no overlap are shown with one standard deviation from 1,000 realizations of the catalog. The horizontal black bar indicates the number of events used in each time step. (B) Plots of time vs. latitude of events for the original and declustered catalog. (C) The magnitude and cumulative number of events for the original and declustered catalog. (D) The depth distribution of the declustered catalog with an average depth of 7.7 km and 54% of the events between 5-10 km.

mostly of right-lateral strike-slip and off-fault dip-slip structures. Excess dip-slip events are resolvable during times of peak stressing rate, which agrees with laboratory and numerical modeling (Ader, Lapusta, et al., 2014; Beeler and Lockner, 2003) if the nucleation time is less than 1 year. This follows a Coulomb failure threshold triggering model that predicts slip to occur with no lag time at the highest stressing rates. However, the population of strike-slip earthquakes indicates excess events when the peak stress amplitude is greatest (Figure 5.4). This could either suggest that the nucleation time is longer for the strike-slip population of events or that there is an increased time lag from the peak stressing rate due to higher tectonic loading rates (Ader, Lapusta, et al., 2014). The strike-slip faults associated with the central SAF system are accumulating strain at rates 8-10 times greater than the dip-slip faults (Titus et al., 2011), consistent with the time-lag scenario.

The results do not indicate a trend with changes in the normal stress, independent of fault type (Figure 5.5, 5.6). The major SAF system of strike-slip faults are postulated to be frictionally weak (Hardebeck and Michael, 2004) and we expected a reduced sensitivity to normal-stress changes. Laboratory measurements, heat flow, and regional principle stress-orientation data all support friction values between 0.1 and 0.2 on the major strike-slip faults

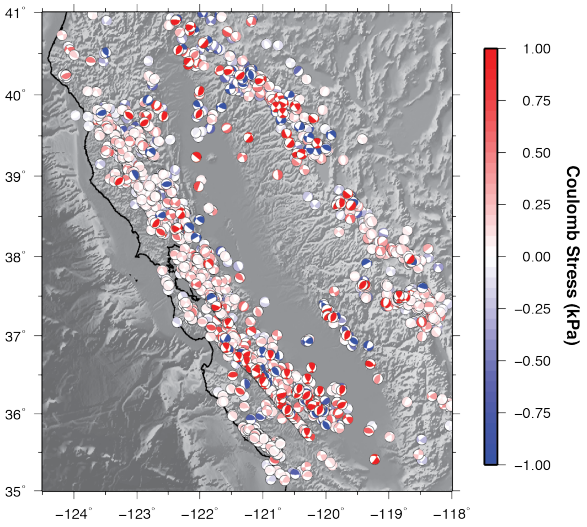

Figure 5.3: Northern California focal mechanism catalog. The hydrological surface loading Coulomb stress change is indicated by the color of the shaded focal mechanism compression quadrant for M≥2.0 events from 2006-2015. Events with a ±0.05 stress change are not shown.

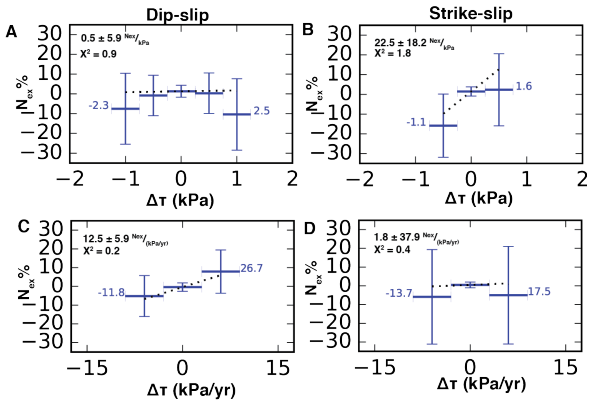

Figure 5.4: Percent excess seismicity for shear stress amplitude and shear stressing rate. (A) Dip-slip events N_{Ex} values for shear stress amplitude. (B) Strike-slip events N_{Ex} values for shear stress amplitude. (C) Dip-slip events N_{Ex} values for shear stressing rate. (D) Strike-slip events N_{Ex} values for shear stressing rate. Bin interval is 0.5 kPa for shear stress amplitude and 6.0 kPa/yr for shear stressing rate. The error bars show the ± 2-standard deviation from bootstrapping. The minimum and maximum stress and stressing rate are shown numerically for the outer bins. The slope of the best fit line is shown in the top left of each panel with the 2-sigma error. The Chi square value is shown for the goodness of fit of the best-fit line.

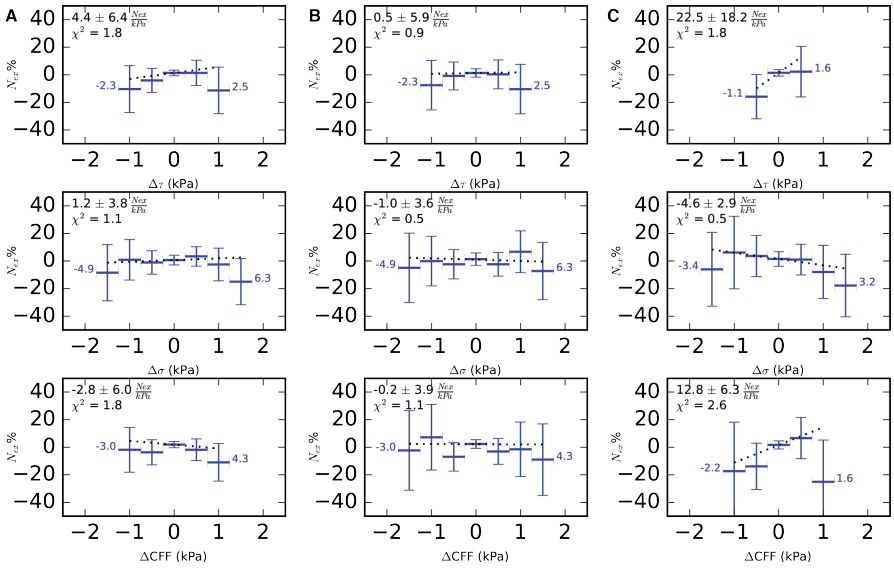

Figure 5.5: Percent excess seismicity for the stress change amplitude for (A) all events, (B) dip-slip and oblique events, and (C) strike-slip events. In each column the top panel is the shear stress, the middle panel is the normal stress, and the bottom panel is the Coulomb stress (μ=0.4). The error bars indicate 2-standard deviation from bootstrapping. The slope and 2-sigma error is shown in the top left of each panel with the associated Chi square value indicating the goodness-of-fit.

(Carpenter et al., 2011; Hardebeck and Michael, 2004). Our results support the weak fault hypothesis for faults in California. However, we cannot assume that all faults in California are inherently weak due to varying geology and the overall maturity of different fault strands. If we perform the analysis and select the fault plane with maximum tension we do find a positive trend with the fault unclamping stress, but cannot say with confidence that the plane selected is the correct failure plane and that a true response to the fault unclamping is occurring.

We calculated seasonal stress time series using the Uniform California Earthquake Rupture Forecast (UCERF3) model geometry (Field et al., 2013), a multi-year community effort that provides earthquake rupture probabilities on California faults. For each fault location we fit a seasonal model to the stress time series and obtain model coefficients to calculate an annual stress cycle. We assumed this represents the monthly stress change for the past 230 years. Figure 5.10 shows the annual peak-to-peak Coulomb stress amplitude on faults throughout northern California (see Figure 5.11 for the corresponding shear, normal, and Coulomb (μ=0.1 and μ=0.7) stresses). The change in Coulomb stress is <1 kPa on most strike-slip faults in the SAF system. The stress cycles on oblique and dip-slip faults in the eastern Coast Ranges and flanking the Sierra Nevada are larger. On many faults the peak slip-encouraging shear and normal stresses are out-of-phase by 30-180 days (Figure 5.12). We assess the timing of historic seismicity from 1781-2012 for M≥5.5 earthquakes (N=137) and

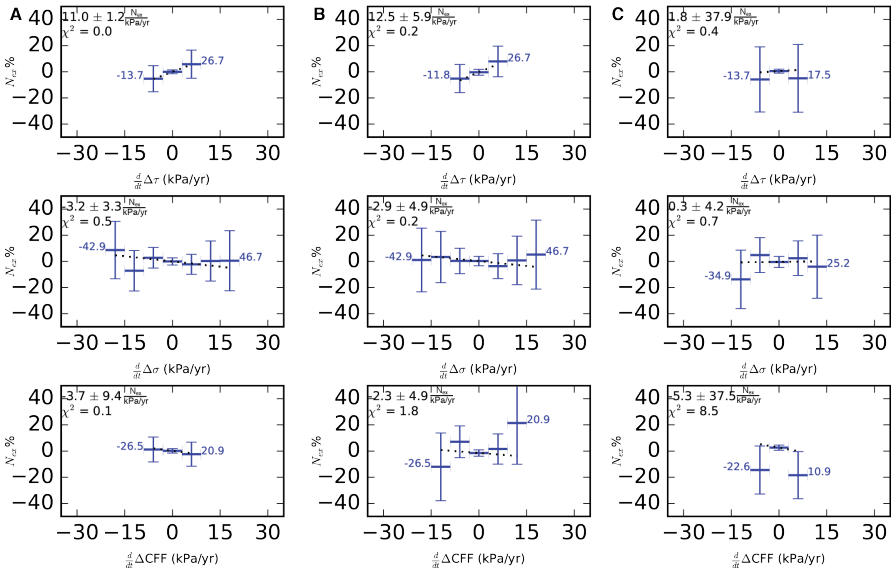

Figure 5.6: Percent excess seismicity for the stressing rate change for (A) all events, (B) dip-slip events, and (C) strike-slip events. In each column the top panel is the shear stress, the middle panel is the normal stress, and the bottom panel is the Coulomb stress (μ=0.4). The error bars indicate 2-standard deviation from bootstrapping. The slope and 2-sigma error is shown in the top left of each panel with the associated Chi square value indicating the goodness-of-fit.

only consider events not identified as foreshock or aftershocks (Felzer, 2013). We assumed the UCERF3 geometry of the nearest fault location is representative of the historic event to evaluate the stress for the month the earthquake occurred. Our simplified treatment of the historical seismicity records suggests that more events occur during times of slip-encouraging failure conditions with a trend of 14.5 ± 9.6 Nex/kPa for the Coulomb stress change (Figure 5.13). The more recent earthquakes occurring during the instrumental era (1932-2012) produce similar results with more events during periods of inferred positive Coulomb seasonal stress changes (Figure 5.14. While their geometry and hydrological stress conditions are less well known, the historic catalogs suggest that large earthquakes might also be triggerable from low-amplitude seasonal stress changes. We infer that annual hydrospheric loading is a contributing factor in the modulation of microseismic earthquakes in California.

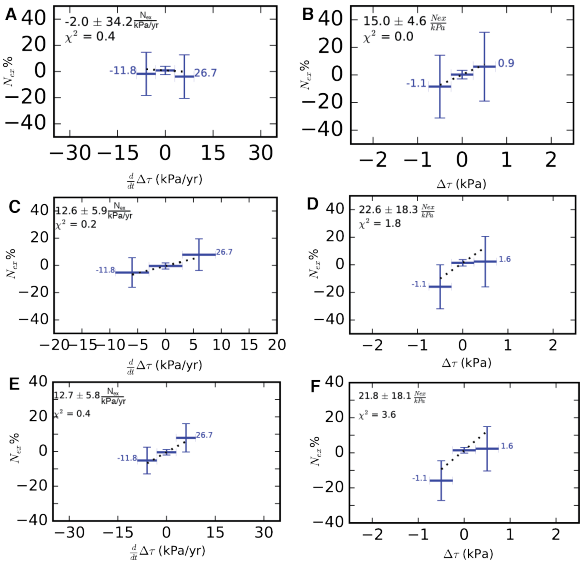

Figure 5.7: Percent excess seismicity is calculated using events with M≥2.3 for the (A) dip-slip events with the shear stressing rate and (B) the strike-slip events with shear stress amplitude. (C) and (D) Excess seismicity calculated using stress on a randomly selected focal plane. (E) and (F) Excess seismicity calculated using stress using both focal planes.

5.3 Materials and Methods

5.3.1 Modeling Terrestrial Water Storage Change and Deformation

The time-varying terrestrial water storage is estimated using vertical GPS deformation as the elastic response due to changes in surface loading. We use the Jet Propulsion Laboratory GPS daily solutions processed with GIPSY software in Point Processing mode (Zumberge et al., 1997). Corrections are applied to the GPS solutions for tropospheric delays (Boehm et al., 2006) and ocean tidal loading (Lyard et al., 2006) using a consistent reference frame (Fu, Freymueller, and van Dam, 2012). The final positions are transformed to the ITRF2008 reference frame. To isolate the contribution of hydrological loading to the vertical displacements we remove the atmospheric loading contribution from the GPS height using data provided by the Global Geophysical Fluid Center (van Dam, 2010; van Dam and Wahr, 1987) as a postprocessing correction to the data time series. We note the seasonal atmospheric loading results in a peak-to-peak shear stress <0.05 kPa and normal stress <0.4 kPa at 8km depth for the same fault location and geometry for the SAF are small in comparison to the hydrological loading signal. We have also explored loading cycles for Earth tide, ocean tides, and temperature changes and find the water cycle is the largest annual load with the exception of a few coastal locations that indicate the ocean loading is significant.

There are a total of 733 GPS stations located in the study area. We are interested in

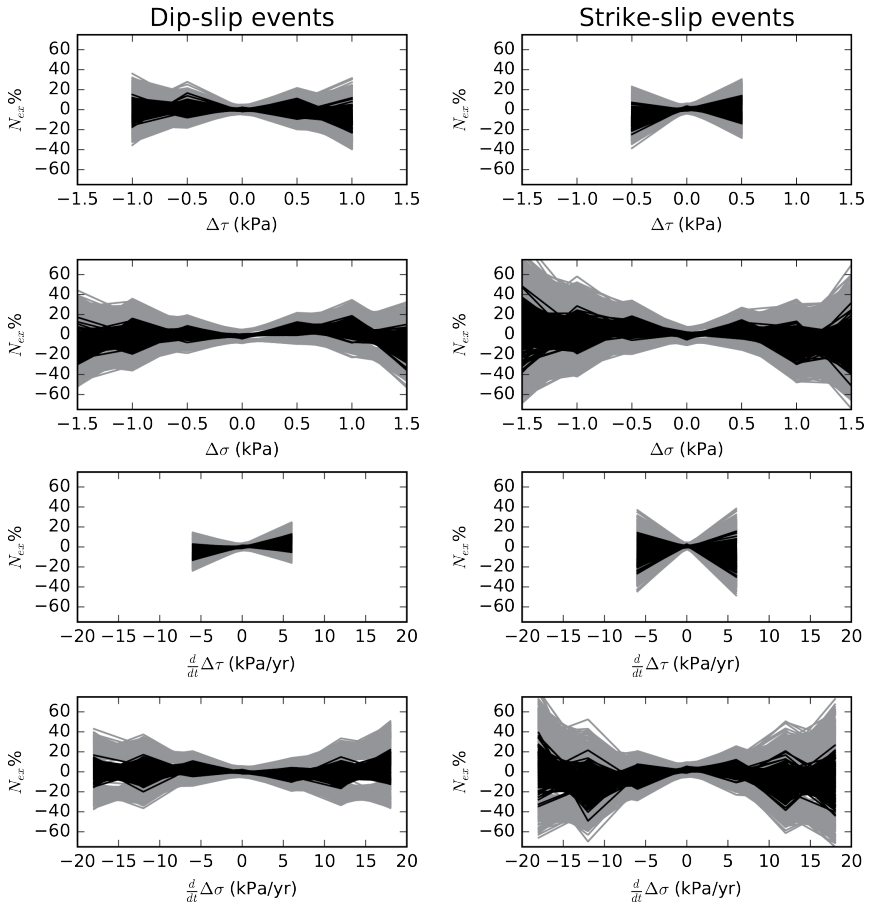

Figure 5.8: Focal mechanism solutions are perturbed with the focal plane error estimates to develop N_{Ex} values for 5,000 Monte Carlo simulations. Black lines are the values across the bins and the grey region is the 95% confidence interval. The simulations are completed for the oblique and dip-slip and the strike-slip earthquake populations. The panels shown are the results for both the peak stress amplitude and peak stressing rate for the shear and normal stress.

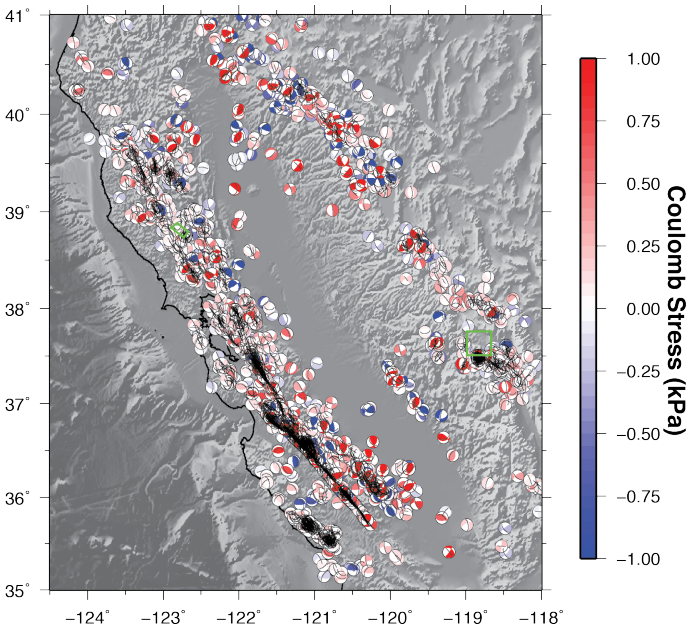

Figure 5.9: The focal mechanisms are shown with the focal plane selected for the analysis highlighted by a black great circle. The strike-slip focal planes are selected based on their alignment with the SAF. The normal events are selected by the plane with a dip angle nearest 60°. The reverse events are selected by the plane with a dip angle nearest 30°. The green rectangles are the Geysers geothermal field and Long Valley volcanic center excluded from the focal mechanism catalog.

retaining the regional-scale hydrological loading displacement signal. To avoid large seasonal signals associated with local aquifer effects we examine the annual amplitudes in the vertical displacement and remove stations that experience uplift in the winter and subsidence in the summer. This includes most stations located in the Central Valley of California where large volumes of groundwater are pumped seasonally for agricultural purposes. This procedure removes 72 stations, and we use the remaining 661 stations for our analysis. The terrestrial water storage is resolved as a time-varying change in water mass on a grid of 0.25° x 0.25° patches. Changes in the GPS derived vertical component are mapped to a surface mass load using Greens functions for a spherical gravitating Earth model (Farrell, 1972). We minimize Equation 5.1 for the vertical elastic response to the monthly water storage variations (Argus et al., 2014; Fu, Argus, et al., 2015), which represents the mass change in the hydrosphere.

$$min\{\, \|W(Gx-b)\|^2 + \beta^2 \|Lx\|^2 \,\} \tag{5.1}$$

The Greens functions (G; m x n matrix; m: number of GPS stations; n: number of patches) associate the load mass change for each patch (x; n x 1 matrix) with the observed

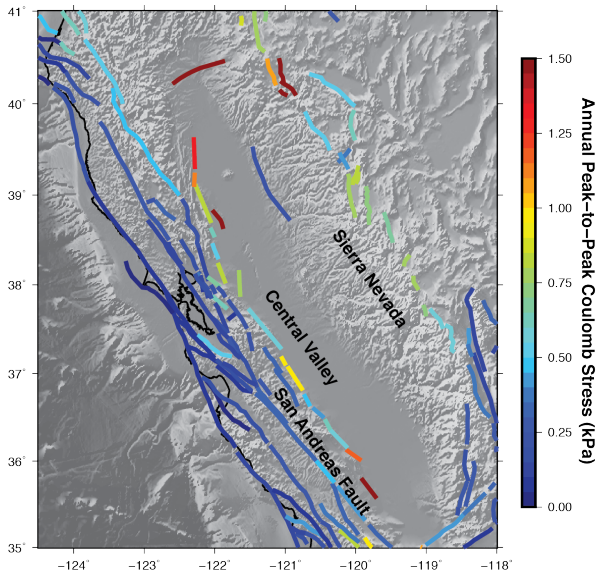

Figure 5.10: Northern California faults in the UCERF3 fault model shown with the annual peak-to-peak Coulomb stress change from hydrological loading.

vertical displacement (b; m x 1 matrix) at each station and are smoothed between patches with a Laplacian operator (L) to suppress large and unrealistic variations between adjacent patches. For the minimization, the residuals are weighted by the factor W and the roughness is scaled by the factor β to adjust the residual misfit. Monthly results are shown in Figure 5.1.

The deformation and stress at the seismogenic depth of 8 km is estimated as a forward calculation from the computed distributed monthly surface loads. The event depth distribution is shown in Figure 5.2 and the catalog events have an average depth of 7.7 km with 54% in the depth range of 5-10 km. The computed stress values do not vary more than 10% over this range. We use a modified version of STATIC1D (Pollitz, 1996) that is adapted for a vertical force at the surface (Pollitz, Wech, et al., 2013) and calculates the equations of static equilibrium for a harmonic degree of 3200 to calculate a 6-compent stress tensor for each location using the preliminary reference Earth model (PREM) (Dziewonski and Anderson, 1981). Due to the non-stationary trend that changes during the wet year of 2011, then followed by the worsening drought starting in 2012 (Robeson, 2015), we assess the annual component by removing a 36-month moving average from the time series and work with the residuals that show the annual peak-to-peak stress change on each fault. We resolve the shear and normal stresses using the strike, dip, and rake from the Uniform California Earthquake Rupture Forecast fault model (Field et al., 2013) and for the focal mechanism geometry.

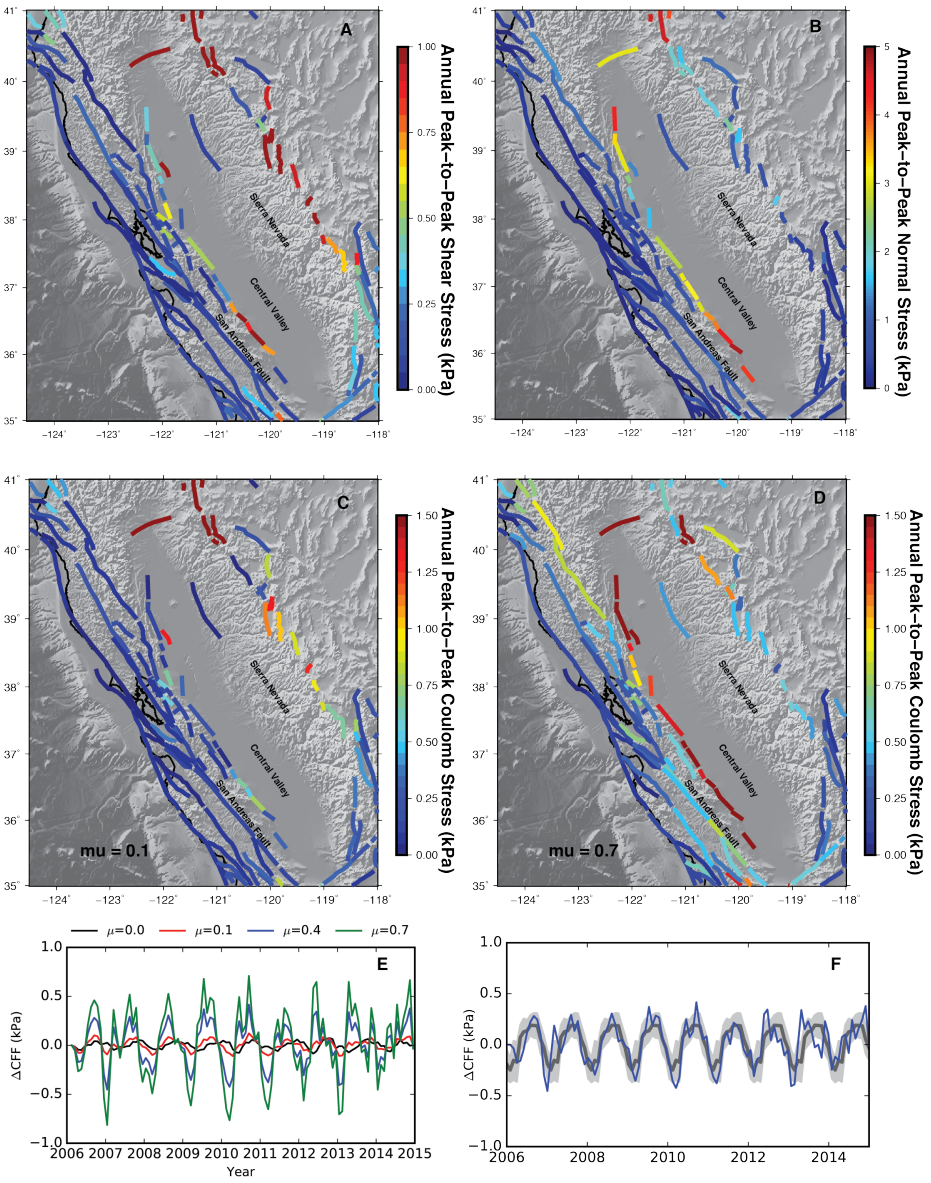

Figure 5.11: Seasonal average peak-to-peak (A) shear and (B) normal stress changes resolved on the UCERF3 California statewide fault model. (C) The Coulomb stress using a friction coefficient of 0.1. (D) The Coulomb stress using a friction coefficient of 0.7. (E) The times series of Coulomb stress changes on the central San Andreas fault for friction coefficients of 0.0, 0.1, 0.4, 0.7. (F) The central San Andreas Fault estimated annual stress (dark gray line) with one standard deviation (grad shading) for the hydrological induced Coulomb (μ=0.4) stress change (blue line).

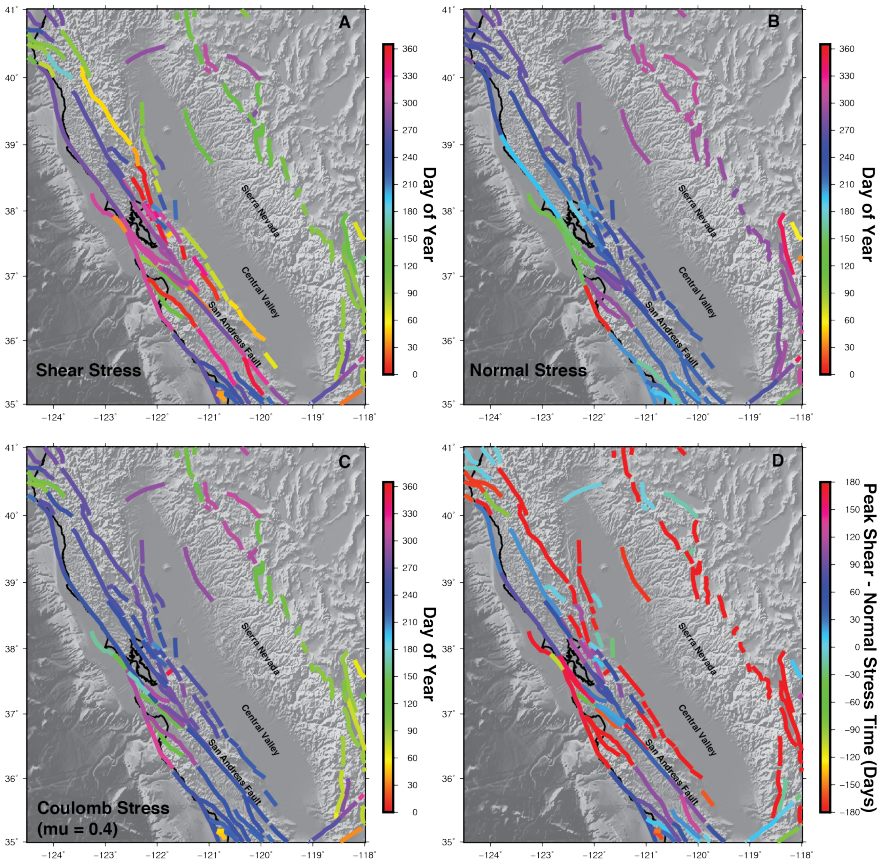

Figure 5.12: The annual timing of peak (A) slip-vector-parallel shear stress, (B) fault-normal tension, and (C) Coulomb stress is shown for northern California faults. The colors of fault segments (color scale on right) indicate the mean phase (day of year) of the peak stress value. (D) The difference in days is shown for the peak time of year for the maximum shear stress with respect to the peak normal stress.

5.3.2 Focal mechanism catalog

Earthquake first motion data is available through the Northern California Earthquake Data Center (`http://ncedc.org`). The focal mechanisms are calculated using the first motion phase arrivals with the FPFIT algorithm (Reasenberg and Oppenheimer, 1985) for M≥1.5 events located onshore between January 2006 and December 2014 for northern and central California at a depth <20 km. We remove focal solutions that contain <25 first motion observations or do not converge during the inversion. Using the remaining events we estimate a temporal magnitude of completeness (M_c) using a 0.25-year moving window with no overlap and estimate the uncertainty with 1000 bootstrap realizations of the magnitude distribution for each time step. The M_c is calculated using the entire-magnitude-range method that utilizes all the catalog seismicity to fit the data above the M_c to a power-law

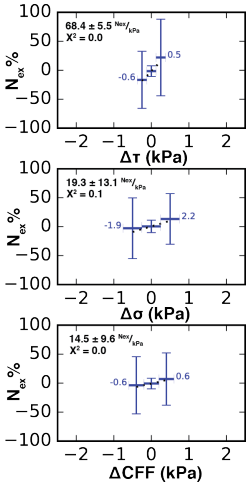

Figure 5.13: Percent excess seismicity from 1781-2012 for M≥5.5 events (N=137) using the UCERF3 historic seismic records and the monthly annual stress estimated from the closest fault model geometry. The error bars show the ± 2-standard deviation from bootstrapping. The minimum and maximum extent of stress values is shown numerically for the outer bins. The slope of the best fit line is shown in the top left of each panel with the 2-sigma error. The Chi square value is shown for the goodness of fit of the best-fit line.

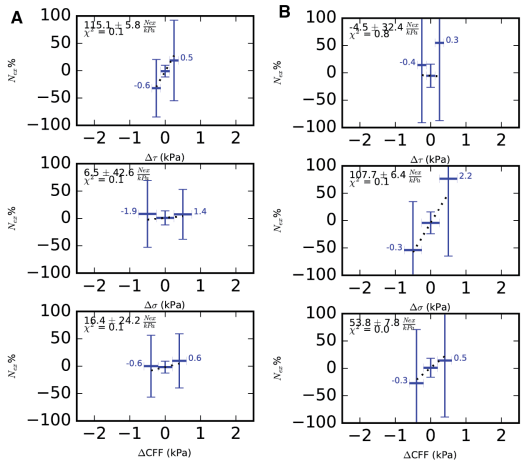

Figure 5.14: The excess seismicity for historic M≥5.5 events in California from 1782-2012. The events are from the UCERF3 earthquake catalog and only independent mainshocks are counted. The stress estimates assume the geometry of the closest UCERF3 fault segment and the average seasonal stress variations during 2006-2014. (A) Contains events between 1782-1931 (N=107) before instrumentation. (B) Contains events during 1932-2012 (N=30) and events were recorded with regional instrumentation.

distribution and below the M_c to a cumulative normal distribution for a range of possible Mc values (Ogata and Katsura, 1993; Woessner and Wiemer, 2005). The process is performed iteratively and the Mc is calculated by estimating the b- and a-value (Aki, 1965; Bender, 1983; Shi and Bolt, 1982) for each M $\geq$ Mi to generate a synthetic frequency magnitude distribution. For each M $\geq$ M_i the frequency distribution is fit to a cumulative normal distribution and the mean (μ) and standard deviation (σ) parameters for this distribution are determined using a non-linear least squares approach. The fitted solution provides the probability of the model for each magnitude below the M_i and above this value the probability is assumed to be 1; the best solution maximizes the log-likelihood for the b, a, μ, and σ values for each M_c (Woessner and Wiemer, 2005).

Our results indicate a M_c ~2.0 for the majority of the study period with error estimates indicating a M_c ~2.3 at a few of the time periods. To retain the largest population of events we use M_c2.0 (N=8,738) for the analysis and calculate all results with a M_c2.5 to ensure the magnitude selection is not biasing the analysis. Aftershock sequences are identified using a spatial-temporal epidemic type aftershock sequence (ETAS) model (Zhuang, Ogata, et al., 2002). The inverted model parameters A=1.0, c=4.35e-3, α=1.08, p=1.01, d=4.4e-6, q=1.88, and γ=0.82 are used to estimate the probability of independence for each catalog event. Establishing the background intensity with an ETAS model allows the use of a non-parametric, stochastic declustering of the aftershocks based on the probability of each event contributing to the background rate (Zhuang, Ogata, et al., 2002). The cumulative number of events for the original and declustered catalog, with the magnitudes, is shown in Figure 5.2. We remove events located in The Geysers geothermal field and in Long Valley Caldera to avoid biasing the results from anthropogenic or volcanic activity (shown in map in Figure 5.9). Additionally, the offshore events in the northwest region of the study area are removed. The declustered catalog contains 3,689 independent events that are used for the analysis.

5.3.3 Seismicity and stress correlation

The seasonal stress change is computed for the time, location and geometry of each earthquake. For every earthquake we develop a stress time-series using the modeled deformation at the location of the event and calculate the stress at the time of failure. We choose a sign convention in which positive shear and normal stress components are slip encouraging and tensile, respectively. To resolve the stress on the failure plane requires knowledge of the fault geometry for each event. Each focal mechanism contains two possible slip planes where the shear stress is equal on each plane but the normal stress can vary in amplitude. Due to this ambiguity, we apply three different methods to select the slip plane; (1) based on the fault geometry, (2) using both possible solutions, and (3) using a random selection procedure with the goal of not introducing a bias to the results. For the geometric selection procedure we classify each event as reverse, strike-slip, normal, or oblique using the plunge of the P-, B-, and T-axis (Zoback, 1992). For the strike-slip mechanisms we select the plane that is best aligned with the SAF (325°) for a geometry consistent with the tectonic environment. For the normal and reverse mechanisms we assume Andersonian geometry and select the plane

with a dip angle closer to 30° for reverse events and 60° for normal events. For the events classified as oblique (20% of the mechanisms) the plane is randomly selected.

The annual peak-to-peak stress resolved on the UCERF3 fault model geometry is calculated by generating a stress time series for each location and fitting an annual and semiannual seasonal model shown in Equation 5.2 to the series. The amplitude is obtained from the model coefficients and are doubled for the peak-to-peak estimate. The peak phase is also obtained from the model coefficients and reported as a day of year.

$$y = a_0 + \sum_{i=1}^{N=2} c_i sin2\pi k_i + d_i cos2\pi k_i \tag{5.2}$$

To evaluate the timing of earthquakes with respect to the seasonal stress change we express the percentage of excess seismicity as N_{Ex} = (N_{Act} - N_{Exp}) / N_{Exp} *100, where N_{Act} is the observed number of events occurring over a given range of stress-change values, N_{Exp} is the expected number of events assuming a uniform random distribution in time, and N_{Ex} is the percent excess number of events (Cochran et al., 2004). To obtain the actual number of events N_{Act} we use the stress at the time of each event using the shear, normal, and Coulomb time-series. To obtain the expected number of events N_{Exp} we assume a uniform sampling of 250 event times for each focal mechanism and resolve the stress and phase at that location using the same stress tensor time-series associated with the focal plane geometry. The distributions of the actual and expected number of events in a given stress interval are determined for each stress component in a 0.5 kPa stress interval within a range that contains 99% of the values and is centered about zero. We choose to center the stress intervals on zero with the central bin containing both positive and negative stress values that are near zero ($\|\text{stress}\| \geq 0.25$ kPa) to avoid overinterpreting the lowest amplitude stress changes. All values beyond the 99% limits are considered in the end-member bins and the total extent of the end-member bins (i.e., the minimum and maximum resolved stresses), is reported in the associated figures. The distribution of the expected numbers is normalized by 250 to account for the uniform sampling of random event times assumed for each focal mechanism stress time series. A N_{Ex} value is calculated for each stress interval and the variance is estimated using 10,000 realizations of the bootstrapped catalog to repeat the analysis and is reported as a two-standard deviation for each stress interval. We fit a variance-weighted regression line to the N_{Ex} values with Equation 5.3 to estimate the coefficients of the linear trend and report the slope with a 2-sigma (95%) error estimate as shown in Equation 5.4. The goodness-of-fit of the trend line is reported as a Chi square statistic calculated using the NEx value and the expected value from the best-fit line as shown in Equation 5.5.

$$min\{\sum_{i=1}^{N}(W_i^2(y_i - (b_0 + b_1 x_i))^2)\} \tag{5.3}$$

$$CI_{95} = \frac{\frac{1}{N-2}\sum(y_j - y_i)^2}{var_i} t_{\frac{\alpha}{2},N-2} \tag{5.4}$$

$$\chi^2 = \frac{1}{N-2}\sum \frac{(y_j - N_{Ex_i})^2}{var_i} \tag{5.5}$$

To estimate the seasonal stress change for the historic seismicity we use the annual model fitted to the stress time series at each location and assume the nearest fault model location is representative of the fault geometry. The distribution for the expected number of events is obtained by assuming the event could have occurred at any time during the annual cycle and using all stress values to generate a distribution. The percent excess seismicity is then computed as previously described.

5.4 Error assessment and sensitivity analysis

The surface load is derived from continuous GPS stations for which advances in processing techniques provide surface displacement measurements with millimeter accuracy. Previous studies (Argus et al., 2014) have compared the GPS derived terrestrial water storage with GRACE (Swenson and Wahr, 2006), the North American Land Data Assimilation System (NLDAS-Noah) (Mitchell et al., 2004), and a composite model containing the soil moisture from the NLDAS-Noah models, the snow water equivalent from the Snow Data Assimilation System (SNODAS) [National Operational Hydrologic Remote Sensing Center, 2004] and surface water in 174 artificial reservoirs from California Data Exchange Center (CDEC, 2014) and find similar estimates among the differing data products. The associated deformation modeling calculates strains that are converted to stress values using constant elastic moduli for the region to report stress values. The uncertainty in these estimates can be attributed to local effects below the spatial resolution of the model and heterogeneous geology containing non-isotropic elastic moduli. The values reported are first order and do not attempt to capture these higher order characteristics of the subsurface deformation.

Systematic and unbiased analysis of the seismicity data is critical to the results presented herein. The assessment and removal of aftershock sequences that potentially bias the results is performed using robust seismicity modeling techniques. Our declustering of the catalog relies on the spatial temporal ETAS model that has been shown to perform well in northern California (Dutilleul et al., 2015). Even though no M≥6.1 earthquakes occurred in the study area during 2006-2014, about 40% of the events are found to be dependent and are removed from the analysis. We test the effect of the cutoff magnitude by repeating the analysis using a M2.3 threshold (Figure 5.7). While the uncertainties and scatter of the obtained N_{Ex} values increases with the decreasing number of events, the results remain consistent for the shear stress amplitude results.

We consider the role of error in the focal solutions (Kilb and Hardebeck, 2006) and test the robustness of our results by removing lower-quality focal mechanisms that have a station distribution ratio <0.50 or if the strike, dip, and rake misfit is $>30°$. The removal of the lower quality events does not alter the conclusions but does increase the uncertainty when using a lower number of events. To evaluate the error into the percent excess values we randomly perturb the strike, dip, and rake of each focal mechanism within the error bounds and repeat the analysis 5,000 times for the oblique and dip-slip, and strike-slip populations (Figure 5.8). The Monte Carlo results indicate a positive trend for the shear stress rate on the dip-slip events and the shear stress amplitude on the strike-slip events. The results are less constrained and the Monte Carlo simulations demonstrate the error in the focal mechanisms can increase the percent excess events for negative stress conditions. Selecting the focal plane using the geometric constraints (Figure 5.9) produces similar results to selecting the plane at random or using both planes in the analysis (Figure 5.7).

Chapter 6

Time dependent seasonal stress changes on California faults

6.1 Abstract

Deformation of the lithosphere arises from multiple natural loading sources that include both surface and body forces. The largest surface loads include near-surface water storage, atmosphere pressure changes, ocean loading, and temperature changes. The solid earth is also deformed by celestial body interactions and variations in the earths rotation rate. We model the deformation in California from 2006 through 2014 for seven different loading sources with annual periods to produce an aggregate stressing history for the study area. Time series analysis indicates the hydrological loads and earth pole-tides are the source of the largest seasonal stress changes. The in-phase nature of the loads constructively interferes and contributes to the largest resolvable stresses for many locations. Our modeling efforts show that all known periodic cycles should be explored when modeling seasonal deformation to fully describe the stress changes. We explore the seasonally induced stresses with respect to the background principal stress orientation and the timing of seismicity. The long-term background stress orientation is resolved using 30 years of focal mechanism data. The results do not indicate a resolvable change to the ambient stress orientation in the crust. Nine years of M$\geq$1.7 seismicity finds the timing of earthquakes correlates with a 5 kPa stress perturbation in the orientation of the maximum compressional background stress direction. The results suggest faults are optimally oriented with the background stress field and at any given time a population of faults is near failure as evident from earthquakes triggered by a 5 kPa stress perturbation.

6.2 Introduction

The state of stress in the earths crust is continuously perturbed as tectonic and transient forces elastically deform the lithosphere. The highest crustal strain rates are located along

actively deforming plate boundaries and generally correlate with high seismicity rates. In addition to tectonic loading, these regions experience transient stresses that originate from multiple non-tectonic loading sources; e.g., tidal oscillations or seasonal surface loading, and contain natural cycles with hourly to annual, or longer, periods. The stress amplitudes of these natural periodic loads can range from 0.01-100 kPa and are generally less than the annual tectonic stress accumulation (∼5 kPa/yr) along plate-boundary fault zones (Parsons, 2006). It has been noted that in some cases these low-amplitude periodic stress perturbations appear to modulate seismicity (Ader and Avouac, 2013; Bettinelli et al., 2008; Bollinger et al., 2007; Christiansen et al., 2007; Cochran et al., 2004; Gao et al., 2000; Hainzl, Ben-Zion, et al., 2013; Heki, 2003; Johnson, Fu, et al., 2017). Investigating the dominant contribution of seasonal forces and the respective timing of earthquakes provides insight into the mechanical properties of the lithosphere and improves our understanding of crustal dynamics.

Earthquakes represent the release of locally accumulated elastic stress in the crust and the spatiotemporal variations of the stress field should influence the timing of earthquake nucleation, if a transient load increases or decreases the regional background stress in an orientation that promotes slip (Freed, 2005; Harris, 1998). The modulation of earthquakes by harmonic forces is thought to be period and amplitude dependent as suggested by laboratory experiments (Beeler and Lockner, 2003; Lockner and Beeler, 1999; Savage and Marone, 2007) and numerical modeling (Ader, Lapusta, et al., 2014). Seasonal loading cycles provide the framework for a natural experiment to extend these observations to the field and characterize the crustal response to periodic stressing. The periodic stresses that arise from multiple natural sources can constructively interfere to amplify the contribution of the transient loading cycle with respect to the background stress field. Conversely, due to the heterogeneous spatial and temporal distribution of these loading cycles the transient stresses may destructively interfere and thus reduce the total stress change. Characterizing the contributing transient loads across a large network of heterogeneous interconnected faults provides insight into the expected response for multiple failure geometries in both space and time.

The natural systems producing the largest periodic deformation of the crust are the hydrosphere, atmosphere, and tidal forces generated by Earths interaction with celestial bodies. The hydrosphere, consisting of surface waters, is circulated around the planet in the atmosphere resulting in the redistribution of surface mass. High precision measurements from the continuously operating global positioning system (GPS) are able to resolve displacements attributed to the annual loading cycles associated with the accumulation and transport of snow and water (Amos et al., 2014; Bevis et al., 2005; Borsa et al., 2014; Chanard et al., 2014; Fu and Freymueller, 2012; Grapenthin et al., 2006; Han, 2017; Johnson, Fu, et al., 2017; Wahr et al., 2013). As air and water circulate the planet, changes in atmosphere pressure are synonymous with mass variations on the surface. Similarly, annual temperature changes are postulated to produce thermoelastic stresses in the shallowest parts of the crust that are of comparable amplitude (Ben-Zion and Allam, 2013). Tidal forces are produced by the gravitational attraction of the moon and sun and variations in the Earths rotation rate that deform the solid Earth and generate the ocean tides (Agnew, 2015; Wahr, 1985). The solid Earth body tides are small and the redistribution of ocean mass generally is the larger source

of deformation (Agnew, 2015). The Earth pole tides produce a body force by the nutation of the Earths axis of rotation relative to the solid Earth and are composed of 12- and 14.24 month Chandler wobble periods (Wahr, 1985). These processes occur simultaneously and all contribute to the continual loading cycles in the crust.

The elastic deformation from these natural loading cycles has been investigated for the suppression or enhancement seismic activity. The loading of the crust from summer monsoons in the Ganges Basin results in a 2-4 kPa stress change in the Himalayan seismic zone where earthquakes occur with greater numbers during the winter (Bettinelli et al., 2008). Similarly, snow accumulation in the western mountain ranges of Japan is estimated to produce a 2-5 kPa stress change during the winter months, and the removal of snow during the spring is thought to contribute to an increase in the number of historical $M \geq 7$ earthquakes (Heki, 2003). In California the annual rain and snow accumulation produces 1-5 kPa stress changes that correlate with increased earthquake numbers at times when stress conditions favor slip on faults (Johnson, Fu, et al., 2017). Seasonal changes in atmospheric pressure of $\sim$2 kPa have also been attributed to the modulation of seismicity in geothermal and volcanic regions (Gao et al., 2000). Short period daily tides can result in a stressing rate greater than the tectonic loading; however, the correlation with seismicity is weak (Vidale et al., 1998) and only observed for the largest tidal stress changes (Cochran et al., 2004) or in particular fluid-rich environments (Rubinstein et al., 2008; Saar and Manga, 2003; Thomas et al., 2009; Tolstoy et al., 2002). Stress cycles produced by the Earth pole tides are 0.1-10 kPa and have been proposed to modulate tremor and slow slip earthquakes in Cascadia and other subduction zones (Shen et al., 2005). These examples demonstrate the complex nature of seasonal loading cycles since many of these processes produce stress changes of varying magnitudes depending on the time of year and location, and all may contribute to modulating seismicity.

In this study, we evaluate seasonal loading cycles from multiple natural sources with an annual period and focus on central and northern California where the modulation of seismicity has previously been reported (Christiansen et al., 2007; Dutilleul et al., 2015; Johnson, Fu, et al., 2017). We examine changes in the background seismicity with respect to the enhancement of the background stress during the loading cycle. Johnson, Fu, et al. (2017) investigated the seismic response to hydrospheric loads in California and found more seismicity occurring when the shear stress increased of $\sim$2kPa on focal mechanism nodal planes of the 2006 - 2014 earthquakes. Here we investigate the contribution of additional seasonal loads and evaluate their enhancement or suppression of stresses from the water loading cycle. For all sources of loading analyzed we examine how they each contribute to the annual deformation and investigate the dynamics of regional seismicity with respect to the loading cycles.

6.3 Annual Periodic Surface Loading and Deformation

We consider the combined contribution of annual periodic loading from hydrospheric, atmosphere, temperature, Earth body tides, Earth pole tides, and ocean tides, and develop a suite of models that describe the time varying stress on active fault structures in central and northern California. The modeling and loading data for each source is described below. A monthly stress time series is calculated for every fault location and geometry in the study. The deformation associated with the loading sources is calculated for the region 34°N - 42°N and 124°W - 116°W from January 2006 - December 2014. The selected time range is consistent with the continuous GPS data that are corrected for the tides, pole-tides, ocean loads, and atmosphere loads and used to estimate the time-dependent water storage (Johnson, Fu, et al., 2017). We report the seasonal stresses as a time series for each load.

6.3.1 Deformation modeling

The sources of loading investigated in this study include atmosphere pressure, Earth pole-tides, Earth tides, non-tidal ocean loading, ocean tidal loading, surface temperature, and water storage. The loading contributions are calculated independently for each source. Two techniques are employed to model the deformation. For the Earth body tides, Earth pole tides, and temperature variations we use theoretical models constrained with data to estimate the deformation. For the atmosphere, non-tidal ocean, ocean tidal, and surface water we utilize a general surface-load model for an elastic spherical layered Earth to estimate the deformation. The loading model is a variant of STATIC1D (Pollitz, 1996) that is modified for a vertical surface force (Pollitz, Wech, et al., 2013). We assume a 1D preliminary reference Earth structure (PREM). All the modeled components of the 3D strain tensor are calculated at 8 km depth that is considered a representative seismogenic depth for the study (Johnson, Fu, et al., 2017). Assuming isotropic elasticity, the stresses are calculated from the modeled deformation using a Poisson ratio of 0.25 and a shear modulus of 30 GPa.

6.3.2 Loading Sources

Atmosphere

The atmospheric loading contribution is obtained from the Global Geophysical Fluid Center (`http://geophy.uni.lu/ncep-loading.html`) (van Dam, 2010) for a global grid derived from the National Center for Environmental Protection reanalysis surface pressure data set. Three dimensional displacements are calculated following van Dam and Wahr (1987). The input loads are estimated on a 0.25° grid for the region 30°N - 44°N and 124°W - 114°W. This the same data applied as a correction to the GPS time-series used in this study and described below. The atmosphere load is discretized for a 0.25° grid and the deformation is calculated using the general loading model.

Earth pole-tides

Changes in the Earths rotation pole axis produce observable surface deformation and theoretical calculations can estimate the horizontal and radial displacements (Wahr, 1985). Earths pole tides involve annual and 14.24-month Chandler wobble periods, which are related to the nutation of Earth's axis of rotation relative to the solid earth. The displacements can be extended to estimate the Earth pole tide induced strains using equations 6.1, 6.2, and 6.3 (Shen et al., 2005).

$$\begin{aligned}\varepsilon_{\theta\theta} = 2l\frac{\Omega_0^2 r}{g}[\sin(2\theta)(m_x\cos(\lambda) + m_y sin(\lambda)) - m_z\cos(2\theta)] - \\ h\frac{\Omega_0^2 r}{2g}[\sin(2\theta)(m_x\cos(\lambda) + m_y sin(\lambda)) - m_z\sin_2(2\theta)]\end{aligned} \tag{6.1}$$

$$\begin{aligned}\varepsilon_{\lambda\lambda} = l\frac{\Omega_0^2 r}{g}[\cot(\theta)(1-\cos(2\theta))(m_x\cos(\lambda) + m_y sin(\lambda)) - m_z\sin(2\theta)] - \\ h\frac{\Omega_0^2 r}{2g}[\sin(2\theta)(m_x\cos(\lambda) + m_y sin(\lambda)) - m_z\sin_2(2\theta)]\end{aligned} \tag{6.2}$$

$$\varepsilon_{\theta\lambda} = -l\frac{\Omega_0^2 r}{g}[\sin(\theta)(m_x\sin(\lambda) + m_y cos(\lambda)) \tag{6.3}$$

Where l and h are the Love numbers (l = 0.085; h = 0.600), Ω is the rotation rate, r is the position radius, g is the gravitational acceleration, λ is the longitude, θ is the colatitude, m_x and m_y are the vectors components of the change in the rotation pole, and m_z is the change in the rotation rate. Note the change in rotation rate is insignificant compared to the variations in the rotation pole (Wahr, 1985). The rotation pole vector components and rotation rate changes are obtained from the International Earth Rotation and Reference System Service (`https://www.iers.org/IERS/EN/DataProducts/EarthOrientationData/eop.html`). The Earth orientation parameters are smoothed values at a 1-day interval and are calculated with respect to the IAU2000A nutation model, which is consistent with IRTF2008. The natural period of the pole-tide induced deformation is $\sim$12 and $\sim$14.2 months.

Earth body tide

The interaction with celestial bodies (namely the moon and sun) induces changes in the gravitational potential and deforms the solid Earth (see Agnew (2015) for a complete review of gravitational tidal forces). The solid Earth tides are the resulting displacements from this interaction and are derived assuming an oceanless Earth. The ocean tidal loading is considered separately when using this framework. Theoretical Earth body tide strains are

calculated using the SPOTL software package (subroutine ertid) (Agnew, 1997) for 1-hour time steps from 2006 to 2014. The largest tidal displacements are observed in the short-period semidiurnal and diurnal tidal constituents. We are interested in the long-period deformation and filter the time series and retain the semiannual and annual component of the tidal signal.

Non-tidal ocean

The non-tidal ocean load results in deformation associated with the changes in the distribution of water mass within the oceans due to Earth tides and atmospheric forcing. The load is equivalent to the change in the pressure exerted on the seafloor by the mass of a column of water directly above. The monthly data product is calculated by the ECCO Project (`http://www.ecco-group.org`) and available through the Jet Propulsion Laboratory (`ftp://podaac-ftp.jpl.nasa.gov/allData/tellus/L3/ecco_obp/`). The ocean model is the same correction applied to the GPS time series. The ocean load is discretized on a 0.25° grid and the deformation is calculated using the general loading model.

Ocean tide

As mentioned for the Earth tides, changes in the gravitational potential deform the Earth. The tidal oscillation of the oceans is dominated by the semidiurnal and diurnal tidal species (Agnew, 2015). The tidal loading prediction used in this study is the TPXO7.2 model calculated on a 0.25° global grid (Egbert and Erofeeva, 2002). The data product is available through the Oregon State University TOPEX/Poseidon Global Inverse Solution (`volkov.oce.orst.edu/tides/global.html`). The ocean model is the same correction applied to the GPS time series. This study is interested in the long period annual tidal changes and the time series are filtered to retain only this component. The deformation is calculated with the general loading model.

Temperature

Temperature variations at the Earth surface induce thermoelastic expansion in competent surface geology that induce strains in the crust (Berger, 1975). Assuming a two-dimension elastic half space, the expected strain value can be quantified using reasonable homogenous elastic parameters (Ben-Zion and Leary, 1986; Tsai, 2011). The largest thermoelastic perturbation is expected near the surface as the thermoelastic strain decays with depth (Tsai, 2011). Temperature data are acquired from the North America Land Data Assimilations System (`ldas.gsfc.nasa.gov/nldas/`). Hourly temperatures are averaged to daily values on a 0.125° grid for the region 34°N - 42°N and 124°W - 116°W from 2006 2014. The thermoelastic strains are estimated using equations 6.4, 6.5, 6.6, 6.7. The strain equations are fully described in Tsai (2011).

$$A(t) = \frac{1+\nu}{1-\nu} k\alpha T_0 \sqrt{\frac{\kappa}{\omega}} e^{-\sqrt{\frac{\omega}{2\kappa}} y_b} \cos(\omega t - \sqrt{\frac{\omega}{2\kappa}} y_b \frac{\pi}{4}) \tag{6.4}$$

$$\varepsilon_{xx}(x, y, t) \approx A(t) \sin(kx) e^{-ky} [2(1-\nu) - ky] \tag{6.5}$$

$$\varepsilon_{yy}(x, y, t) \approx A(t) \sin(kx) e^{-ky} [2\nu - ky] \tag{6.6}$$

$$\varepsilon_{xy}(x, y, t) \approx A(t) \cos(kx) e^{-ky} [1 - ky] \tag{6.7}$$

Where ν is the Poisson ratio (ν=0.25), k is the horizontal wave number (k = $\frac{2\pi}{10^3}$), α is the coefficient of linear thermal expansion ($\alpha = 10^{-05}\ ^\circ C^{-1}$), T_0 is the annual temperature amplitude (half the peak-to-peak temperature), κ is the thermal diffusivity ($\kappa = 10^{-06} \frac{m^2}{s}$), ω is the frequency ($\omega = 2 * 10^{-07} s^{-1}$), and y_b is the incompetent layer thickness at the surface (y_b = 0.5 m). These thermoelastic strains are sufficient to estimate the deformation for our purposes and additional parameter constraints are required to further improve the modeling.

Water Storage

The monthly water storage is estimated using the vertical displacements obtained from the continuous GPS stations in the Plate Boundary Observatory network. The assumptions for this procedure is that water mass is the main source of seasonal displacements on the Earth surface after the removal of additional loading sources from the GPS time series. This study uses the GPS daily solutions processed with GIPSY software in Point Processing mode (Zumberge et al., 1997) by the Jet Propulsion Laboratory and corrected for ocean tidal loading (Lyard et al., 2006) using a consistent reference frame (Fu, Freymueller, and van Dam, 2012). The GPS solutions are transformed into the ITRF2008 reference frame. The atmospheric and ocean loading are sources of seasonal deformation and are removed from the GPS solutions during the postprocessing in order to retain the hydrological loading signal (Argus et al., 2014; Fu, Argus, et al., 2015).

Using 0.25° x 0.25° grid patches for the study area we resolve the time-varying terrestrial water storage as a function of the vertical displacements. The study area contains 773 GPS stations and we remove 72 stations that display a large subsidence signal due to groundwater extraction in agricultural areas. The criteria for removal is a station that exhibits large uplift in the winter and subsidence in the summer, thereby out of phase with the precipitation and following the patterns of anthropogenic pumping. The surface deformation is translated to a mass load using Greens functions for a spherical gravitating Earth model (Farrell, 1972)

assuming an elastic response to water storage variations (Argus et al., 2014; Fu, Argus, et al., 2015), which represents the mass change in the hydrosphere. We solve for the water storage using a weighted least-square smoothed inversion method by minimizing equation 6.8.

$$min\{ \|W(Gx-b)\|^2 + \beta^2 \|Lx\|^2 \} \tag{6.8}$$

Where G is the Greens functions for a m x n matrix (m is the number of GPS stations and n is the number of patches), x is the load mass change, b is the observed displacement, L is the Laplacian smoothing operator, W scales the residuals, and β adjusts the residual misfit. The discretized water mass is used to calculate the deformation with the general loading model. Note this is the same water storage estimate used in Johnson, Fu, et al. (2017) and the trend is removed to asses the seasonal changes in the water loading.

6.3.3 Stress from Loading Sources

The results of the load calculations are presented as individual seasonal stress change contributions from the five largest loads of interest and as a combined seasonal deformation time series. The contributions to the total seasonal stress signal is greatest for the Earth pole tide, atmosphere, temperature, ocean, and surface water load sources. The Earth body tides and non-tidal ocean loading are calculated but not included since the contribution is near zero across the study area. The deformation is resolved as a shear, normal and Coulomb (μ=0.4) stress time-series using the geometry described in the Uniform California Earthquake Rupture Forecast model (Field et al., 2013) that contains major fault structures throughout the region. The stress time-series are shown for three locations spaced along a 300 km transect across central and eastern California with different fault geometries (Figure 6.1 and 6.2) and is repeated for three additional locations and fault orientations located 300 km to the north (Figures 6.3 and 6.4). The faults selected show how the geometry and seasonal stresses vary across the region. This subsample of faults does not represent the full complexity of the varying fault geometry in the study area, but does highlight the spatial heterogeneity of both the faults and loading cycles. To illustrate the relative influence of each loading source, the time series are cross-correlated with the combined total stress time series to show their corresponding amplitude and time lag. A large amplitude with no lag indicates the loading component substantially contributes to the total amplitude. If the amplitude is not in phase, then that loading component is reducing the overall stressing amplitude.

The locations and attitudes shown in Figure 6.1 are the Oceanic Fault near San Simeon, California (a), the central San Andreas Fault near Parkfield, California (b), and the Keough Hot Springs Fault in the Owens Valley Fault zone along the eastern Sierra range front near Bishop, California (c). The Oceanic Fault is an oblique reverse fault. The average peak-to-peak shear and normal stress change is $\sim$0.5 kPa and $\sim$0.8 kPa, respectively (Figure 6.5). The greatest shear stress is from the annual ocean tide, which constitutes the majority of the signal. The largest loading signal in the normal stress component is from the atmosphere

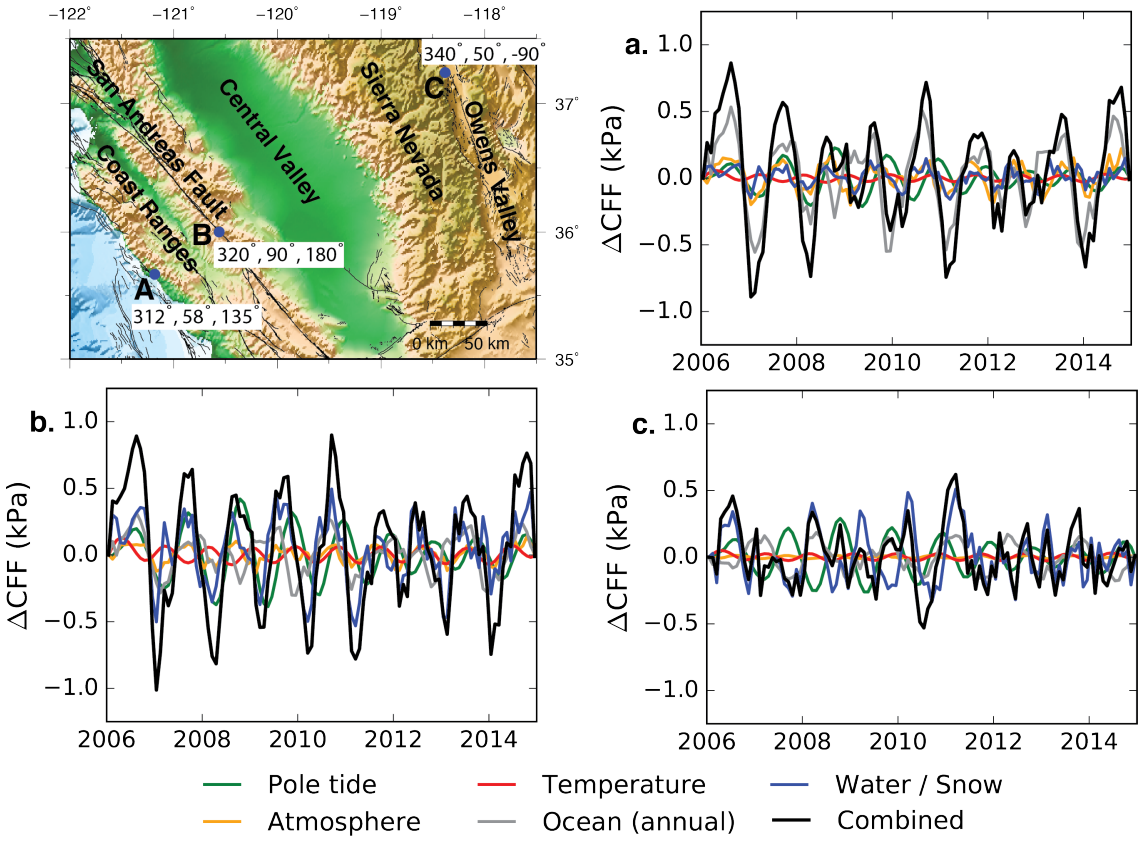

Figure 6.1: The location and the orientation of three faults are listed with the strike, dip, and rake for (a) the Oceanic Fault (-121.18, 35.67) near San Simeon, CA. (b) the central San Andreas Fault (-120.56, 36.00) near Parkfield, CA. (c) the eastern Sierra range front normal fault in Owens Valley (-118.38, 37.34). The corresponding curves show the Coulomb stress change during the study period for the five largest loading sources and the combined total. The locations correspond to Figures 6.5-6.7.

and annual ocean tide. The average annual peak-to-peak Coulomb stress change is ∼0.8 kPa with the largest contributions from the ocean tide.

The central San Andreas Fault is a vertically dipping right-lateral strike-slip fault and is shown near the transition from the locked to creeping section of the fault. The average peak-to-peak shear- and normal-stress change is ∼0.4 kPa and ∼1.9 kPa, respectively (Figure 6.6). The largest shear-stress loading component is the annual component of the pole tide (∼12 and ∼14.2 month period). The largest load for the normal stress change is the water storage, which accounts for >80 % of the combined stress curve (Figure 6.6). The peak-to-peak Coulomb stress is ∼0.9 kPa and a 2-month time lag is observed for the pole tide stressing contribution.

In the eastern California shear zone is the Owens Valley Fault zone in the foothills of

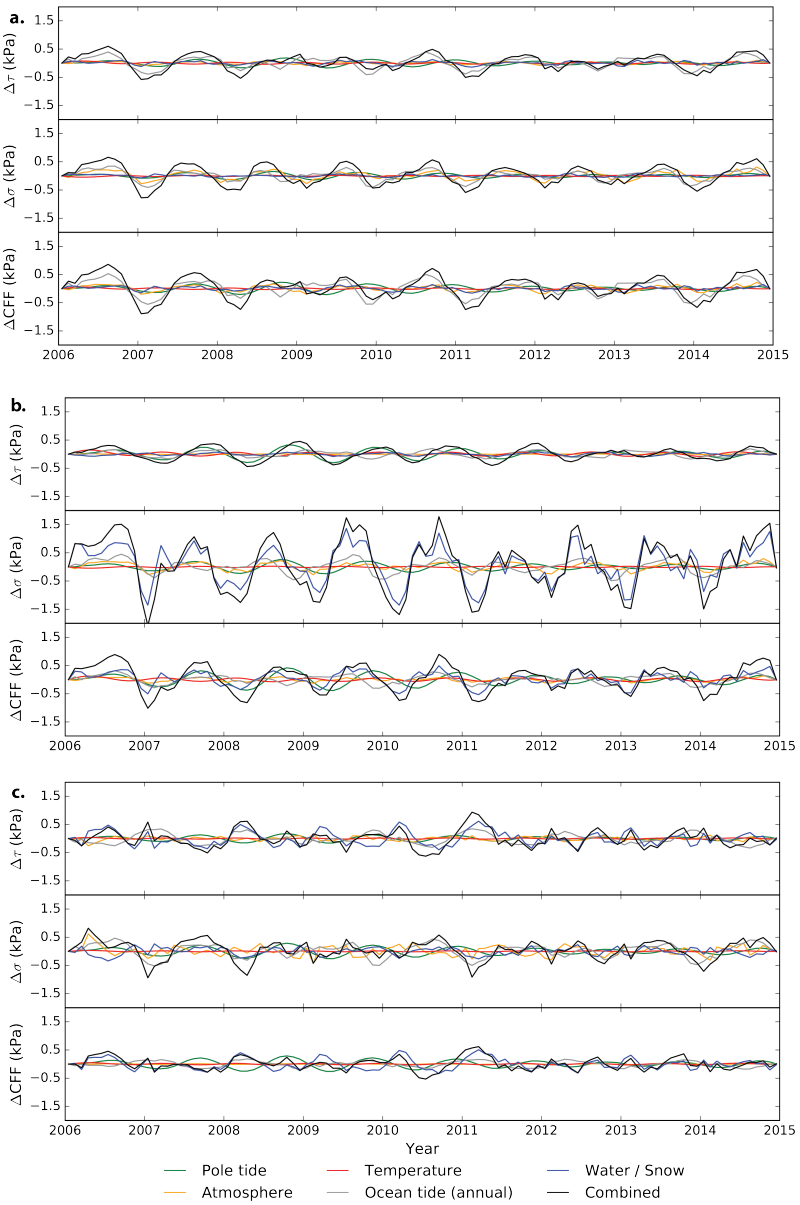

Figure 6.2: The shear, normal, and Coulomb stress time series for (a) the Oceanic Fault (-121.18, 35.67) near San Simeon, CA. (b) the central San Andreas Fault (-120.56, 36.00) near Parkfield, CA. (c) the eastern Sierra range front normal fault in Owens Valley (-118.38, 37.34). These are the same locations as in Figure 6.1 in the main text.

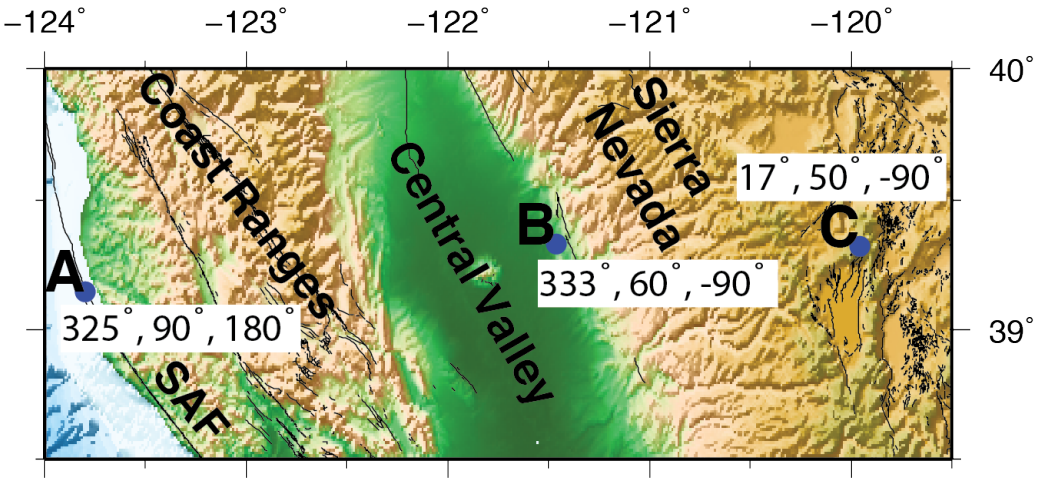

Figure 6.3: The locations as blue dots and the orientation of each fault is listed with the strike, dip, and rake. (A) the San Andreas Fault (-123.80, 39.15) near Bodega Bay, CA. (B). the Foothill Fault system (-121.46, 39.53) in the western Sierra range front. (C) the North Tahoe Fault (-119.96, 39.32) near Lake Tahoe, CA.

the eastern Sierra Nevada that contains normal and strike-slip fault segments. The Keough Hot Springs Fault is a normal fault in the range front. The average peak-to-peak shear and normal stress is ∼0.4 kPa and ∼0.6 kPa, respectively (Figure 6.7). The shear stress change is modulated by the ocean tide and seasonal water storage. Interestingly, the largest contribution to the normal stress changes is the annual ocean tide. The peak-to-peak Coulomb stress change is ∼0.2 kPa. The shear and normal stress time series are out of phase and the resulting Coulomb stress amplitude is minimal (Figure 6.7).

In the northern region of the study area the locations are the San Andreas Fault near Bodega Bay, California, the Foothill Fault System east of Sacramento, California in the Sierra Nevada western range front, and the North Tahoe Fault near Truckee, California (Figure 6.3). The northern San Andreas Fault is a vertically dipping right lateral strike-slip fault located along the coastline and offshore for much of northern California. The peak-to-peak shear and normal stress change is ∼1.8 kPa and ∼2.9 kPa, respectively (Figure 6.4). The largest stress is from the annual ocean tidal loading (Figure 6.8). The peak-to-peak Coulomb stress change is ∼3.0 kPa. The Foothills Fault system consists of a series of normal faults in the western foothills of the Sierra Nevada. The peak-to-peak shear and normal stress change is ∼0.2 kPa and ∼1.3 kPa, respectively (Figure 6.4). The fault system is within close proximity to the large hydrological loading associated with the Sierra Nevada that modulates the normal stress component, but the fault geometry produces a modulated stress in the shear stress component that is dominated by the ocean tides. None of the loading contributions indicate a significant shear stress change and the Coulomb stress indicates ∼0.4 kPa (Figure 6.9). The North Tahoe Fault system is a normal fault in the Sierra Nevada along the Tahoe range front. The peak-to-peak shear and normal stress change is ∼1.5 kPa and ∼2.1 kPa,

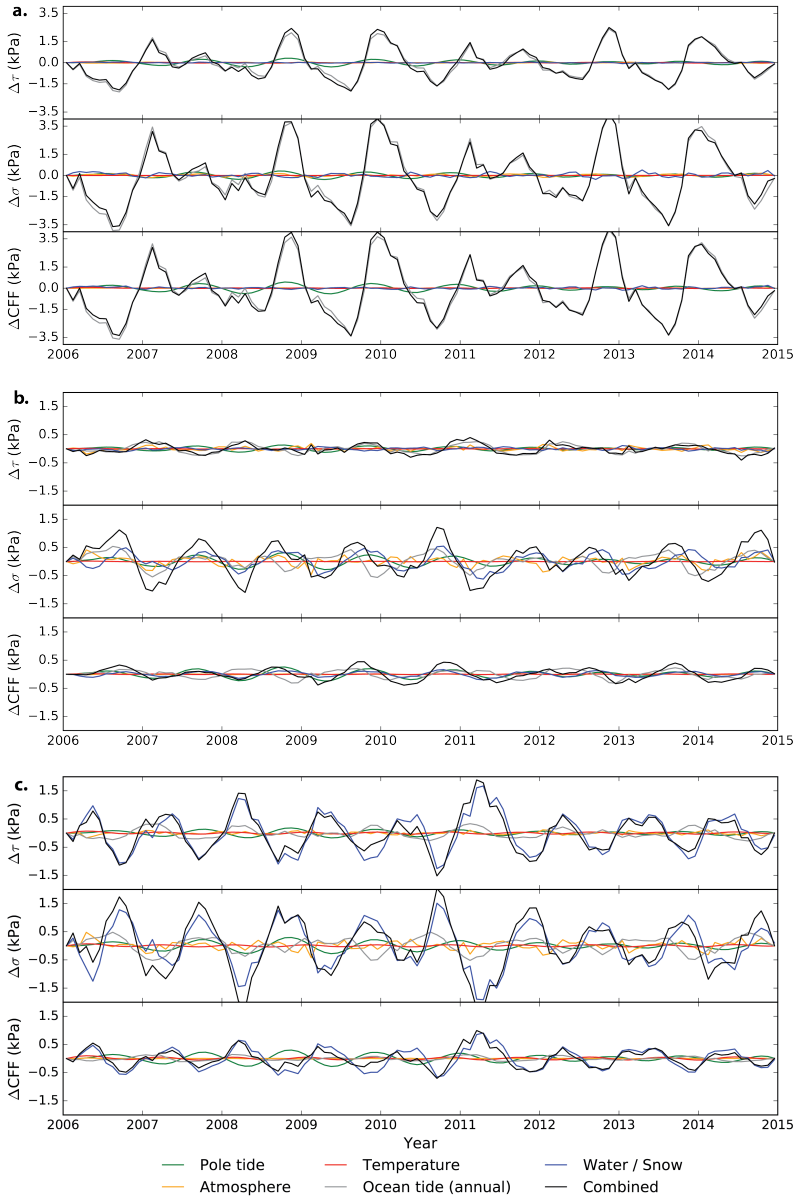

Figure 6.4: The deformation time series for the locations shown in Figure 6.3. (a) San Andreas Fault near Bodega Bay, CA, (b) Foothills fault system, and (c) the North Tahoe Fault. At each location the shear, normal, and Coulomb stress is calculated for each loading component and shown as an individual curve.

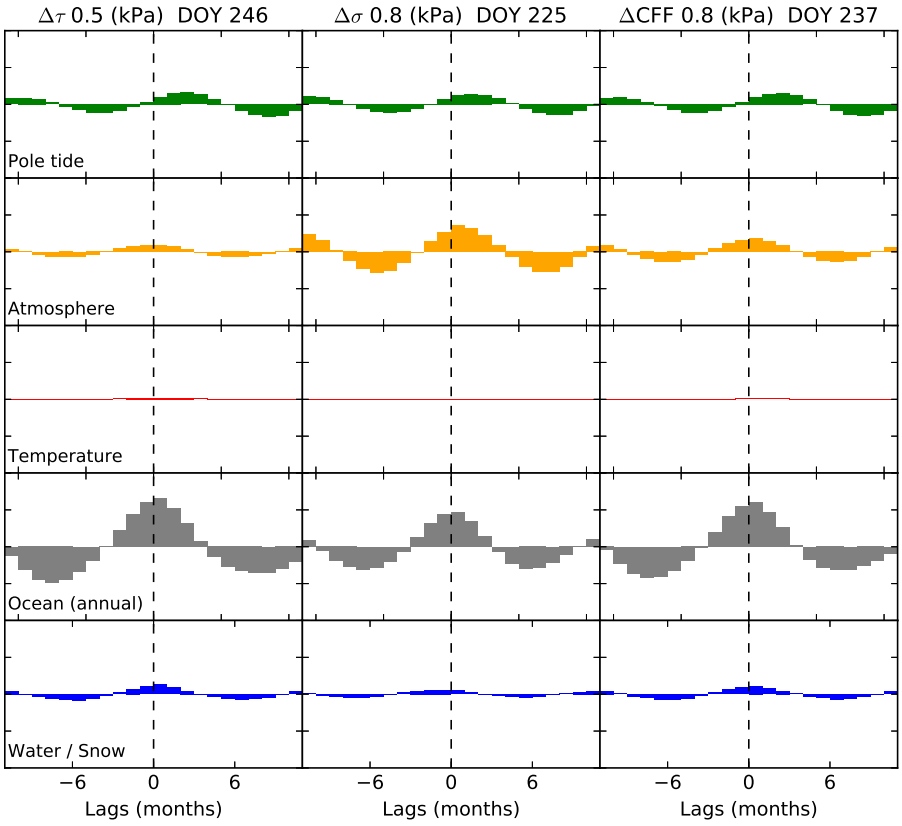

Figure 6.5: Seasonal stress contribution for the Oceanic Fault for the shear, normal, and Coulomb stress labeled on the top of each column with the peak-to-peak stress and the day of year (DOY) of the peak combined total stress. The contributions of the individual seasonal stress time series are shown as the normalized cross correlation with the combined total stress time series. The vertical axis is the relative amplitude from -1.0 to 1.0 with respect to the total stress time series and the horizontal axis shows the ±12 month time lags. Shown are the results for the Earth pole tide, atmosphere, temperature, annual ocean tide, and near surface water storage as labeled in each left-side panel. Not included are the Earth body tides and non-tidal ocean which all contain values near zero (< 0.08 kPa).

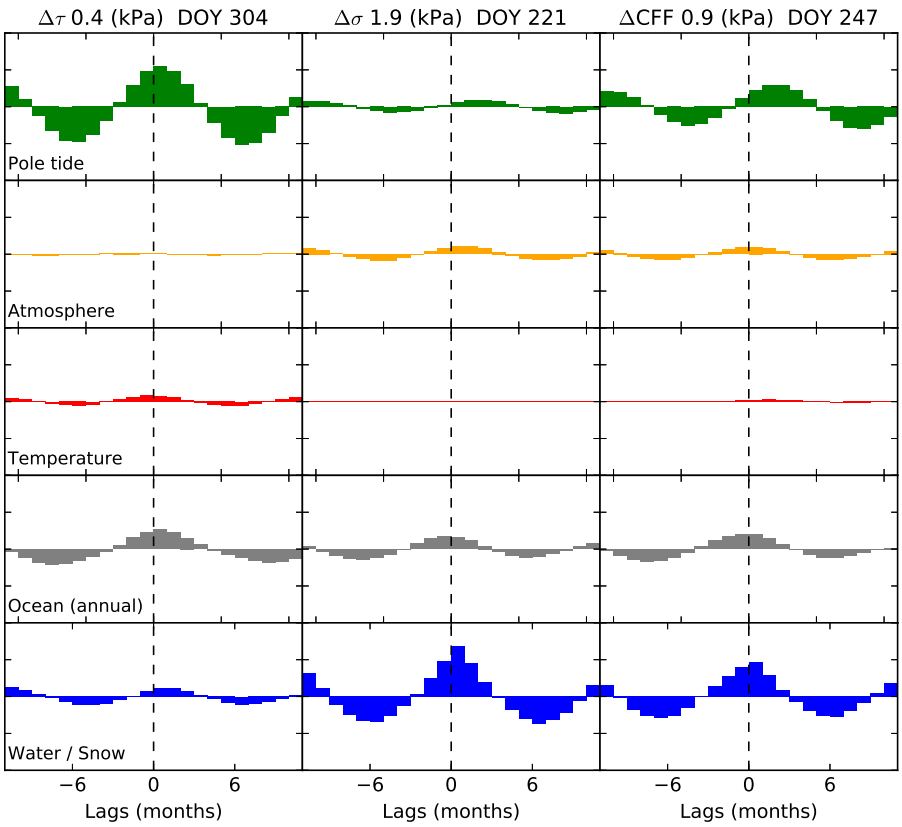

Figure 6.6: Seasonal stress contribution for the Parkfield section of the central San Andreas Fault for the shear (left), normal (center), and Coulomb stress (right). Details are the same as Figure 6.5.

respectively (Figure 6.4). The greatest stress contribution for both the shear and normal components is from the water storage, notably snow accumulation throughout the winter months. The shear and normal stress are 180° out of phase and the resulting peak-to-peak Coulomb stress change is ∼0.7 kPa (Figure 6.10).

As indicated by the 6 locations documented, the regional stress change on the major fault systems is heterogeneous and the dominant loading source varies spatially and temporally. Figure 6.11 shows the average annual peak-to-peak Coulomb stress (μ=0.4) change with the day-of-year for the maximum stress change. Along the Coast range the maximum stress change is between 0.75 - 2.0 kPa and generally is at a maximum in late in the year during September and October. A 6 month difference is observed for many faults in the Sierra Nevada that have a peak-to-peak stress change $<$ 1.0 kPa and is greatest during the early summer months. As shown in Figures 6.5-6.7 the combined seasonal stress change can be dominated by one or two sources.

For each fault, the loading source that contributes the greatest to the seasonal Coulomb

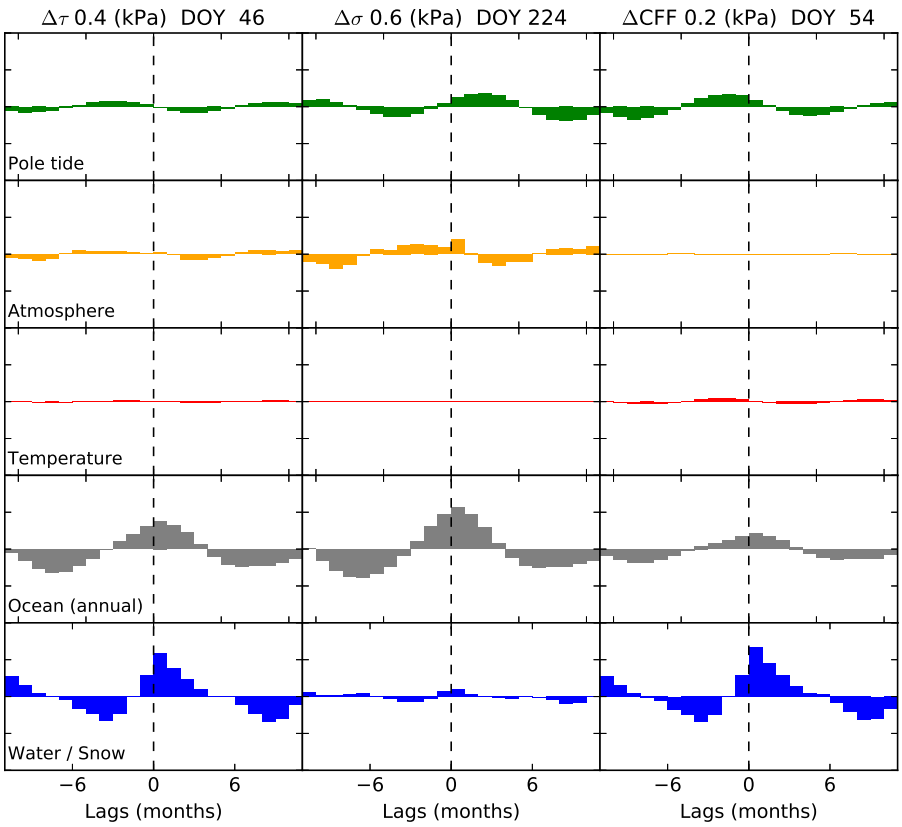

Figure 6.7: Seasonal stress contribution for the Keough Hot Springs Fault in the Owens Valley Fault zone for the shear (left), normal (center), and Coulomb stress (right). Details are the same as Figure 6.5.

stress change is reported (Figure 6.12). Two loading sources are observed to contribute the greatest to the seasonal stress cycle. In many locations surrounding the Sierra Nevada the hydrological loading is the greatest source of loading. As distance from the mountain range increases the Earth pole-tide is the largest source of seasonal stress. Faults located along the coast are mostly modulated by the ocean loading cycle. Loading induced by atmosphere pressure and temperature changes contribute the least to the seasonal stress changes.

6.4 Background Stress and the Regional Seismicity Seasonal Response

To evaluate the degree to which seasonal stress changes affect seismicity we quantify by how much the background state of stress is enhanced by seasonal perturbations and estimate the variation of seismicity rates as a function of those stresses. The timing, location,

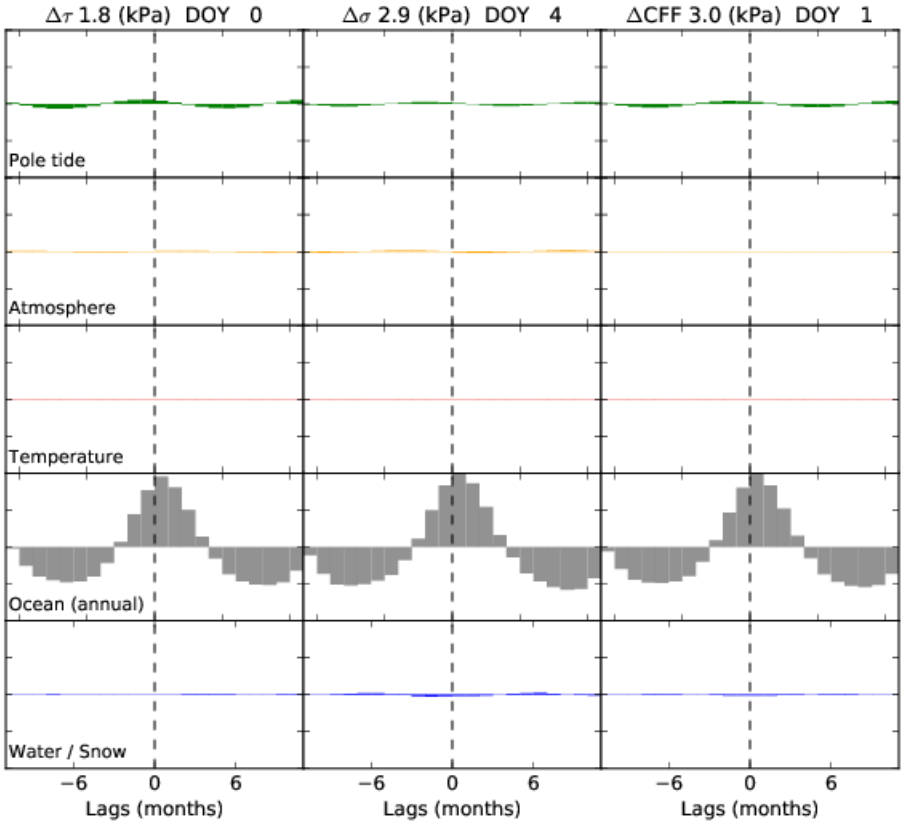

Figure 6.8: Seasonal stress contribution for the San Andreas Fault near Bodega Bay, CA for the shear, normal, and Coulomb stress labeled on the top of each column with the peak-to-peak stress and the day of year (DOY) of the peak combined total stress. The contributions of the individual seasonal stress time series are shown as the normalized cross correlation with the combined total stress time series. The vertical axis is the relative amplitude from -1.0 to 1.0 with respect to the total stress time series and the horizontal axis shows the ±12 month time lags. Shown are the results for the Earth pole tide, atmosphere, temperature, annual ocean tide, and near surface water storage as labeled in each left-side panel. Not included are the Earth body tides and non-tidal ocean which all contain values near zero ($<$ 0.08 kPa).

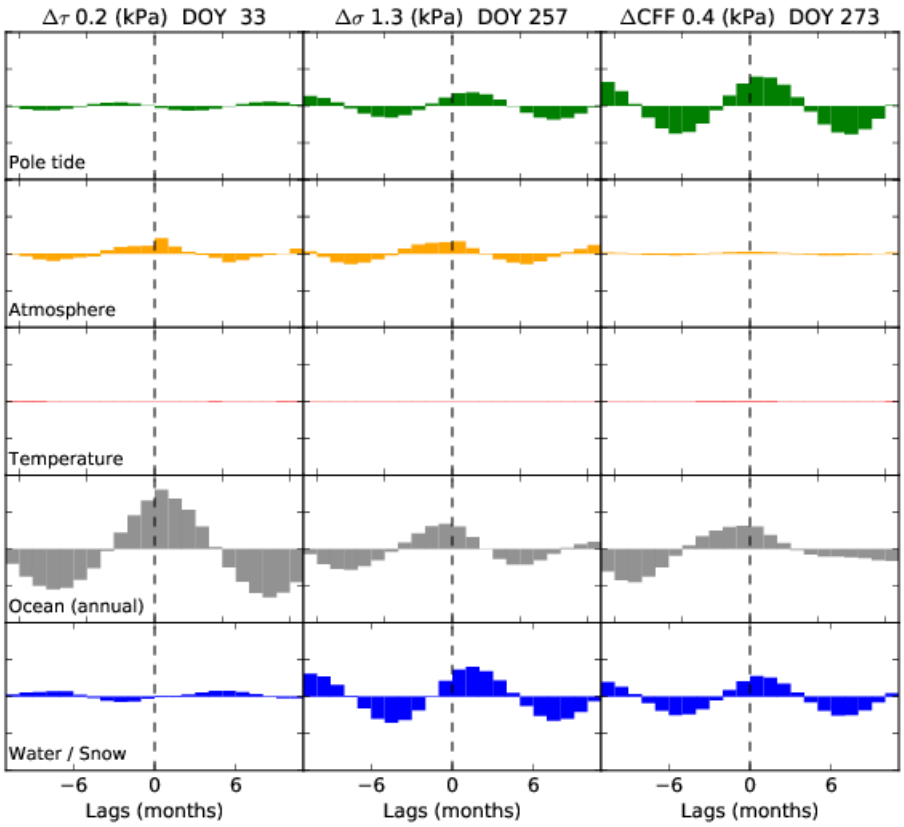

Figure 6.9: Seasonal stress contribution for the Foothills fault system for the shear (left), normal (center), and Coulomb stress (right). Details are the same as Figure 6.8.

and rupture orientation of an earthquake each provide insight into the state of stress in the crust and the possible response to additional transient forces. We utilize hypocentral seismicity catalogs to develop earthquake rate time series and earthquake focal mechanisms to estimate the orientation of the regional background stress field. The data contained in the two catalogs are inherently different since detecting and locating an earthquake does not guarantee that enough information is also recorded to calculate a robust focal mechanism solution. Therefore, we treat the catalogs as independent and apply different criteria when analyzing the seismicity. Detailed in this section is the treatment of the seismicity records to obtain earthquake rates

6.4.1 Seismicity Catalogs

Seismicity Hypocentral Catalog

To avoid biases in the analysis, we seek a seismicity catalog that is complete above a selected magnitude threshold and is composed independent events. Seismicity data is

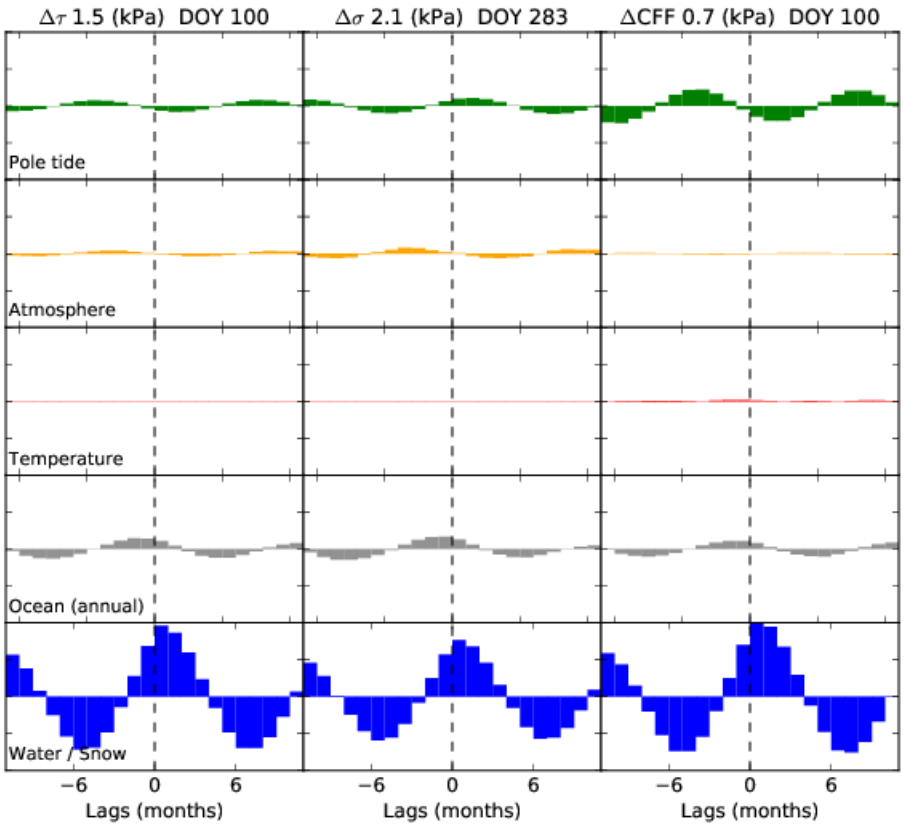

Figure 6.10: Seasonal stress contribution for the Foothills fault system for the shear (left), normal (center), and Coulomb stress (right). Details are the same as Figure 6.8.

obtained from the ANSS composite catalog for the period of January 2006 to December 2014 and is spatially limited to the region 34.5N - 41.5N and 125W - 117W. We exclude earthquakes located in Coso geothermal field, Geysers geothermal field, and Long Valley Caldera and focus our study on non-volcanic seismicity located on or near active faults. The magnitude of completeness (M_c) is calculated using a non-overlapping 0.25-year moving window and 500 bootstrap iterations to estimate the uncertainty. We calculate the b- and a-value for each M $\geq M_i$ (Aki, 1965; Bender, 1983; Shi and Bolt, 1982) and fit the data to a synthetic distribution for the goodness of fit test (Wiemer and Wyss, 2000) to determine the M_c for each time step. We find M_c1.7 and a b-value of $\sim$1.0 for the period of interest in this study (Figure 6.13). Aftershock sequences are declustered using the spatial-temporal Epidemic Type Aftershock Sequence model (ETAS) to estimate the probability that each earthquake is independent from the remaining catalog with the inverted model parameters mu=1.0, A=0.95, c = 0.003, alpha=1.15, p=1.02, d=7e-05, q=1.8, gamma=0.49 (Zhuang, Ogata, et al., 2002). The cumulative number of events and the spatial-temporal distribution of clusters is shown in Figure 6.13. The declustered hypocentral seismicity is used to calculate

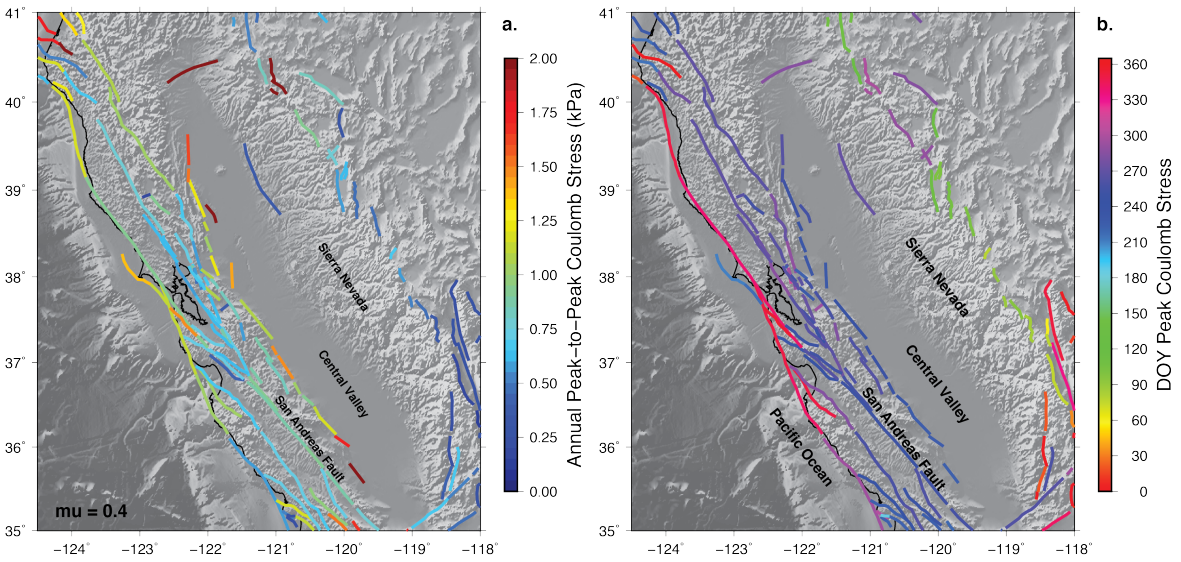

Figure 6.11: The average annual peak-to-peak Coulomb stress (μ=0.4) change is shown is on the UCERF3 fault model geometry with (b) the day of year of the peak stress.

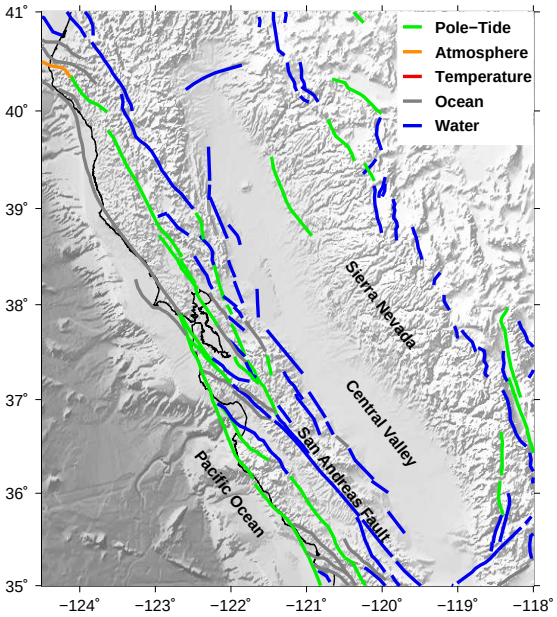

Figure 6.12: The regional faults are color coded by the loading source that contribute the largest in-phase amplitude to the total seasonal Coulomb stress change.

earthquake rates at specific locations using a moving average.

Focal Mechanism Catalog

Earthquake focal mechanisms are used to estimate the regional background stress field. Efforts are taken to ensure the highest quality focal mechanisms are selected for the study. First motion data recorded by the Berkeley Seismological Laboratory are available through the Northern California Earthquake Data Center (`http://ncedc.org`). Focal mechanisms with M≥1.5 between January 1984 and December 2015 are calculated with the FPFIT algorithm (Reasenberg and Oppenheimer, 1985). Solutions that do not converge are removed. If multiple solutions are obtained for an event the mechanism with the highest station distribution ratio (sdist) is retained to use the mechanism with less first motions on a nodal plane. The full catalog with duplicate solutions removed contains 69,296 events. Events located in The Geysers geothermal field and Long Valley Caldera are removed from the analysis to avoid energy production and volcanic activity related events. Events shallower than 2 km and deeper than 20 km are also removed. The final catalog contains 50,716 M≥1.5 events. The magnitude of completeness, cumulative number of events, and the clusters through time are shown in Figure 6.14. The results indicate a magnitude of completeness between M2.0 - M2.5 in the early years of the catalog. The increased detection of events following 2001 coincides with funding for the implementation of the ANNS (`http://earthquake.usgs.gov/monitoring/anss/milestones.php`) and is primarily due to the initiation of a network wide conversion from analog to 24-bit digital telemetry for collocated first motion and strong motion sensors that continues to the present (personal comm. David Oppenheimer, U.S. Geologic Survey, Menlo Park, CA). The advantage of the digital telemetry is an increase in the dynamic range, which allows the detection of lower magnitude events and is shown with the decreasing M_c to M1.5 - M2.0 in the later years of the catalog (Figure 6.14). This is also observed in the cumulative number of events and the clusters in time, which both indicate a rate increase in early 2000's. Here we use events below the calculated M_c since the focal mechanism catalog is not used to calculate a seismicity rate and only the focal plane and location is of interest.

To address seismicity clusters in the catalog the nearest neighbor distance (η) is calculated using equation 6.9, 6.10, 6.11, to determine the parent daughter relationship between each event (Zaliapin and Ben-Zion, 2013). We calculate the scalar nearest-neighbor distance from the rescaled temporal and spatial distances between event pairs, T_{ij} and R_{ij}.

$$\eta_{ij} = T_{ij} R_{ij} \tag{6.9}$$

$$T_{ij} = t_{ij} 10^{-qbm_i} \tag{6.10}$$

$$R_{ij} = r_{ij}^{d_f} 10^{-(1-q)bm_i} \tag{6.11}$$

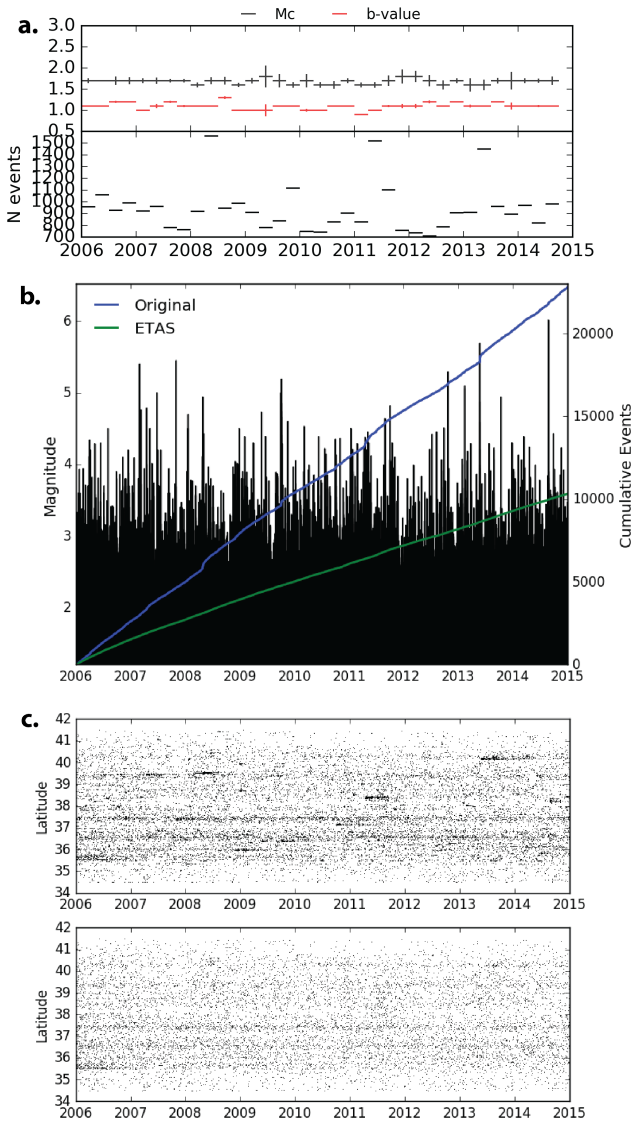

Figure 6.13: ANSS catalog details. (A) Magnitude of completeness and b-value calculated with a 0.25-year non-overlapping moving window. Upper panel shows the calculated value with 1-sigma uncertainty. Lower panel is the number of events per time step to perform calculation. (B) The cumulative number of events from 2006 to 2015 for the M≥1.7 original and ETAS spatial-temporal declustered catalog with the event magnitude shown in black. (C) The original and declustered catalog shown as time vs latitude for the original and declustered catalog.

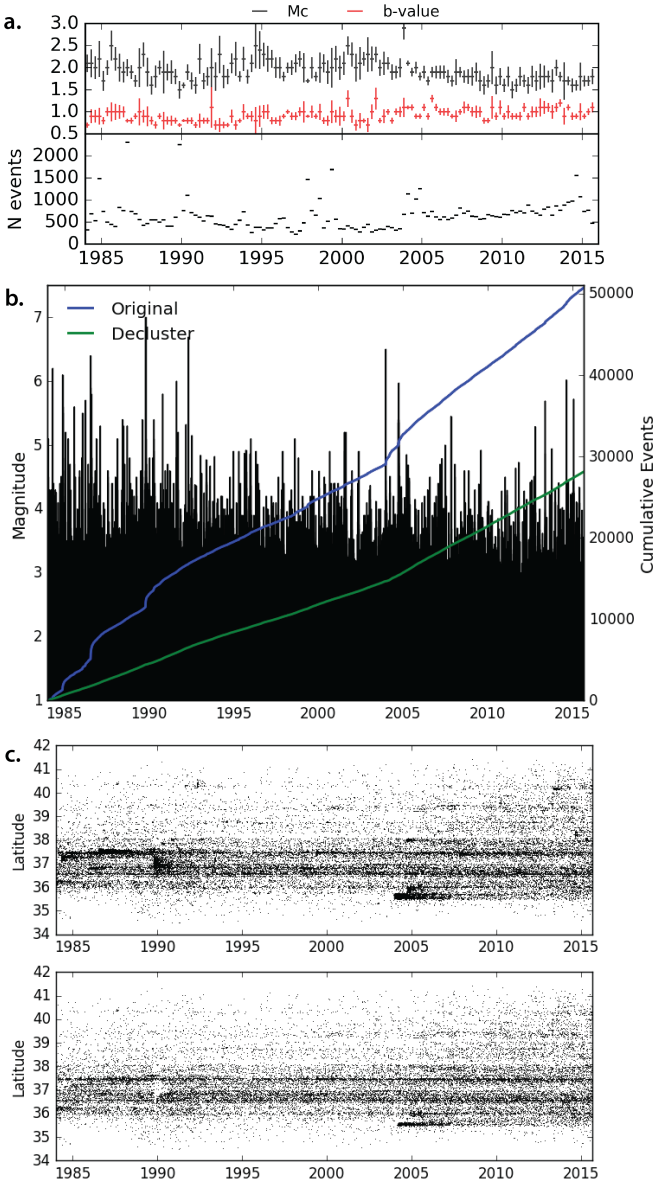

Figure 6.14: The M≥1.5 focal mechanism catalog between 1984-2015. (A) The magnitude of completeness through time with a 0.25 year time step. The results show a decreasing value as the monitoring network improves. (B) The magnitude shown in time with the cumulative number of events for the original and declustered catalog. The declustering shows an increasing rate at ∼2004 which is observed in the magnitude of completeness decreasing as more instrumentation is deployed and more small events are detected. (C) Time vs latitude shows the removal of clusters but also indicated more events post 2004.

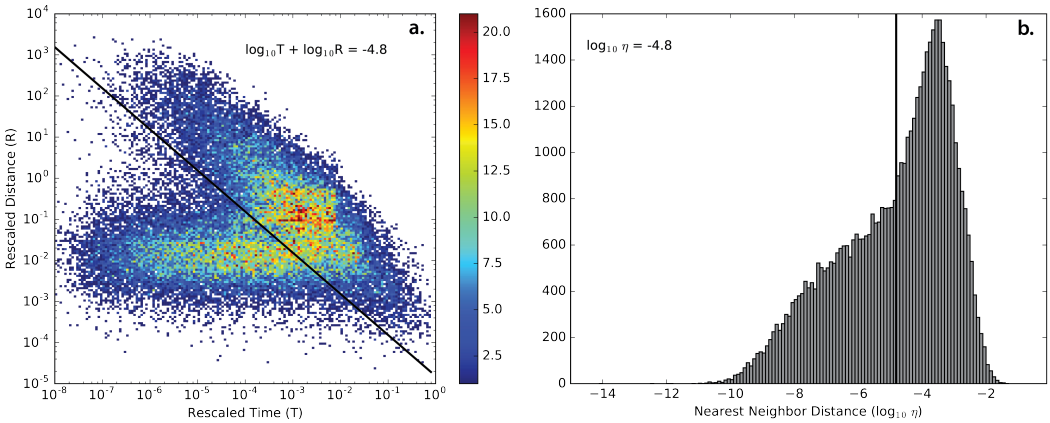

Figure 6.15: The Nearest Neighbor rescaled time and distance for the M≥1.5 events between 1984-2015. (A) The histogram of rescaled time and rescaled distance indicates a bimodal distribution that is separated along the black line for the declustering. The black line is where log_{10}(T) + log_{10}(R) = -4.8 and represents the maximum likelihood solution for the midpoint between the distributions. (B) The distribution of $log_{10}\eta$ with the maximum likelihood solution bimodal separation line shown at -4.8. In both figures the events to the right of the black line are considered independent events and retained for the analysis.

Where t_{ij} is the interevent time in years, r_{ij} is the distance between events in kilometer, q is a spatiotemporal scaling factor of 0.5 for this study, b is the b-value of 1.0 for this study, m is the event magnitude, and d_f is a distance scaling factor of 1.6 for this study following Zaliapin and Ben-Zion (2013). The nearest neighbor value represents the minimum scaled distance for each event. The method has the advantage of not being sensitive to the catalog magnitude of completeness when finding event pairs and allows the use of more low magnitude events in the catalog. The lower the nearest neighbor value the closer in space and time the daughter event is to a parent and is more likely a dependent event, i.e. an aftershock. The bimodal distribution is separated at log_{10}(T) + log_{10}(R) = -4.8 (Figure 6.15). Removing the clusters, i.e. events with η <-4.8 using the maximum likelihood estimate of splitting two distributions, retains 28,121 focal mechanisms.

6.4.2 Background Stress Orientation

Stress Inversion

The principal axis orientations of the background stress are estimated from the focal mechanism geometry using the damped inversion technique implemented with the SATSI software package (Hardebeck and Michael, 2006). The inversion is performed using a 10-km grid patch spacing, where the stress orientation reported is derived from the events in the volume under each patch. The focal mechanisms are evaluated following similar criteria to other focal mechanism inversion studies with the goal of retaining the highest quality data

set [e.g. (Hardebeck and Michael, 2006; Kilb and Hardebeck, 2006; Provost and Houston, 2001; Provost and Houston, 2003; Yang and Hauksson, 2013)]. The focal mechanism quality is evaluated and events are removed as follows: strike, dip, or rake angle error >35°, station distribution value <0.45, azimuthal gap > 150°, solution misfit >0.2. The remaining 5,618 focal mechanisms are assigned to the nearest grid patch location. For a grid patch to be used it must contain >30 events. In regions of sparse seismicity, if a grid patch contains fewer than the 30 events it is combined with nearest surrounding patches to obtain the 30 event cutoff. A location that still fails to reach 30 events is not included in the analysis. For locations with >30 events the 30 focal mechanisms are randomly selected from the population. When performing the inversion all grid patches contain 30 focal mechanisms. Performing the inversion multiple time with different sets of randomly selected focal planes does not substantially alter the stress inversion results. To determine the best model solution, the variance and misfit are evaluated for a suite of spatial damping parameters. A value of 1.6 is used for the study and little change is observed if the damping parameters 1.7 - 2.1 are used. The selection procedure is repeated using a minimum of 10 events per grid patch to test the sensitivity of the results when including regions with lower seismicity rates and increase the number of locations with a stress orientation. The stress inversion results are shown as the azimuth of maximum horizontal stress (SHmax) and the color is the A_ϕ value following (Simpson, 1997) to indicate the Andersonian faulting style based on the shape of the stress tensor (Figure 6.16). This assumes the plane of maximum shear stress, i.e. the slip direction, is within ∼30° of the largest principle stress orientation. The 95% confidence interval is estimated with 1000 bootstraps of the inversion (Figure 6.17). Overall the range of the confidence intervals are low with a median value of 10° (Figure 6.17).

Seasonal Background Stress Rotation

To test for a seasonal change in the background stress orientation during periods of seasonal loading we repeat the inversion with the data split into 6 month bins. The stress inversion gridding procedure is modified to include only grid patches with 20 events for both 6 month intervals. If a grid patch contains less than 20 for half the year it is not included. The time intervals are selected to estimate the wet and dry seasons to capture the hydrological loading cycle, which is the largest loading source for many faults (Figure 6.12). The background stress at each patch is determined by stacking all the focal mechanism from May - October and November - April. The procedure is repeated for the month intervals February - August and September to January to test the sensitivity of results. The inversion is calculated with the same spatial damping parameter of 1.6 and no temporal smoothing. The 95% percent confidence interval is calculated from 1000 bootstraps of each time interval. The results are quantified as the normalized tensor double dot product and the δA_ϕ values for the tensor obtained at each location for the different time of the year to assess the tensor orientations. The normalized tensor double dot product is a scalar between [-1,1], where 1 indicates that the summer and winter stress axes are perfectly aligned. The change in the A_ϕ value at a location indicates the change in shape with values that range from [-3,3], where 0

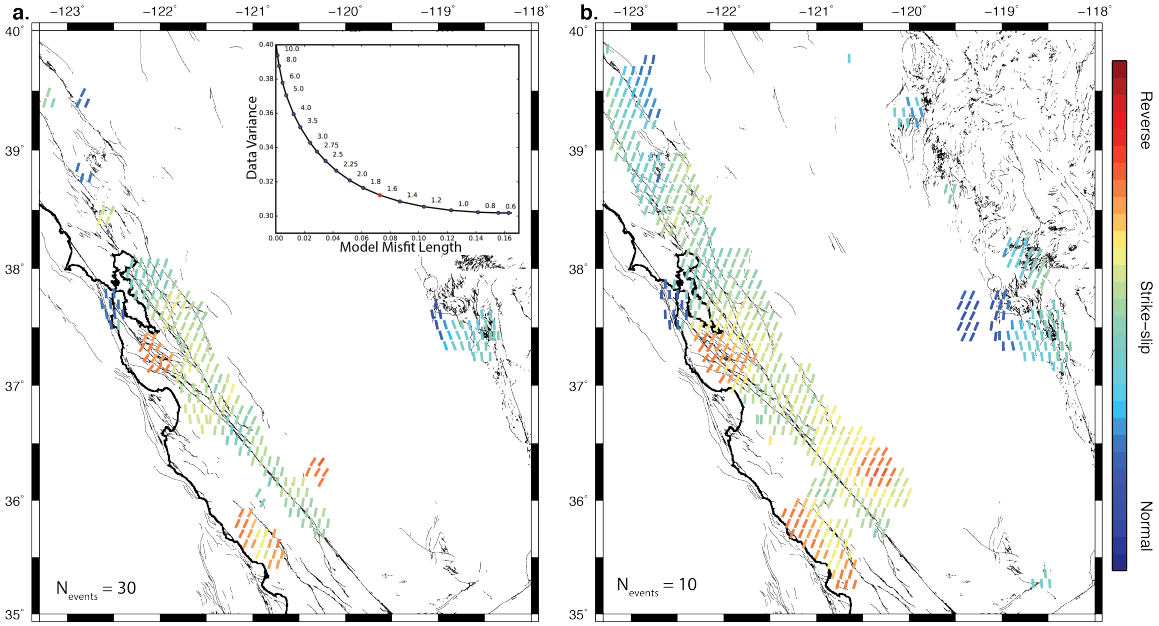

Figure 6.16: Background stress orientation from the focal mechanism inversion using a 10 km grid patch spacing. The results are shown for grid patches with minimum of 30 (a) and 10 (b) high-quality mechanisms. The orientation is the azimuth of SHmax and the color indicates the faulting style. The insert in the left panel shows the damping parameter tradeoff curve for the model misfit length vs the data variance. A damping value of 1.6 is used in this inversion and shown in red. The gray lines are the USGS mapped faults in the study area.

is no change. The results from both tests indicate very similar tensor orientations for the two seasonal intervals (Figure 6.18). The SHmax azimuth is shown with 95% confidence intervals and also indicates little difference between the seasons. The regions of the geothermal and volcanic activity do indicate the largest uncertainty in the stress orientation. We do not find a substantial rotation in background stress orientation from seasonal loading cycles.

6.4.3 Regional Seismicity Seasonal Response

The timing of seismic events is evaluated with respect to the seasonal stress perturbation in the direction of the principal stress orientation using the percentage of excess earthquakes that occur during a range of stressing intervals (Cochran et al., 2004; Johnson, Fu, et al., 2017). We utilize the background stress orientation derived from the focal mechanism inversion for the grid patches of 10 km x 10 km with N≥10 events (Figure 6.16b) and the declustered hypocentral catalog containing independent events with M≥1.7 from 2006 through 2014 (Figure 6.13). For each grid patch the principal stress directions are calculated and the seasonal loading monthly stress tensor time series is projected into the σ_1 and σ_3

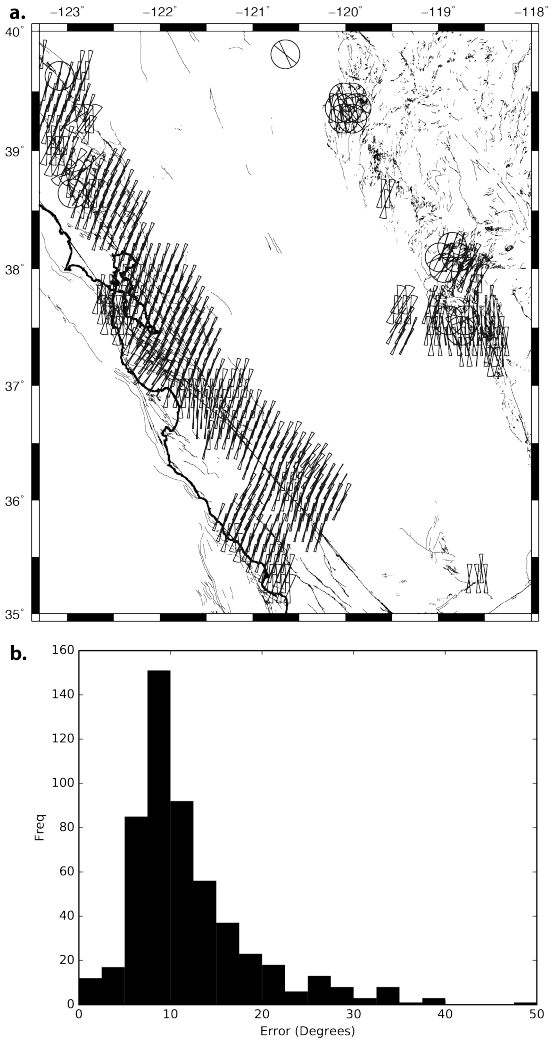

Figure 6.17: (a) Stress inversion confidence intervals shown at 95% for the SHmax stress orientation. (b) The distribution of error for the inversion results for the SHmax stress orientation.

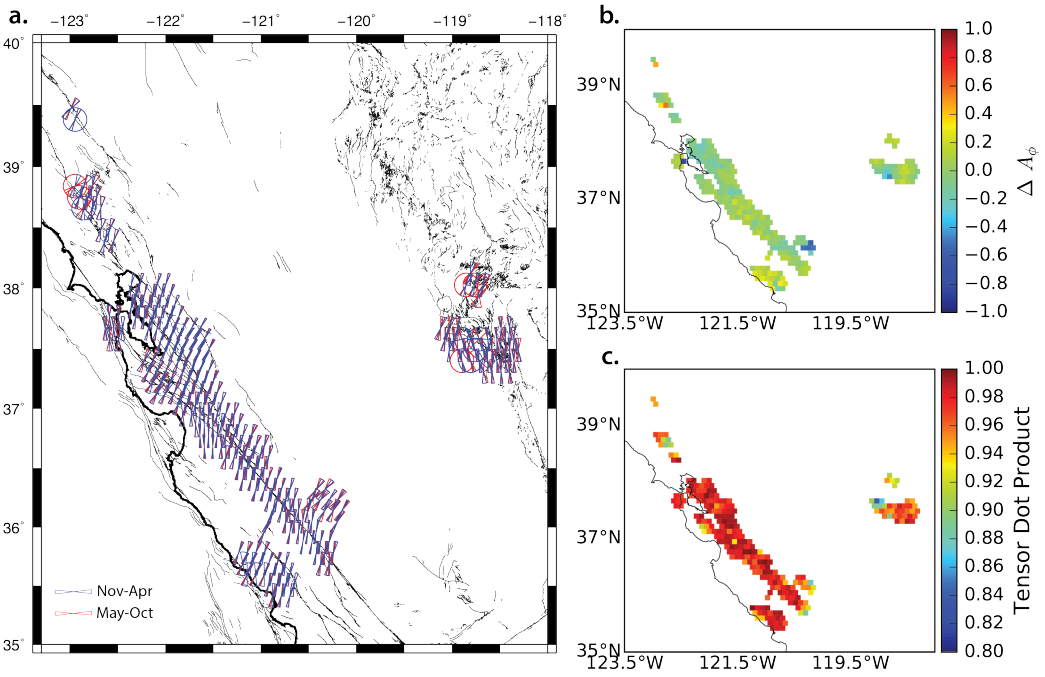

Figure 6.18: Seasonal stress tensor orientation comparison for the time intervals of May October and November April. (a) The azimuth of SHmax shown with 95% confidence intervals for winter (blue) and summer (red) months. (b) The change in the A_ϕ value is shown for each stress tensor location. A value of 0 suggests the orientation of the principle stress axis is the same for the two tensors. (c) The normalized tensor dot product is shown for each location where a value of 1.0 indicates the tensors are aligned.

orientations. In addition, we calculate time series for the differential stress (σ_1-σ_3), the mean normal stress (σ_1+σ_3)/2, and the square root of the second invariant of the deviatoric stress tensor, which represents the scalar magnitude of the shear stress, in order to test 5 different stress components with respect to the timing of each earthquake. The assumption is all the earthquakes located in the volume of each grid patch experience the stress perturbation calculated at the time of the event. The different stress components represent different stressing scenarios that promote failure on optimally oriented faults. Figure 6.19 schematically illustrates the increase in compression for σ_1, the decrease in compression for σ_3, and the change in differential stress, showing mechanically how these perturbations increase the chance of failure.

The percentage of excess earthquakes is calculated using equation 6.12, where N_{Ex} is the percentage of excess earthquakes per stress interval, N_{Act} is the actual number of events per stress interval, and N_{Exp} is the expected number of earthquakes assuming a uniform distribution of background events.

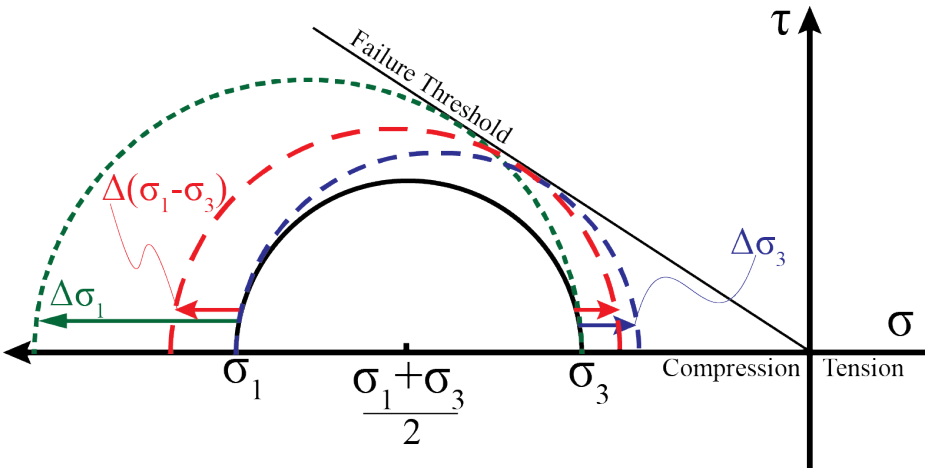

Figure 6.19: Mohr circle diagram schematically illustrating the change in stress for different principal components. The horizontal axis is the normal stress and the vertical axis is the shear stress. An earthquake is expected when the Mohr circle reaches the failure plane. In green shows an increase in compressional stress in the σ_1 orientation. In blue is the decrease in compression in the σ_3 orientation. In red is the differential stress changing the radius and shifting the circle.

$$N_{Ex} = \frac{N_{Act} - N_{Exp}}{N_{Exp}} 100\% \tag{6.12}$$

To obtain the distribution of the actual number (N_{Act}) of events, the stress perturbation at the time of each earthquake, in each grid patch (N=5,893) is evaluated for the 5 stressing time series of interest. The stresses are binned using a 1.0 kPa stress interval centered about zero. The stress interval is limited to the 99th percentile of the data range. All stresses beyond this range are binned in the outermost stress interval. The distribution of the expected number (N_{Exp}) of events is calculated by selecting 250 uniformly distributed times from each stressing time series for each earthquake. Following the same protocol the stresses are limited to the 99th percentile and the binned using a 1.0 kPa stress interval. The distribution is normalized by the total number of events time 250 to account for to oversampling of the time series. Following equation 6.12 the N_{Ex} value is calculated for each stress interval. A variance weighted regression line is fit to the N_{Ex} values and reported as the slope of the trend with a 2-sigma error estimate.

The seismicity results indicate that more earthquakes are occurring during the increased compression in the σ_1 orientation and the increased compression of the differential stress (σ_1-σ_3) (Figure 6.20). The reduction of compressive stress in the σ_3 orientation is expected to also correlate with increased seismicity (Figure 6.19), however, the percent excess seismicity is not showing any significant change in the stressing cycle. Similarly, the mean normal

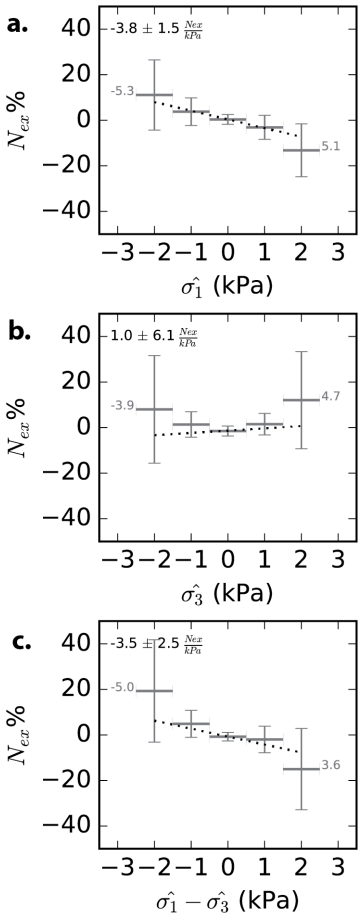

Figure 6.20: The percent excess seismicity for (a) the σ_1 orientation, (b) σ_3 orientation, (c) and the differential stress (σ_1-σ_3). The horizontal bar shows the stress interval, the vertical error bars represent the 95% confidence interval. The numeric values at the end member bins is the minimum and maximum range of the stresses. The trend of the best fit line is shown in the top left of each panel with the 2-sigma error.

stress and the square root of the second invariant and do not indicate a detectable change in earthquake occurrence (Figure 6.21). We repeat the analysis using a magnitude threshold of M$\geq$2.0, which reduces the number of earthquakes by half, and do not find a significant correlation for any stressing component above the confidence intervals due to the increased uncertainty when using a smaller population of events.

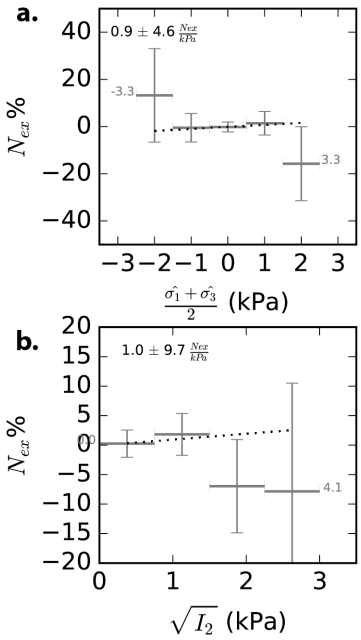

Figure 6.21: Percent excess seismicity for the (a) mean normal stress and (b) the square root of the second invariant of the stress tensor. The horizontal bar shows the stress interval, the vertical error bars represent the 95% confidence interval. The numeric values at the end member bins is the minimum and maximum range of the stresses. The trend of the best fit line is shown in the top left of each panel with the 2-sigma error.

6.5 Discussion

6.5.1 Seasonal Loads and Background Stress Perturbations

The integrated load time series in this analysis is constructed from multiple data sets to produce a comprehensive view of the stress changes during seasonal loading cycles. The deformation results indicate that the pole-tide, atmosphere, annual ocean tide, and the water loading are the largest sources of annual deformation for the earthquake faults investigated in central and northern California. When analyzing seasonal deformation these four largest loads should be considered collectively to more accurately describe the deformation. Seasonal stress changes have also been calculated for the Earth body tides, non-tidal-ocean loads, and changes in surface temperature, but their contribution to stress changes at seismogenic depths (8 km) is 1-2 orders of magnitude smaller. In many locations examined in this study the hydrospheric loads are the largest sources of transient deformation for the fault geometries in California (Figure 6.12), with the earth pole tides being the largest loading source for faults at greater distances from the Sierra Nevada as the hydrological loading diminishes (Johnson, Fu, et al., 2017). Depending on the geometry, some faults located near

the coast experience the largest stress change from the annual ocean tidal cycle, but the non-tidal ocean loading does not substantially contribute (Dill and Dobslaw, 2013). The annual earth body tides are the smallest amplitude load considered and are negligible when compared to other sources of deformation. However, if investigating short period loading cycles (Delorey, Elst, et al., 2017), the daily tidal cycles will contribute to the stress changes and should be included for a complete representation of the deformation as the semi-diurnal and diurnal constituents are 1-2 orders of magnitude larger than the annual tides.

The spatial heterogeneity of the regional fault geometry and the spatiotemporal heterogeneity in the loading cycles can together produce stressing conditions that may favor or suppress slip on a fault. We present 6 locations as examples along 2 transects extending inland from the coast for 300 km. The results highlight how the stresses from different loading sources can change on spatial scales of <75 km and is strongly dependent on the fault orientation and slip direction. At the Oceanic Fault Zone (Figure 6.5), the distance from the water loading source and the fault geometry produces small stress amplitudes for the fault normal stress component and is dominated by the ocean loading, however, the San Andreas fault (Figure 6.6), located 70 km to the east, experiences the largest stress change from the water loading. The strike of the San Andreas Fault is subparallel to the Sierra Nevada, where the largest snow and water accumulation occurs. This orientation produces a cycle of clamping in the winter and unclamping in the summer (Amos et al., 2014) that changes the normal stress on the fault. At Oceanic Fault Zone a large contribution to the normal stress modulation is the atmosphere loading, which accounts for half of the total load, with the majority from the ocean tides. Similarly, the source of the shear stresses at the two locations vary over these short distances. At the San Andreas Fault the largest shear stress is from the pole-tide, while the annual ocean loading producing the largest shear stress change at the Oceanic Fault Zone. Interestingly, despite this complex integration of seasonal loading cycles on adjacent faults, the peak stress change and the time of year when this occurs is very similar (Figure 6.11). However, this aggregate stressing scenario where all things average out is not a ubiquitous phenomenon when resolving seasonal stresses on faults throughout the plate boundary system. For example, when considering the Keough Hot Springs Fault along the same transect the Coulomb stress change is ∼4x less than the San Andreas and Oceanic Fault due to the fault geometry and slip direction. This implies that inclusion of all stressing sources and the best representation of the spatially varying fault geometry is needed to provide a robust estimate of seasonal stress changes.

Seasonal loading cycles are shown to induce small stress perturbations for known fault orientations and we pose the question if a regional change in the background stress field is resolvable throughout the annual cycle. A detectable change in the background stress field requires a stress perturbation greater than the ambient crustal stress to induce a change or rotation in the principal stress orientation (Hardebeck, 2010). Regional-scale studies characterizing the background tectonic stress field using focal mechanisms find a stress orientation that varies smoothly on length scales of 10 km (Hardebeck and Michael, 2006), with more localized stress heterogeneities observed across major faults (Provost and Houston, 2001; Provost and Houston, 2003; Yang and Hauksson, 2013). Large earthquakes can perturb the

stress field (Michael, 1987), but the orientation of aftershocks still tend to occur where the stress perturbation preferentially aligns with the background stress (Hardebeck, 2010; King et al., 1994; Stein, 1999). This suggests many faults in seismically active regions are optimally oriented with respect to the background stress field and possibly fail due to stress changes that are substantially less than the ambient stress in the crust. Careful examination using two comparison techniques of the seasonal loading stress tensors stacked over two 6-month periods do not indicate a change in the background stress field. A seasonal rotation is also not observed beyond the confidence intervals of the maximum horizontal stress orientation. The region north of The Geysers and south of Long Valley caldera do indicate larger uncertainties, but this can be attributed to a normal faulting environment where the horizontal stresses are less than the vertical stress, thereby introducing more variability when resolving the orientation of the maximum horizontal stress. Our results imply that the strength of the crust is greater than the seasonal loads and agrees with earthquake rupture studies that report similar results for coseismic stress changes of 10 kPa to 1 MPa (Hardebeck, 2010). Therefore, any observed change in seismicity would presumably be occurring due to a stress perturbation on the fault plane or in the principal stress orientation.

6.5.2 Earthquake response to stress perturbation

Earthquake triggering represents the occurrence of an earthquake due to a known transient stress and has implication for nucleation processes. Seasonal loads provide a natural experiment to quantify a cyclic loading stress perturbation and measure the seismic response. Periodic signals in the seismicity records have been observed in California along the San Andreas Fault in the central Coast Ranges and in the eastern Sierra Nevada, with the inference that seasonal forces or pore pressure changes are modulating seismicity (Christiansen et al., 2007; Dutilleul et al., 2015). Using the same hydrological loads in this study, Johnson, Fu, et al. (2017) found a 10% change in central and northern California seismicity from the background occurrence that correlates with the peak shear stresses when resolved in the focal plane orientations. The use of shear, normal, and Coulomb stresses to describe a transient load requires knowledge of the fault orientation to resolve the stress change. Alternatively, the principal stress orientations represent the preferred orientation of a failure plane within $\sim$30° of the principal stress direction. The results shown in Figure 6.20 indicate a change in the compressional stress of $\sim$5 kPa in the σ_1 orientation results in a $\pm$10% change in seismicity. This correlation is not observed for the 3 orientation alone, but is found for the differential stress (σ_1-σ_3) which indicates the σ_3 orientation could be involved in the modest change in earthquake occurrence.

Exploring the seasonal stresses that are projected into the principal stress orientation provides additional information about the response of the fault to a transient load. The increase in compressional stresses in the σ_1 orientation increases both shear and normal stress on a fault plane and the amplitude of the change is dependent on the incident of the stress orientation to the rupture plane. The reduction of compressional stresses in the σ_3 orientation reduces the normal stress while increasing the shear stress and we might expect

to find increased seismicity rates for this scenario. Our results do not show evidence for a resolvable increase in seismic activity for a changing stress in the σ_3 orientation, suggesting the faults are less sensitive to normal stress changes. This agrees with the Johnson, Fu, et al. (2017) results that seasonal earthquake modulation in California is controlled by changes in the shear stresses but they cannot say with confidence the unclamping effect of reduced normal stresses contributes the seasonal seismicity. Additionally, we do not find an increase in seismicity rates when examining the mean normal stress on the fault plane or the second invariant of the stress tensor (Figure 6.21). This suggests that other failure processes could be contributing to the variations in seismicity rates. One possibility is the mobilization of fluids in the crust (Christiansen et al., 2007). A plausible scenario is the increased compressive stress introduces a pressure gradient that reduces the pore pressure on the fault and decreases the slip potential on the fault plane and would require a time dependence for failure that is not explored in this study. The lack of correlation with the second invariant of the stress tensor suggests that knowing the fault geometry is important when resolving the shear stress changes on faults. If the direction of the shear stress change is not optimally oriented for slip, then an increase in seismicity rates would not be expected.

Seismicity changes that are invariant to the normal stresses suggests that faults are mechanically weak. For the San Andreas Fault system, Provost and Houston (2003) find the frictional strength most likely varies along strike, as indicated by the indecent angle of the maximum horizontal stress with respect to the fault plane, with strength increasing as distance along the fault increases to the north. In the northern section of the San Andreas Fault system the seismicity rates are much lower than the creeping section that is frictionally weak (Provost and Houston, 2001). Here the results are not examined by specific locations of seismic activity and instead are aggregated by the relative stress change with respect to the background stress orientation. One possibility is the results presented in Figure 6.20 are representative of the central San Andreas Fault system where the seismicity rates are higher, thereby suggesting a weaker fault system.

6.6 Conclusions

We investigate the role of 7 sources of seasonal loading to constrain the contribution of each on fault geometry in a seismically active region. The results indicate the water loading cycle and the pole-tides are the largest source of seasonal Coulomb stress changes. Our results find the loads investigated all contribute to the seasonal deformation and should be considered in studies of seasonal loading if the hydrological loading cycle is the same order of magnitude as the other loading cycle. The investigation of 6 different faults located along two transects quantifies the spatial variations in the stresses resolved for specific geometries of slip. The dominant loading source and stresses resolved can change on short spatial scales. The in-phase or out-of-phase cycles of the different loads is shown to produce constructive and destructive interference of the stressing time series and the seasonal stress estimates can alter if not all loading sources producing the same order of magnitude of stresses is not

considered.

The ambient background stress field is investigated for seasonal variations during the loading cycles and enhancement or suppression of seismicity. The results do not indicate a change in the orientation of the stress tensors or the maximum horizontal stress direction suggesting an observable change in seismicity is possibly from stress changes in the direction of the background stress. The timing of the seismicity is found to increase during periods of maximum compressive stress in the σ_1 orientation, but not when compressive stresses are reduced in the σ_3 orientation suggesting the increase in shear stress is a more resolvable signal and plausible failure mechanism than a reduction of normal stresses when examining the timing of seismicity. Our results support faults failing when stress perturbations are optimally oriented for slip with respect to the background stress orientations and population of faults exist in the crust that are near failure and rupture during a period of transient loading.

Chapter 7

Conclusions

"Does this research help in predicting the big one?" is a question I was recently asked in an interview following a publication in a scientific journal. The short answer is as a scientific community we cannot predict the time, location, and magnitude of an earthquake, but learning more and more about the processes involved with nucleation and faulting will advance the ability to reach the goal of improved hazard assessments and possibly more reliable forecasts of earthquakes. An earthquake is the release of accumulated strain in the lithosphere when the strength of the fault material is exceeded. To the general public an earthquake is the ground shaking that occurs during the passage of the seismic waves and has little to do with the how, where, or why. However, to scientists who study earth processes, the term earthquake describes the breaking of a fault interface at seismogenic depths for a section of a fault zone that releases strain accumulated over 10's - 1,000's of years of tectonic loading. The associated ground shaking is only one component in a complex process of energy released into the earth. As of now there are fundamental processes in crustal strength, dynamic friction, time varying strain accumulation, earthquake cycling, and the state of stress on a fault prior to rupture that require continued investigation in laboratory experiments, field observations, remote sensing observations, and more advanced models to fully describe the earthquake cycle and nucleation process. A reason to continue investigating earthquake triggering, beyond basic curiosity, is getting at the underlying question of why does an earthquake rupture a specific time, location, and magnitude.

The common thread for the collection of work presented in this dissertation is observations of a quantifiable stress perturbation and the resulting changes in seismicity, either immediately or after some delay time, i.e. earthquake triggering. The initial question posed in the introduction asks why faults respond to transient loading in the form of a triggered earthquake on a particular fault. The collection of evidence supporting earthquake triggering from different loading sources, e.g. impounding of reservoirs, subsurface fluid injection, earthquake interaction, extends decades into the refereed literature with many compelling observations to support the phenomenon as a nonrandom process. In this collection of research three different sources of transient forcing are investigated: (1) dynamic stressing from teleseismic surface waves produced by the greatest global earthquakes, (2) subsurface

fluid injection during enhanced power production, (3) and regional-scale cyclic loading from the coupling of atmosphere, hydrosphere, earths rotation, and the interaction of celestial bodies to lithospheric deformation. These loading sources all produce a similar amplitude stress change on a fault that is 3-4 orders of magnitude less than the ambient stress on the fault, and they occur on time scales from short periods on the order of 10's - 100's of seconds to long-periods that are on the order of a year ($\sim \pi * 10^7$ seconds) or longer. This suggests that earthquake nucleation is a combination of multiple processes in a complex feedback system where asperities on the fault fail and frictional surfaces weaken as stress is transferred through the fault zone. Fully unraveling the processes of earthquake nucleation will require additional multidisciplinary investigations that include seismological and geodetic observations with models that include dynamic failure and hydrological processes.

From a fault rupture perspective, a large earthquake is the same as a small earthquake, so why a magnitude dependence may exist for triggering a large event is still an open question. In Chapter 2 and 3 we examine global catalog records and local seismic networks to explore the delay time of large magnitude earthquake triggering following a known transient stress. Dynamic triggering from global seismic wave interaction is not found to systematically trigger large earthquakes during the passage of the surface waves. One possibility for the lack of a systematic triggering observation is the requirement that a population of faults exists that are critically stressed and experience this transient load to be able to observe a triggered event. If that is true and large magnitude events should be triggered as often as smaller events, then the methodology applied in Chapter 2 requires more and more time to pass to observe a statistically significant rate change in large event triggering. In the study only one large magnitude event in the 35 years of data analyzed provides evidence for delayed dynamic triggering of other large events at teleseismic distances over the course of many days. Is there a magnitude dependence to earthquake triggering or is the lack of observation a function of time of records? This question remains and additional seismic and non-seismic observations are needed to provide insight to the earthquake nucleation process.

One conundrum with large magnitude triggering is relating the transient loading to a large earthquake if there is a time delay. The delayed response in earthquake triggering suggests more than one process is occurring simultaneously to culminate into a large magnitude event. The detailed investigation of 3 delayed dynamically triggered M$\geq$6 earthquakes following the 2012 M8.6 Indian Ocean earthquake shows that smaller earthquakes were triggered during the surface wave passage but a delay time of 14 hours lapsed before the large mainshock. Interestingly, small event triggering was not observed in the subduction zone environment examined, but was resolvable in two different transtensional tectonic regions. This suggests the regional stress field is a factor in the ability of a fault zone as the compressional stresses in a subduction zone are expected to be greater than a transtensional region. If these smaller triggered events represent the initiation of a large triggered large earthquake then additional geodetic observations would prove most useful in constraining the aseismic processes prior to the rupture. A good test would be to set out to trigger a large earthquake in the field in a well instrumented environment. Efforts are in discussion within the community to perform such an experiment. A strong motivation for this is that waste water injection is providing more

and more evidence that events as large as M5 can occur with subtle changes in pore pressure. This suggests that these faults are critically stressed and supports crustal hydraulics as a viable mechanism to trigger an earthquake with a measureable stress change.

Pore fluid pressure changes can initiate slip on a fault. Chapter 4 details an investigation of seismicity at The Geysers geothermal field where high-volume waste water injection occurs for enhanced energy production. The injection of cold water into a 200° - 400° environment produces both poroelastic and thermoelastic stresses that fracture the surrounding rock. The thermoelastic mechanism is not the same failure process as the poroelastic effect. The thermoelastic stresses are produced by the expansion and contraction of the material. The evidence for both processes in this study is the immediate increase in seismicity and the depth dependent seismicity that occurs over the following months as pore pressure diffuses through the geothermal system. The change in pore pressure on a fault interface is enhancing seismicity and the results from our study show more of the M≥4 earthquakes occurring in the time delay period when fluid pressures changes would be expected to contribute more to the stress changes.

Dynamic triggering and fluid injection processes tell us about the stresses on the faults and the small stress changes that produce earthquakes. In Chapter 4 and 5 the question of a period dependence loading cycle is explored by examining seasonal cycles and the induced stresses. Seasonal loading cycles vary spatially and temporally throughout California and the hydrological cycle produces a 1-5 kPa stress change on faults in the region. We carefully explore 7 loading cycles and find the water loading and earth pole tides produce the greatest shear stress change on a fault. For M≥2 earthquakes we find a ∼10% change in seismicity through the annual loading cycle. The stresses are calculated for the fault orientation of each earthquake and suggest the orientation of the fault must be preferentially aligned with the stress perturbation to promote failure. This is further supported by more seismicity occurring when loading are aligned with the background stress orientation and increase the occurrence of earthquakes. The stress changes are the same order of magnitude as the stresses induced by the semidiurnal tidal cycle, which does not show clear evidence for earthquake triggering and suggests a period dependence to the triggering phenomenon. If the nucleation phase is longer than the semidiurnal cycle then we would not expect to see a correlation with the daily tides. By exploring the annual loading cycles we can say the nucleation of an earthquake occurs on the time scale of a year or less. The study is extended to earthquakes of M>5.5 and finds similar results, but with less confidence due to the uncertainty of the 230 years of earthquake records and the transient loads modeled to produce that result. In order to support the results that quantify the seasonal stress changes and the relationship to seismic activity the analysis should be repeated in a different tectonic environment with different amplitudes of the seasonal loads. Choosing a region with larger magnitude events occurring more often is ideal to test the sensitivity to trigger these events. The insight gained from this is verifying laboratory experiments and mechanical models that indicate the periodic loading cycle should reveal information about the earthquake nucleation time scale.

Earthquake triggering has developed over the course of ∼25 years to a mature research area with many question left to be answered. One powerful aspect of this topic of study is the

ability to use these observations to advance problems in earthquake physics. As presented in this dissertation and scores of articles published in the literature many different natural processes can produce stresses that trigger earthquake, but the underlying mechanism of why these events do get triggered still remains unanswered. To continue moving forward and further investigate triggered earthquakes advances must be made in incorporating geodetic observations of aseismic processes prior to moderate to larger earthquakes, improved detection techniques of small magnitude event that can highlight breaking asperities and fault geometry, and an overall better understanding of the hydraulic processes that exist in fault networks through drilling projects, models, and fluid injection.

Bibliography

Ader, Thomas J. and Jean-Philippe Avouac (2013). "Detecting periodicities and declustering in earthquake catalogs using the Schuster spectrum, application to Himalayan seismicity". In: *Earth and Planetary Science Letters* 377-378, pp. 97–105. DOI: 10.1016/j.epsl.2013.06.032.

Ader, Thomas J, Nadia Lapusta, et al. (2014). "Response of rate-and-state seismogenic faults to harmonic shear-stress perturbations". In: *Geophysical Journal International* 198.1, pp. 385–413. DOI: 10.1093/gji/ggu144.

Agnew, D. C. (1997). "NLOADF: A program for computing ocean-tide loading". In: *Journal of Geophysical Research* 102.B3, pp. 5109–5110. DOI: 10.1029/96jb03458.

— (2015). "3.06 - Earth Tides A2 - Schubert, Gerald". In: *Treatise on Geophysics (Second Edition)*. Oxford: Elsevier, pp. 151–178. ISBN: 978-0-444-53803-1. DOI: http://dx.doi.org/10.1016/B978-0-444-53802-4.00058-0. URL: http://www.sciencedirect.com/science/article/pii/B9780444538024000580.

Aiken, C., J. P. Zimmerman, et al. (2015). "Triggered Seismic Events along the Eastern Denali Fault in Northwest Canada Following the 2012 Mw 7.8 Haida Gwaii, 2013 Mw 7.5 Craig, and Two Mw>8.5 Teleseismic Earthquakes". In: *Bulletin of the Seismological Society of America* 105.2B, pp. 1165–1177. DOI: 10.1785/0120140156.

Aiken, Chastity and Zhigang Peng (2014). "Dynamic triggering of microearthquakes in three geothermal/volcanic regions of California". In: *Journal of Geophysical Research* 119, pp. 6992–7009. DOI: 10.1002/2014JB011218.

Aiken, Chastity, Zhigang Peng, and Kevin Chao (2013). "Tremors along the Queen Charlotte Margin triggered by large teleseismic earthquakes". In: *Geophysical Research Letters* 40.5, pp. 829–834. DOI: 10.1002/grl.50220.

Aki, K. (1965). "Maximum likelihood estimate of b in the formula log N = a-bM and its confidence limits". In: *Bulletin of Earthquake Research* 43, pp. 237–239.

Amos, C. B. et al. (2014). "Uplift and seismicity driven by groundwater depletion in central California". In: *Nature* 509.7501, pp. 483–6. DOI: 10.1038/nature13275.

Argus, Donald F., Yuning Fu, and Felix W. Landerer (2014). "Seasonal variation in total water storage in California inferred from GPS observations of vertical land motion". In: *Geophysical Research Letters* 41.6, pp. 1971–1980. DOI: 10.1002/2014gl059570.

Barton, Colleen A., Mark D. Zoback, and Daniel Moos (1995). "Fluid flow along potentially active faults in crystalline rock". In: *Geology* 23.8, pp. 683–686. DOI: 10.1130/0091-7613(1995)023$<$0683:ffapaf$>$2.3.co;2.

Beall, J.J. and M.C. Wright (2010). "Southern extent of The Geysers high temperature reservoir based on seismic and geochemical evidence". In: *Geothermal Resources Council Transactions* 34, pp. 1199–1202.

Beall, Joseph J., Melinda C. Wright, et al. (2010). "Effect of High Rate Injection on Seismicity in The Geysers". In: *Geothermal Resources Council Transactions* 34, pp. 1203–1208.

Beeler, N. M. and D. A. Lockner (2003). "Why earthquakes correlate weakly with the solid Earth tides: Effects of periodic stress on the rate and probability of earthquake occurrence". In: *Journal of Geophysical Research* 108.B8. DOI: 10.1029/2001jb001518.

Bender, B. (1983). "Maximum likelihood estimation of b values for magnitude grouped data". In: *Bulletin of the Seismological Society of America* 73, pp. 831–51.

Ben-Zion, Y and AA Allam (2013). "Seasonal thermoelastic strain and postseismic effects in Parkfield borehole dilatometers". In: *Earth and Planetary Science Letters* 379, pp. 120–126. DOI: 10.1016/j.epsl.2013.08.024.

Ben-Zion, Yehuda and Peter Leary (1986). "Thermoelastic strain in a half-space covered by unconsolidated material". In: *Bulletin of the Seismological Society of America* 76.5, pp. 1447–1460.

Berger, Jon (1975). "A note on thermoelastic strains and tilts". In: *Journal of Geophysical Research* 80.2, pp. 274–277. DOI: 10.1029/JB080i002p00274.

Bettinelli, Pierre et al. (2008). "Seasonal variations of seismicity and geodetic strain in the Himalaya induced by surface hydrology". In: *Earth and Planetary Science Letters* 266.3-4, pp. 332–344. DOI: 10.1016/j.epsl.2007.11.021.

Bevis, Michael et al. (2005). "Seasonal fluctuations in the mass of the Amazon River system and Earth's elastic response". In: *Geophysical Research Letters* 32.16. DOI: 10.1029/2005GL023491.

Bodin, P and J. Gomberg (1994). "Triggered seismicity and deformation between the Landers, California, and Little Skull Mountain, Nevada, earthquakes". In: *Bulletin of the Seismological Society of America* 84.3, pp. 835–843.

Boehm, Johannes, Birgit Werl, and Harald Schuh (2006). "Troposphere mapping functions for GPS and very long baseline interferometry from European Centre for Medium-Range Weather Forecasts operational analysis data". In: *Journal of Geophysical Research: Solid Earth* 111.B2. DOI: 10.1029/2005JB003629.

Bollinger, L. et al. (2007). "Seasonal modulation of seismicity in the Himalaya of Nepal". In: *Geophysical Research Letters* 34.8. DOI: 10.1029/2006GL029192.

Borsa, A. A., D. C. Agnew, and D. R. Cayan (2014). "Ongoing drought-induced uplift in the western United States". In: *Science* 345.6204, pp. 1587–1590. DOI: 10.1002/wrcr.20173.

Boyle, K. and M. Zoback (2014). "The Stress State of the Northwest Geysers, California Geothermal Field, and Implications for Fault-Controlled Fluid Flow". In: *Bulletin of the Seismological Society of America* 104.5, pp. 2303–2312. DOI: 10.1785/0120130284.

Brodsky, E. E. (2003). "A mechanism for sustained groundwater pressure changes induced by distant earthquakes". In: *Journal of Geophysical Research* 108.B8. DOI: 10.1029/2002jb002321.

Brodsky, E. E., V. Karakosta, and H Kanamori (2000). "A New Observation of Dynamically Triggered Regional Seismicity: Earthquakes in Greece Following the August, 1999 Izmit, Turkey Earthquake". In: *Geophysical Research Letters* 27.17, pp. 2741–2744.

Brodsky, E. E. and L. J. Lajoie (2013). "Anthropogenic seismicity rates and operational parameters at the Salton Sea Geothermal Field". In: *Science* 341.6145, pp. 543–6. DOI: 10.1126/science.1239213.

Brodsky, E. E. and S. G. Prejean (2005). "New constraints on mechanisms of remotely triggered seismicity at Long Valley Caldera". In: *Journal of Geophysical Research* 110.B4. DOI: 10.1029/2004jb003211.

Brodsky, E. E. and Nicholas J. van der Elst (2014). "The Uses of Dynamic Earthquake Triggering". In: *Annual Review of Earth and Planetary Sciences* 42.1, pp. 317–339. DOI: 10.1146/annurev-earth-060313-054648.

Carpenter, B. M., C. Marone, and D. M. Saffer (2011). "Weakness of the San Andreas Fault revealed by samples from the active fault zone". In: *Nature Geosci* 4.4, pp. 251–254. DOI: http://www.nature.com/ngeo/journal/v4/n4/abs/ngeo1089.html#supplementary-information.

CDEC (2014). *California Data Exchange Center. [Available at http://cdec.water.ca.gov.]*

Chanard, K. et al. (2014). "Modeling deformation induced by seasonal variations of continental water in the Himalaya region: Sensitivity to Earth elastic structure". In: *Journal of Geophysical Research: Solid Earth* 119.6, pp. 5097–5113. DOI: 10.1002/2013jb010451.

Chao, Kevin et al. (2013). "A global search for triggered tremor following the 2011 Mw 9.0 Tohoku earthquake". In: *Bulletin of the Seismological Society of America* 103.2B, pp. 1551–1571. DOI: 10.1785/0120120171.

Chen, Kate Huihusan, Roland Bürgmann, and Robert M. Nadeau (2013). "Do earthquakes talk to each other? Triggering and interaction of repeating sequences at Parkfield". In: *Journal of Geophysical Research: Solid Earth* 118.1, pp. 165–182. DOI: 10.1029/2012jb009486.

Christiansen, Lizet B., Shaul Hurwitz, and Steven E. Ingebritsen (2007). "Annual modulation of seismicity along the San Andreas Fault near Parkfield, CA". In: *Geophysical Research Letters* 34.4. DOI: 10.1029/2006gl028634.

Cochran, Elizabeth S, John E Vidale, and Sachiko Tanaka (2004). "Earth tides can trigger shallow thrust fault earthquakes". In: *Science* 306.5699, pp. 1164–1166. DOI: 10.1126/science.1103961.

Convertito, Vincenzo et al. (2012). "From Induced Seismicity to Direct Time-Dependent Seismic Hazard". In: *Bulletin of the Seismological Society of America* 102.6, pp. 2563–2573. DOI: 10.1785/0120120036.

Delorey, Andrew A., Kevin Chao, et al. (2015). "Cascading elastic perturbation in Japan due to the 2012 Mw 8.6 Indian Ocean earthquake". In: *Science Advances* 1:e1500468.

Delorey, Andrew A., Nicholas J. van der Elst, and Paul A. Johnson (2017). "Tidal triggering of earthquakes suggests poroelastic behavior on the San Andreas Fault". In: *Earth and Planetary Science Letters* 460, pp. 164–170. DOI: https://doi.org/10.1016/j.epsl.2016.12.014.

DeMets, Charles, Richard G. Gordon, and Donald F. Argus (2010). "Geologically current plate motions". In: *Geophysical Journal International* 181.1, pp. 1–80. DOI: 10.1111/j.1365-246X.2009.04491.x.

Dill, R. and H. Dobslaw (2013). "Numerical simulations of global-scale high-resolution hydrological crustal deformations". In: *Journal of Geophysical Research: Solid Earth* 118.9, pp. 5008–5017. DOI: 10.1002/jgrb.50353.

Dutilleul, Pierre et al. (2015). "Multifrequential periodogram analysis of earthquake occurrence: An alternative approach to the Schuster spectrum, with two examples in central California". In: *Journal of Geophysical Research: Solid Earth* 120.12, pp. 8494–8515. DOI: 10.1002/2015JB012467.

Dziak, Robert P. et al. (2000). "Recent tectonics of the Blanco Ridge, eastern blanco transform fault zone". In: *Marine Geophysical Researches* 21, pp. 423–450.

Dziewonski, A. M., T. A. Chou, and J. H. Woodhouse (1981). "Determination of earthquake source parameters from waveform data for studies of global and regional seismicity". In: *Journal of Geophysical Research* 86, pp. 2825–2582. DOI: 10.1029/JB086iB04p02825.

Dziewonski, Adam M. and Don L. Anderson (1981). "Preliminary reference Earth model". In: *Physics of the Earth and Planetary Interiors* 25.4, pp. 297–356. DOI: http://dx.doi.org/10.1016/0031-9201(81)90046-7.

Eberhart-Phillips, Donna and David H. Oppenheimer (1984). "Induced seismicity in The Geysers Geothermal Area, California". In: *Journal of Geophysical Research: Solid Earth* 89.B2, pp. 1191–1207. DOI: 10.1029/JB089iB02p01191.

Egbert, Gary D. and Svetlana Y. Erofeeva (2002). "Efficient Inverse Modeling of Barotropic Ocean Tides". In: *Journal of Atmospheric and Oceanic Technology* 19.2, pp. 183–204. DOI: doi:10.1175/1520-0426(2002)019<0183:EIMOBO>2.0.CO;2.

Ekstrom, G., M. Nettles, and A. M. Dziewonski (2012). "The global CMT project 2004-2010: Centroid-moment tensors for 13,017 earthquakes". In: *Physics of the Earth and Planetary Interiors* 200-201, pp. 1–9. DOI: 10.1016/j.pepi.2012.04.002.

Ellsworth, W. L. (2013). "Injection-induced earthquakes". In: *Science* 341.6142, p. 1225942. DOI: 10.1126/science.1225942.

Evans, D. M. (1966). "The Denver area earthquakes and The Rocky Mountain Arsenal disposal well". In: *The Mountain Geologist* 3.1, pp. 23–36.

Fan, Wenyuan and Peter M. Shearer (2016). "Local near instantaneously dynamically triggered aftershocks of large earthquakes". In: *Science* 353.6304, pp. 1133–1136. DOI: 10.1126/science.aag0013.

Farrell, W. E. (1972). "Deformation of the Earth by surface loads". In: *Reviews of Geophysics* 10.3, pp. 761–797. DOI: 10.1029/RG010i003p00761.

Felzer, Karen R., Rachel E. Abercrombie, and Goran Ekstrom (2004). "A Common Origin for Aftershocks, Foreshocks, and Multiplets". In: *Bulletin of the Seismological Society of America* 94.1, pp. 88–98. DOI: 10.1785/0120030069.

Felzer, Karen R. and E. E. Brodsky (2005). "Testing the stress shadow hypothesis". In: *Journal of Geophysical Research* 110.B5. DOI: 10.1029/2004jb003277.

Felzer, K.R. (2013). "The UCERF3 earthquake catalog, in Uniform California earthquake rupture forecast, version 3 (UCERF3)-The time-independent model, Appendix K". In: *U.S. Geological Survey Open-File Report 2013-1165*, pp. 1–5.

Field, E.H. et al. (2013). "Uniform California earthquake rupture forecast, version 3 (UCERF3) The time-independent model: U.S. Geological Survey Open-File Report 2013-1165". In: *California Geological Survey Special Report 228, and Southern California Earthquake Center Publication 1792*, 97p, http://pubs.usgs.gov/of/2013/1165/.

Freed, Andrew M. (2005). "Earthquake Triggering by Static, Dynamic, and Postseismic Stress Transfer". In: *Annual Review of Earth and Planetary Sciences* 33.1, pp. 335–367. DOI: 10.1146/annurev.earth.33.092203.122505.

Friederich, Wolfgang and Jorg Dalkolmo (1995). "Complete synthetic seismograms for a spherically symmetric earth by a numerical computation of the Green's function in the frequency domain". In: *Geophysical Journal International* 122, pp. 537–550.

Fu, Yuning, Donald F. Argus, and Felix W. Landerer (2015). "GPS as an independent measurement to estimate terrestrial water storage variations in Washington and Oregon". In: *Journal of Geophysical Research: Solid Earth* 120.1, pp. 552–566. DOI: 10.1002/2014JB011415.

Fu, Yuning, J. T. Freymueller, and T. van Dam (2012). "The effect of using inconsistent ocean tidal loading models on GPS coordinate solutions". In: *Journal of Geodesy* 86.6, pp. 409–421. DOI: 10.1007/s00190-011-0528-1.

Fu, Yuning and Jeffrey T. Freymueller (2012). "Seasonal and long-term vertical deformation in the Nepal Himalaya constrained by GPS and GRACE measurements". In: *Journal of Geophysical Research: Solid Earth* 117.B3. DOI: 10.1029/2011jb008925.

Fuchs, F., M. Lupi, and S. A. Miller (2014). "Remotely triggered nonvolcanic tremor in Sumbawa, Indonesia". In: *Geophysical Research Letters* 41.12, pp. 4185–4193. DOI: 10.1002/2014gl060312.

Gao, S.S. et al. (2000). "Annual modulation of triggered seismicity following the 1992 Landers earthquake in California". In: *Nature* 406, pp. 500–4.

Ghosh, Abhijit et al. (2009). "Complex nonvolcanic tremor near Parkfield, California, triggered by the great 2004 Sumatra earthquake". In: *Journal of Geophysical Research* 114. DOI: 10.1029/2008jb006062.

Gomberg, J. (2001). "The failure of earthquake failure models". In: *Journal of Geophysical Research* 106.B8, p. 16253. DOI: 10.1029/2000jb000003.

— (2013). "Permanently enhanced dynamic triggering probabilities as evidenced by two M≥7.5 earthquakes". In: *Geophysical Research Letters*. DOI: 10.1002/grl.50933.

Gomberg, J., N. M. Beeler, et al. (1998). "Earthquake triggering by transient and static deformations". In: *Journal of Geophysical Research* 103.B10, p. 24411. DOI: 10.1029/98jb01125.

Gomberg, J. and P Bodin (1994). "Triggering of the Ms = 5.4 Little Skull Mountain, Nevada, earthquake with dynamic strains". In: *Bulletin of the Seismological Society of America* 84.3, pp. 844–853.

Gomberg, J., P Bodin, et al. (2004). "Earthquake nucleation by transient deformations caused by the M=7.9 Denali, Alaska, earthquake". In: *Nature* 427.6975, pp. 621–24.

Gomberg, J. and Brian Sherrod (2014). "Crustal earthquake triggering by modern great earthquakes on subduction zone thrusts". In: *Journal of Geophysical Research: Solid Earth*, 2012JB009826. DOI: 10.1002/2012JB009826.

Gonzalez-Huizar, Hector and Aaron A. Velasco (2011). "Dynamic triggering: Stress modeling and a case study". In: *Journal of Geophysical Research* 116.B2. DOI: 10.1029/2009jb007000.

Gonzalez-Huizar, Hector, Aaron A. Velasco, et al. (2012). "Remote triggered seismicity caused by the 2011, M9.0 Tohoku-Oki, Japan earthquake". In: *Geophysical Research Letters* 39.10. DOI: 10.1029/2012gl051015.

Grapenthin, Ronni et al. (2006). "Icelandic rhythmics: Annual modulation of land elevation and plate spreading by snow load". In: *Geophysical Research Letters* 33.24. DOI: 10.1029/2006GL028081.

Gritto, Roland, Douglas Dreger, et al. (2014). "Towards the Understanding of Induced Seismicity in Enhanced Geothermal Systems". In: p. 210. DOI: 10.2172/1154937.

Gritto, Roland and Steve P. Jarpe (2014). "Temporal variations of Vp/Vs-ratio at The Geysers geothermal field, USA". In: *Geothermics* 52, pp. 112–119. DOI: http://dx.doi.org/10.1016/j.geothermics.2014.01.012.

Gutenberg, R and C. F. Richter (1944). "Frequency of earthquakes in California". In: *Bulletin of the Seismological Society of America* 34, pp. 631–644.

Hainzl, S., Y. Ben-Zion, et al. (2013). "Testing atmospheric and tidal earthquake triggering at Mt. Hochstaufen, Germany". In: *Journal of Geophysical Research: Solid Earth* 118.10, pp. 5442–5452. DOI: 10.1002/jgrb.50387.

Hainzl, Sebastian and Yosihiko Ogata (2005). "Detecting fluid signals in seismicity data through statistical earthquake modeling". In: *Journal of Geophysical Research* 110.B5. DOI: 10.1029/2004jb003247.

Han, Shin-Chan (2017). "Elastic deformation of the Australian continent induced by seasonal water cycles and the 2010fffdfffdfffd2011 La Nifffdfffda determined using GPS and GRACE". In: *Geophysical Research Letters* 44.6, pp. 2763–2772. DOI: 10.1002/2017GL072999.

Hardebeck, Jeanne L (2010). "Aftershocks are well aligned with the background stress field, contradicting the hypothesis of highly heterogeneous crustal stress". In: *Journal of Geophysical Research: Solid Earth* 115.B12. DOI: 10.1029/2010JB007586.

Hardebeck, Jeanne L. and Andrew J. Michael (2004). "Stress orientations at intermediate angles to the San Andreas Fault, California". In: *Journal of Geophysical Research: Solid Earth* 109.B11. DOI: 10.1029/2004JB003239.

— (2006). "Damped regional-scale stress inversions: Methodology and examples for southern California and the Coalinga aftershock sequence". In: *Journal of Geophysical Research* 111.B11. DOI: 10.1029/2005jb004144.

Harris, Ruth A. (1998). "Introduction to Special Section: Stress Triggers, Stress Shadows, and Implications for Seismic Hazard". In: *Journal of Geophysical Research: Solid Earth* 103.B10, pp. 24347–24358. DOI: 10.1029/98JB01576.

Harris, Ruth A. and R. J. Archuleta (1991). "Fault steps and the dynamic rupture process: 2-D numerical simulations of a spontaneously propagating shear fracture". In: *Geophysical Research Letters* 18.5, pp. 893–96.

Hartline, Craig S, Mark A Walters, and Melinda C Wright (2015). "Three-Dimensional Structural Model Building, Induced Seismicity Analysis, Drilling Analysis, and Reservoir Management at The Geysers Geothermal Field, Northern California". In: *Geothermal Resources Council Transactions* 39, pp. 603–614.

Healy, JH et al. (1968). "The denver earthquakes". In: *Science* 161.3848, pp. 1301–1310.

Heki, Kosuke (2003). "Snow load and seasonal variation of earthquake occurrence in Japan". In: *Earth and Planetary Science Letters* 207.1, pp. 159–164. DOI: 10.1016/S0012-821X(02)01148-2.

Helmstetter, A. (2005). "Importance of small earthquakes for stress transfers and earthquake triggering". In: *Journal of Geophysical Research* 110, B05S08. DOI: 10.1029/2004JB003286.

Hill, D. P. (2012). "Dynamic Stresses, Coulomb Failure, and Remote Triggering–Corrected". In: *Bulletin of the Seismological Society of America* 102.6, pp. 2313–2336. DOI: 10.1785/0120120085.

— (2015). "On the Sensitivity of Transtensional Versus Transpressional Tectonic Regimes to Remote Dynamic Triggering by Coulomb Failure". In: *Bulletin of the Seismological Society of America*. DOI: 10.1785/0120140292.

Hill, D. P. and S. G. Prejean (2007). "4.09 - Dynamic Triggering". In: *Treatise on Geophysics*. Ed. by Gerald Schubert. Amsterdam: Elsevier, pp. 257–291. ISBN: 978-0-444-52748-6. DOI: http://dx.doi.org/10.1016/B978-044452748-6.00070-5. URL: http://www.sciencedirect.com/science/article/pii/B9780444527486000705.

— (2015). "Dynamic Triggering". In: *Treatise on Geophysics (2nd Edition)*. Ed. by Gerald Schubert. Vol. 4. Oxford: Elsevier, pp. 273–304. DOI: 10.1016/b978-0-444-53802-4.00078-6.

Hill, D. P., P. A. Reasenberg, et al. (1993). "Seismicity Remotely Triggered by the Magnitude 7.3 Landers, California, Earthquake". In: *Science* 260.5114, pp. 1617–1623.

Husker, A. L. and E. E. Brodsky (2004). "Seismicity in Idaho and Montana Triggered by the Denali Fault Earthquake: A Window into the Geologic Context for Seismic Triggering". In: *Bulletin of Earthquake Research* 94.6B, S310–S316.

Hutchings, Lawrence et al. (2015). "Micro-earthquake Analysis for Reservoir Properties at the Prati-32 Injection Test, The Geysers, California". In: *Preceedings of the Fourtieth Workshop on Geothermal Reservoir Engineering, Stanford University, Stanford, California, January 26-28*.

Iwata, Takaki (2008). "Low detection capability of global earthquakes after the occurrence of large earthquakes: investigation of the Harvard CMT catalogue". In: *Geophysical Journal International* 174.3, pp. 849–856. DOI: 10.1111/j.1365-246X.2008.03864.x.

Jaeger, J.C., N.G.W. Cook, and R.W. Zimmerman (2007). *Fundamentals of rock mechanics*. 4th. Malden, MA: Blackwell Publishing. ISBN: 978-0632057597.

Jeanne, Pierre, Jonny Rutqvist, Craig Hartline, et al. (2014). "Reservoir structure and properties from geomechanical modeling and microseismicity analyses associated with an enhanced geothermal system at The Geysers, California". In: *Geothermics* 51, pp. 460–469. DOI: 10.1016/j.geothermics.2014.02.003.

Jeanne, Pierre, Jonny Rutqvist, Antonio Pio Rinaldi, et al. (2015). "Seismic and aseismic deformations and impact on reservoir permeability: The case of EGS stimulation at The Geysers, California, USA". In: *Journal of Geophysical Research: Solid Earth* 120.11, pp. 7863–7882. DOI: 10.1002/2015JB012142.

Johnson, C. W., R. Bürgmann, and F. F. Pollitz (2015). "Rare dynamic triggering of remote M≥5.5 earthquakes from global catalog analysis". In: *Journal of Geophysical Research: Solid Earth* 120. DOI: doi:10.1002/2014JB011788.

Johnson, C. W., Y. N. Fu, and R. Bürgmann (2017). "Seasonal water storage, stress modulation, and California seismicity". In: *Science*. DOI: 10.1126/science.aak9547.

Johnson, Christopher W., Eoghan J. Totten, and Roland Bürgmann (2016). "Depth migration of seasonally induced seismicity at The Geysers geothermal field". In: *Geophysical Research Letters*. DOI: 10.1002/2016GL069546.

Kane, Deborah L. et al. (2007). "Quantifying the remote triggering capabilities of large earthquakes using data from the ANZA Seismic Network catalog (southern California)". In: *Journal of Geophysical Research* 112.B11. DOI: 10.1029/2006jb004714.

Kato, Aitaro, Jun'ichi Fukuda, and Kazushige Obara (2013). "Response of seismicity to static and dynamic stress changes induced by the 2011M9.0 Tohoku-Oki earthquake". In: *Geophysical Research Letters* 40.14, pp. 3572–3578. DOI: 10.1002/grl.50699.

Kennett, B.L.N, E.R. Engdahl, and R. Buland (1995). "Constraints on seismic velocities in the Earth from traveltimes". In: *Geophysical Journal International* 122, pp. 108–124.

Ketner, Dane and John Power (2013). "Characterization of seismic events during the 2009 eruption of Redoubt Volcano, Alaska". In: *Journal of Volcanology and Geothermal Research* 259, pp. 45–62. DOI: 10.1016/j.jvolgeores.2012.10.007.

Kilb, D. and Jeanne L Hardebeck (2006). "Fault Parameter Constraints Using Relocated Earthquakes: A Validation of First-Motion Focal-Mechanism Data". In: *Bulletin of the Seismological Society of America* 96.3, pp. 1140–1158. DOI: 10.1785/0120040239.

Kilb, D., Z. Peng, et al. (2012). "Listen, Watch, Learn: SeisSound Video Products". In: *Seismological Research Letters* 83.2, pp. 281–286. DOI: 10.1785/gssrl.83.2.281.

King, Geoffrey C. P., Ross S. Stein, and Jian Lin (1994). "Static stress changes and the triggering of earthquakes". In: *Bulletin of the Seismological Society of America* 84.3, pp. 935–953.

Kwiatek, Grzegorz et al. (2015). "Effects of long-term fluid injection on induced seismicity parameters and maximum magnitude in northwestern part of The Geysers geothermal field". In: *Journal of Geophysical Research: Solid Earth* 120.10, pp. 7085–7101. DOI: 10.1002/2015JB012362.

Lay, T. and T. C. Wallace (1995). *Modern Global Seismology*. San Diego, CA: Academic Press.

Linville, L et al. (2014). "Exploring remote earthquake triggering potential across EarthScope's Transportable Array through frequency domain array visualization". In: *Journal of Geophysical Research: Solid Earth* 119, pp. 8950–8963. DOI: 10.1002/2014JB011529.

Lockner, D. A., R. Summers, et al. (1982). "Laboratory measurements of reservoir rock from the Geysers geothermal field, California". In: *International Journal of Rock Mechanics and Mining Sciences and Geomechanics Abstracts* 19.2, pp. 65–80. DOI: 10.1016/0148-9062(82)91632-1.

Lockner, David A. and Nick M. Beeler (1999). "Premonitory slip and tidal triggering of earthquakes". In: *Journal of Geophysical Research: Solid Earth* 104.B9, pp. 20133–20151. DOI: 10.1029/1999JB900205.

Lyard, Florent et al. (2006). "Modelling the global ocean tides: modern insights from FES2004". In: *Ocean Dynamics* 56.5, pp. 394–415. DOI: 10.1007/s10236-006-0086-x.

Majer, Ernest L. et al. (2007). "Induced seismicity associated with Enhanced Geothermal Systems". In: *Geothermics* 36.3, pp. 185–222. DOI: 10.1016/j.geothermics.2007.03.003.

Mallman, Ellen P. and Tom Parsons (2008). "A global search for stress shadows". In: *Journal of Geophysical Research* 113.B12. DOI: 10.1029/2007jb005336.

Marks, S. M. et al. (1978). "Seismic monitoring at The Geysers geothermal field, California". In: *U.S. Geol. Surv. Open File Rept* 78-798, pp. 1–26.

Marsan, D., E. Prono, and A. Helmstetter (2013). "Monitoring Aseismic Forcing in Fault Zones Using Earthquake Time Series". In: *Bulletin of the Seismological Society of America* 103.1, pp. 169–179. DOI: 10.1785/0120110304.

Martinez-Garzon, Patricia et al. (2014). "Spatiotemporal changes, faulting regimes, and source parameters of induced seismicity: A case study from The Geysers geothermal field". In: *Journal of Geophysical Research: Solid Earth* 119.11, pp. 8378–8396. DOI: 10.1002/2014JB011385.

Mathews, M. V. and P. A. Reasenberg (1988). "Statistical methods for investigating quiescence and other temporal seismicity patterns". In: *Pure Applied Geophysics* 126.2-4, pp. 357–372.

McGuire, J. J. and G. C. Beroza (2012). "A rogue earthquake off Sumatra". In: *Science* 336.6085, pp. 1118–9. DOI: 10.1126/science.1223983.

Meng, L., J. P. Ampuero, et al. (2012). "Earthquake in a maze: compressional rupture branching during the 2012 M(w) 8.6 Sumatra earthquake". In: *Science* 337.6095, pp. 724–6. DOI: 10.1126/science.1224030.

Meng, X. and Z. Peng (2014). "Seismicity rate changes in the Salton Sea Geothermal Field and the San Jacinto Fault Zone after the 2010 Mw 7.2 El Mayor-Cucapah earthquake". In: *Geophysical Journal International* 197.3, pp. 1750–1762. DOI: 10.1093/gji/ggu085.

Michael, Andrew Jay (1987). "Stress rotation during the Coalinga Aftershock Sequence". In: *Journal of Geophysical Research: Solid Earth* 92.B8, pp. 7963–7979. DOI: 10.1029/JB092iB08p07963.

Mitchell, Kenneth E. et al. (2004). "The multi-institution North American Land Data Assimilation System (NLDAS): Utilizing multiple GCIP products and partners in a continental distributed hydrological modeling system". In: *Journal of Geophysical Research: Atmospheres* 109.D7. DOI: 10.1029/2003JD003823.

Miyazawa (2012). "Detection of seismic events triggered by P-waves from the 2011 Tohoku-Oki earthquake". In: *Earth, Planets and Space* 64.12, pp. 1223–1229. DOI: 10.5047/eps.2012.07.003.

Ogata, Yosihiko (1992). "Detection of precursory relative quiescence before great earthquakes through a statistical model". In: *Journal of Geophysical Research* 97.B13, p. 19845. DOI: 10.1029/92jb00708.

— (1999). "Seismicity Analysis through Point-process Modeling: A Review". In: *Pure Applied Geophysics* 155, pp. 471–507.

Ogata, Yosihiko and Koichi Katsura (1993). "Analysis of temporal and spatial heterogeneity of magnitude frequency distribution inferred from earthquake catalogues". In: *Geophysical Journal International* 113.3, pp. 727–738.

Page, Benjamin M., Robert G. Coleman, and George A. Thompson (1998). "Late Cenozoic tectonics of the central and southern Coast Ranges of California". In: *Geological Society of America Bulletin* 110.7, pp. 846–876. DOI: 10.1130/0016-7606(1998)110<0846:olctot>2.3.co;2.

Pankow, Kris L. et al. (2004). "Triggered Seismicity in Utah from the 3 November 2002 Denali Fault Earthquake". In: *Bulletin of the Seismological Society of America* 94.6B, S332–S347.

Parsons, Tom (2002). "Global Omori law decay of triggered earthquakes: Large aftershocks outside the classical aftershock zone". In: *Journal of Geophysical Research* 107.B9. DOI: 10.1029/2001jb000646.

— (2005). "A hypothesis for delayed dynamic earthquake triggering". In: *Geophysical Research Letters* 32.4. DOI: 10.1029/2004gl021811.

— (2006). "Tectonic stressing in California modeled from GPS observations". In: *Journal of Geophysical Research: Solid Earth* 111.B3. DOI: 10.1029/2005JB003946.

Parsons, Tom and Eric L. Geist (2014). "The 2010-2014.3 global earthquake rate increase". In: *Geophysical Research Letters*. DOI: 10.1002/2014gl060513.

Parsons, Tom, J. Ole Kaven, et al. (2012). "Unraveling the apparent magnitude threshold of remote earthquake triggering using full wavefield surface wave simulation". In: *Geochemistry, Geophysics, Geosystems* 13.6. DOI: 10.1029/2012gc004164.

Parsons, Tom, Margaret Segou, and Warner Marzocchi (2014). "The global aftershock zone". In: *Tectonophysics* 618, pp. 1–34. DOI: 10.1016/j.tecto.2014.01.038.

Parsons, Tom and Aaron A. Velasco (2011). "Absence of remotely triggered large earthquakes beyond the mainshock region". In: *Nature Geoscience* 4.5, pp. 312–316. DOI: 10.1038/ngeo1110.

Peng, Zhigang, David P. Hill, et al. (2010). "Remotely triggered microearthquakes and tremor in central California following the 2010 Mw8.8 Chile earthquake". In: *Geophysical Research Letters* 37.24. DOI: 10.1029/2010gl045462.

Peng, Zhigang, L. T. Long, and P. Zhao (2011). "The relevance of high-frequency analysis artifacts to remote triggering". In: *Seismological Research Letters* 82.5, pp. 654–660. DOI: 10.1785/gssrl.82.5.654.

Peng, Zhigang, John E. Vidale, et al. (2009). "Remote triggering of tremor along the San Andreas Fault in central California". In: *Journal of Geophysical Research* 114. DOI: 10.1029/2008jb006049.

Peng, Zhigang, Chunquan Wu, and Chastity Aiken (2011). "Delayed triggering of microearthquakes by multiple surface waves circling the Earth". In: *Geophysical Research Letters* 38.4. DOI: 10.1029/2010gl046373.

Perez-Campos, Xyoli et al. (2008). "Horizontal subduction and truncation of the Cocos Plate beneath central Mexico". In: *Geophysical Research Letters* 35.18. DOI: 10.1029/2008gl035127.

Plattner, C. et al. (2007). "New constraints on relative motion between the Pacific Plate and Baja California microplate (Mexico) from GPS measurements". In: *Geophysical Journal International* 170.3, pp. 1373–1380. DOI: 10.1111/j.1365-246X.2007.03494.x.

Pollitz, F. F. (1996). "Coseismic deformation from earthquake faulting on a spherical earth". In: *Geophysical Journal International* 125, pp. 1–14.

Pollitz, F. F., R. Bürgmann, et al. (2014). "The profound reach of the 11 April 2012 M 8.6 Indian Ocean earthquake: Short-term global triggering followed by a longer-term global shadow". In: *Bulletin of the Seismological Society of America* 104.2, pp. 972–984. DOI: 10.1785/0120130078.

Pollitz, F. F. and Malcolm J. S. Johnston (2006). "Direct test of static stress versus dynamic stress triggering of aftershocks". In: *Geophysical Research Letters* 33.15. DOI: 10.1029/2006gl026764.

Pollitz, F. F., R. S. Stein, et al. (2012). "The 11 April 2012 east Indian Ocean earthquake triggered large aftershocks worldwide". In: *Nature* 490.7419, pp. 250–3. DOI: 10.1038/nature11504.

Pollitz, F. F., A. Wech, et al. (2013). "Annual modulation of non-volcanic tremor in northern Cascadia". In: *Journal of Geophysical Research: Solid Earth* 118.5, pp. 2445–2459. DOI: 10.1002/jgrb.50181.

Prejean, S. G. and D. P. Hill (2009). "Dynamic triggering of earthquakes". In: *Encyclopedia of Complexity and Systems Science*. Ed. by R. Meyer. Springer, New York, pp. 2600–2621.

Prejean, S. G., D. P. Hill, et al. (2004). "Remotely triggered seismicity on the United States west coast following the Mw 7.9 Denali Fault earthquake". In: *Bulletin of the Seismological Society of America* 94.6B, S348–S359.

Provost, Ann-Sophie and Heidi Houston (2001). "Orientation of the stress field surrounding the creeping section of the San Andreas Fault: Evidence for a narrow mechanically weak fault zone". In: *Journal of Geophysical Research: Solid Earth* 106.B6, pp. 11373–11386. DOI: 10.1029/2001JB900007.

— (2003). "Stress orientations in northern and central California: Evidence for the evolution of frictional strength along the San Andreas plate boundary system". In: *Journal of Geophysical Research: Solid Earth* 108.B3. DOI: 10.1029/2001JB001123.

Reasenberg, P. A. and David H. Oppenheimer (1985). "FPFIT, FPPLOT, and FPPAGE: FORTRAN computer programs for calculating and displaying earthquake fault-plane solutions". In: *U.S. Geol. Surv. Open File Rept*, pp. 85–739.

Reasenberg, P. A. and R. W. Simpson (1992). "Response of Regional Seismicity to the Static Stress Change Produced by the Loma Prieta Earthquake". In: *Science* 255.5052, pp. 1687–90.

Reasenberg, Paul (1985). "Second-order moment of central California seismicity, 1969-1982". In: *Journal of Geophysical Research* 90.B7, p. 5479. DOI: 10.1029/JB090iB07p05479.

Richards-Dinger, K., R. S. Stein, and S. Toda (2010). "Decay of aftershock density with distance does not indicate triggering by dynamic stress". In: *Nature* 467.7315, pp. 583–6. DOI: 10.1038/nature09402.

Robeson, Scott M (2015). "Revisiting the recent California drought as an extreme value". In: *Geophysical Research Letters* 42.16, pp. 6771–6779. DOI: 10.1002/2015GL064593.

Rubinstein, Justin L. et al. (2008). "Tidal Modulation of Nonvolcanic Tremor". In: *Science* 319.5860, pp. 186–189. DOI: 10.1126/science.1150558.

Rutqvist, Jonny et al. (2013). "The Northwest Geysers EGS Demonstration Project, California: Pre-stimulation Modeling and Interpretation of the Stimulation". In: *Mathematical Geosciences* 47.1, pp. 3–29. DOI: 10.1007/s11004-013-9493-y.

Rybicki, K., T. Kato, and K. Kasahara (1985). "Mechanical interaction between neighboring active faults - static and dynamic stress-field induced by faulting". In: *Bulletin of Earthquake Research Institute Toyko* 60, pp. 1–21.

Saar, Martin O. and Michael Manga (2003). "Seismicity induced by seasonal groundwater recharge at Mt. Hood, Oregon". In: *Earth and Planetary Science Letters* 214.3fffdfffdfffd4, pp. 605–618. DOI: http://dx.doi.org/10.1016/S0012-821X(03)00418-7.

Sammis, C.G., L. An, and I. Ershaghi (1992). "Determining the 3-D fracture structure in the Geysers geothermal reservoir". In: *Preceedings of the Seventeenth Workshop on Geothermal Reservoir Engineering, Stanford University, Stanford, California, January 29-31.*

Savage, Heather M. and Chris Marone (2007). "Effects of shear velocity oscillations on stick-slip behavior in laboratory experiments". In: *Journal of Geophysical Research: Solid Earth* 112.B2. DOI: 10.1029/2005JB004238.

Shearer, P. M. and P. B. Stark (2012). "Global risk of big earthquakes has not recently increased". In: *Proc Natl Acad Sci U S A* 109.3, pp. 717–21. DOI: 10.1073/pnas.1118525109.

Shelly, D. R., G. C. Beroza, and S. Ide (2007). "Non-volcanic tremor and low-frequency earthquake swarms". In: *Nature* 446.7133, pp. 305–7. DOI: 10.1038/nature05666.

Shelly, David R. and D. P. Hill (2011). "Migrating swarms of brittle-failure earthquakes in the lower crust beneath Mammoth Mountain, California". In: *Geophysical Research Letters* 38.20. DOI: 10.1029/2011GL049336.

Shelly, David R., Zhigang Peng, et al. (2011). "Triggered creep as a possible mechanism for delayed dynamic triggering of tremor and earthquakes". In: *Nature Geoscience* 4.6, pp. 384–388. DOI: 10.1038/ngeo1141.

Shen, Zheng-Kang et al. (2005). "Pole-Tide Modulation of Slow Slip Events at Circum-Pacific Subduction Zones". In: *Bulletin of the Seismological Society of America* 95.5, pp. 2009–2015. DOI: 10.1785/0120050020.

Shi, Yaolin and Bruce A. Bolt (1982). "The Standard Error of the Magnitude-Frequency b Value". In: *Bulletin of the Seismological Society of America* 72.5, pp. 1677–1687.

Simpson, Robert W. (1997). "Quantifying Anderson's fault types". In: *Journal of Geophysical Research: Solid Earth* 102.B8, pp. 17909–17919. DOI: 10.1029/97JB01274.

Stark, M. (2003). "Seismic Evidence for a Long-Lived Enhanced Geothermal System (EGS) in The Northern Geysers Reservoir". In: *Geothermal Resources Council Transactions* 27, pp. 727–731.

Stark, M. A. (1991). "Microearthquakes: a tool to track injected water in The Geysers reservoir". In: *Geothermal Resources Council Monograph on The Geyser Geothermal Field, Special Report* 17, pp. 111–117.

Stein, R. S. (1999). "The role of stress transfer in earthquake occurrence". In: *Nature* 402, pp. 604–609.

Swenson, Sean and John Wahr (2006). "Post-processing removal of correlated errors in GRACE data". In: *Geophysical Research Letters* 33.8, n/a–n/a. DOI: 10.1029/2005GL025285.

Taira, T. et al. (2009). "Remote triggering of fault-strength changes on the San Andreas fault at Parkfield". In: *Nature* 461.7264, pp. 636–9. DOI: 10.1038/nature08395.

Tape, Carl et al. (2013). "Earthquake nucleation and triggering on an optimally oriented fault". In: *Earth and Planetary Science Letters* 363, pp. 231–241. DOI: 10.1016/j.epsl.2012.11.060.

Thomas, A. M., R. M. Nadeau, and R. Bürgmann (2009). "Tremor-tide correlations and near-lithostatic pore pressure on the deep San Andreas fault". In: *Nature* 462.7276, pp. 1048–51. DOI: 10.1038/nature08654.

Thurber, C. H. (1983). "Earthquake Location and Three-Dimensional Crustal Structure in the Coyote Lake Area, Central California". In: *Journal of Geophysical Research* 88.B10, pp. 8226–8236.

Tibi, R., D.A. Wiens, and H. Inoue (2003). "Remote triggering of deep earthquakes in the 2002 Tonga sequences". In: *Nature* 424.6951, pp. 921–25. DOI: 10.1038/nature01917.

Titus, Sarah J et al. (2011). "Geologic versus geodetic deformation adjacent to the San Andreas fault, central California". In: *Geological Society of America Bulletin* 123.5-6, pp. 794–820.

Tolstoy, Maya et al. (2002). "Breathing of the seafloor: Tidal correlations of seismicity at Axial volcano". In: *Geology* 30.6, pp. 503–506. DOI: 10.1130/0091-7613(2002)030<0503:botstc>2.0.co;2.

Toomey, Douglas et al. (2014). "The Cascadia Initiative: A sea change in seismological studies of subduction zones". In: *Oceanography* 27.2, pp. 138–150. DOI: 10.5670/oceanog.2014.49.

Trugman, Daniel T. et al. (2016). "A comparison of long-term changes in seismicity at the Geysers, Salton Sea, and Coso geothermal fields". In: *Journal of Geophysical Research: Solid Earth*. DOI: 10.1002/2015JB012510.

Tsai, Victor C. (2011). "A model for seasonal changes in GPS positions and seismic wave speeds due to thermoelastic and hydrologic variations". In: *Journal of Geophysical Research: Solid Earth* 116.B4. DOI: 10.1029/2010JB008156.

van Dam, T. (2010). *NCEP Derived 6 hourly, global surface displacements at 2.5 x 2.5 degree spacing [Available at urlhttp://geophy.uni.lu/ncep-loading.html.]*

van Dam, T. M. and J. M. Wahr (1987). "Displacements of the Earth's surface due to atmospheric loading: Effects on gravity and baseline measurements". In: *Journal of Geophysical Research: Solid Earth* 92.B2, pp. 1281–1286. DOI: 10.1029/JB092iB02p01281.

van der Elst, N. J. and E. E. Brodsky (2010). "Connecting near-field and far-field earthquake triggering to dynamic strain". In: *Journal of Geophysical Research* 115.B7. DOI: 10.1029/2009jb006681.

van der Elst, N. J., H. M. Savage, et al. (2013). "Enhanced remote earthquake triggering at fluid-injection sites in the midwestern United States". In: *Science* 341.6142, pp. 164–7. DOI: 10.1126/science.1238948.

Velasco, Aaron A. et al. (2008). "Global ubiquity of dynamic earthquake triggering". In: *Nature Geoscience* 1.6, pp. 375–379. DOI: 10.1038/ngeo204.

Vidale, John E. et al. (1998). "Absence of earthquake correlation with Earth tides: An indication of high preseismic fault stress rate". In: *Journal of Geophysical Research* 103.B10, p. 24567. DOI: 10.1029/98jb00594.

Wahr, John M. (1985). "Deformation induced by polar motion". In: *Journal of Geophysical Research: Solid Earth* 90.B11, pp. 9363–9368. DOI: 10.1029/JB090iB11p09363.

Wahr, John et al. (2013). "The use of GPS horizontals for loading studies, with applications to northern California and southeast Greenland". In: *Journal of Geophysical Research: Solid Earth* 118.4, pp. 1795–1806. DOI: 10.1002/jgrb.50104.

Walters, Mark A and J Combs (1992). "Heat flow in The Geysers-Clear Lake geothermal area of northern California, USA". In: *Monograph on the Geysers Geothermal Field*, pp. 43–53.

Wells, D.L. and K.J. Coppersmith (1994). "New Empirical Relationships among Magnitude, Rupture Length, Rupture Width, Rupture Area, and Surface Displacement". In: *Bulletin of the Seismological Society of America* 84.4, pp. 974–1002.

West, Michael, John J. Sanchez, and Stephen R. McNutt (2005). "Periodically triggered seismicity at Mount Wrangell, Alaska, after the Sumatra earthquake". In: *Science* 308, pp. 1144–1146.

Wiemer, S. and M Wyss (2000). "Minimum Magnitude of Completeness in Earthquake Catalogs: Examples from Alaska, the Western United States, and Japan". In: *Bulletin of the Seismological Society of America* 90.4, pp. 859–869. DOI: 10.1785/0119990114.

Wilson, Douglas S. (1993). "Confidence intervals for motion and deformation of the Juan de Fuca Plate". In: *Journal of Geophysical Research* 98.B9, p. 16053. DOI: 10.1029/93jb01227.

Withers, M. et al. (1998). "A comparisoin of select trigger algorithms for automated global seismic phase and event detection". In: *Bulletin of the Seismological Society of America* 88.1, pp. 95–106.

Woessner, J. and S. Wiemer (2005). "Assessing the Quality of Earthquake Catalogues: Estimating the Magnitude of Completeness and Its Uncertainty". In: *Bulletin of the Seismological Society of America* 95.2, pp. 684–698. DOI: 10.1785/0120040007.

Wurman, Gilead, Richard M. Allen, and Peter Lombard (2007). "Toward earthquake early warning in northern California". In: *Journal of Geophysical Research* 112.B8. DOI: 10.1029/2006jb004830.

Yang, Wenzheng and Egill Hauksson (2013). "The tectonic crustal stress field and style of faulting along the Pacific North America Plate boundary in Southern California". In: *Geophysical Journal International* 194.1, pp. 100–117. DOI: 10.1093/gji/ggt113.

Zaliapin, Ilya and Yehuda Ben-Zion (2013). "Earthquake clusters in southern California I: Identification and stability". In: *Journal of Geophysical Research: Solid Earth* 118.6, pp. 2847–2864. DOI: 10.1002/jgrb.50179.

Zhuang, Jiancang, David Harte, et al. (2012). "Basic models of seismicity: temporal models". In: *Community Online Resource for Statistical Seismicity Analysis*. DOI: 10.5078/corssa-79905851.

Zhuang, Jiancang, Yosihiko Ogata, and David Vere-Jones (2002). "Stochastic Declustering of Space-Time Earthquake Occurrences". In: *Journal of the American Statistical Association* 97.458, pp. 369–380. DOI: 10.1198/016214502760046925.

Zigone, Dimitri et al. (2012). "Triggering of tremors and slow slip event in Guerrero, Mexico, by the 2010 Mw 8.8 Maule, Chile, earthquake". In: *Journal of Geophysical Research* 117.B9. DOI: 10.1029/2012jb009160.

Zoback, Mary Lou (1992). "First-and second-order patterns of stress in the lithosphere: The World Stress Map Project". In: *Journal of Geophysical Research: Solid Earth* 97.B8, pp. 11703–11728.

Zumberge, J. F. et al. (1997). "Precise point positioning for the efficient and robust analysis of GPS data from large networks". In: *Journal of Geophysical Research: Solid Earth* 102.B3, pp. 5005–5017. DOI: 10.1029/96JB03860.